



<http://researchspace.auckland.ac.nz>

ResearchSpace@Auckland

Copyright Statement

The digital copy of this thesis is protected by the Copyright Act 1994 (New Zealand).

This thesis may be consulted by you, provided you comply with the provisions of the Act and the following conditions of use:

- Any use you make of these documents or images must be for research or private study purposes only, and you may not make them available to any other person.
- Authors control the copyright of their thesis. You will recognise the author's right to be identified as the author of this thesis, and due acknowledgement will be made to the author where appropriate.
- You will obtain the author's permission before publishing any material from their thesis.

To request permissions please use the Feedback form on our webpage.

<http://researchspace.auckland.ac.nz/feedback>

General copyright and disclaimer

In addition to the above conditions, authors give their consent for the digital copy of their work to be used subject to the conditions specified on the [Library Thesis Consent Form](#) and [Deposit Licence](#).

Anatomically-Based, Subject-Specific Modelling of Lower Limb Motion During Gait

by **Katja Oberhofer**

Supervised by Dr Iain A Anderson, A/Prof Susan Stott and
Dr Kumar Mithraratne

A thesis submitted in partial fulfilment of the requirements for the
degree of Doctor of Philosophy at the University of Auckland.

Auckland Bioengineering Institute
The University of Auckland
New Zealand

October 2009

Abstract

Musculoskeletal models provide insights into muscle structures, and allow for investigations of muscle function during walking based on data from gait analysis. The function of muscles during walking is of special interest in a clinical context if musculoskeletal impairments result in pathological gait. Skeletal muscles in clinical gait analysis have commonly been modelled as series of straight-line segments with no consideration for their 3D architecture. However, experimental and computational results suggest that muscle function is predetermined by anatomical features such as cross-sectional areas and fibre lengths. The validity of straight-line models in gait analysis has been disputed, especially for muscles with complex geometries and broad areas of attachment. The present PhD study has built on a combined effort between the Auckland Bioengineering Institute and the Department of Surgery, University of Auckland, for introducing anatomically-based, subject-specific modelling techniques into clinical gait analysis. In particular, the potential use of anatomically-based models in research related to Cerebral Palsy (CP) was explored. Theoretical background knowledge needed to be acquired in three areas in order to reach this goal: (i) anatomically-based, subject-specific modelling, (ii) clinical gait analysis and (iii) finite deformation of soft-tissue muscle models. The outcome of the present work has demonstrated that muscle volumes and muscle lengths in the lower limbs of children with CP are significantly altered compared to typically developing children, that the Host Mesh Fitting technique provides a valid and efficient method for deriving muscle soft-tissue deformations based on kinematic data from gait analysis, that the calculation of muscle-tendon lengths during walking is significantly affected by errors from optical motion capture and that interactive, web-based visualisation of musculoskeletal models could become a beneficial resource in the teaching of gait. At this stage, the application of anatomically-based, subject-specific models to clinical gait analysis is still considered visionary, requiring an interdisciplinary research effort for further advancing modelling and measurement techniques. Despite remaining challenges, the present work has highlighted the potential of anatomically-based, subject-specific modelling for assisting in the assessment and management of children with CP, and is considered the first step towards the next generation of musculoskeletal models in gait research.

Acknowledgements

Half way through my studies, a senior researcher said to me: “You need to be stubborn to finish a PhD”. It was certainly not only stubbornness that helped me through the present work but also the personal support and encouragement from my supervisors, work colleagues, family and friends; and the financial support from various funding organisations.

This thesis was made possible through the generous funding from the New Zealand Foundation for Research, Science and Technology, and the financial support from the University of Auckland through the Doctoral Fees Bursary. Additional support for travel expanses was provided by the Research Office of the University of Auckland via the Graduate Research Fund and by Education New Zealand via the Postgraduate Study Abroad Awards.

My deepest gratitude goes to my supervisors Dr Iain A Anderson, A/Prof Susan Stott and Dr Kumar Mithraratne for their genuine interest in musculoskeletal modelling, their trust in my abilities and their individual contributions. Dr Iain Anderson has often surprised me with new ideas, which have taught me to think outside the box and search for solid reasons for my endeavours. A/Prof Susan Stott has provided tremendous input as an orthopaedic surgeon, and her expertise in conducting clinical research has been invaluable for my studies. Dr Kumar Mithraratne has been an exceptional teacher and colleague, and I am deeply grateful for the many hours he spent explaining me the theoretical details.

Many of the presented ideas and results originated from invaluable discussions with fellow workers and friends. In particular, I owe much thanks to A/Prof Richard Baker and his team at the Hugh William Gait Laboratory, Murdoch Children’s Research Institute, Australia, who provided me unique insight into clinical gait analysis during a one-month visit. I am further grateful for the fantastic working atmosphere at the Auckland Bioengineering Institute, which has provided the basis for the outcome of this work. Further thanks goes to Dr Anna Mackey, physiotherapist at the Wilson Centre, Auckland, for her invaluable assistance in conducting research on children with CP; and to Dr Suzie Mudge for being an amazing friend and stimulating discussion partner.

Additional thanks goes to Megan Moreau and Dr Sharon Walt at the Tamaki Gait Laboratory, University of Auckland, for their help with the acquisition of kinematic data; Sandra Winsor and Anna-Maria Lydon at the Centre for Advanced MRI, University of Auckland, for their expertise and time in obtaining magnetic resonance images of the lower limbs; Robert Valkenburg at Industrial Research Limited, Auckland, for spontaneously agreeing in doing a surface scan of my lower limbs; and last but not least, all the children and their parents who agreed in participating in my studies, and hence, substantially contributed to this work.

New Zealand could not have been further way from my parents, sister and friends. However, it is the incredible support and unconditional love from my family that has allowed me to pursue the current life. My gratitude towards my family and my appreciation for the amazing upbringing in the Swiss Alps has constantly grown since leaving the secure shelter a few years ago. I have had enough time to build a new little home in New Zealand, though, my heart will always beat for the other side of the planet.

Recently, another wise person said to me: “You need to be patient to catch the big waves.” If I had to dedicate this work to anything, it would need to be the sea. My deep passion for windsurfing brought me to New Zealand, and my mental and physical escapes into the surf have kept me moving forward. At this stage, I am patiently looking forward to the bigger waves to come, both in my personal and my professional life.

Contents

List of Figures	i
List of Tables	iii
Glossary of Symbols	v
Glossary of Acronyms	vii
1 Introduction	1
1.1 Motivation	1
1.2 Aim	3
1.3 Thesis Overview	4
1.4 Thesis Contributions	5
2 Literature Review	7
2.1 Clinical Gait Analysis	7
2.2 Anatomically-Based, Subject-Specific Modelling	9
2.3 Cerebral Palsy	13
3 Theoretical Background	17
3.1 Development of Anatomically-Based Models	17
3.1.1 Magnetic Resonance Imaging (MRI)	17
3.1.2 Data Digitisation	19
3.1.3 Finite Element Representation of the Geometry	20
3.1.4 Fitting Techniques	24
3.1.5 Summary	28
3.2 Derivation of Segmental and Joint Kinematics	31
3.2.1 Optical Motion Capture System	31
3.2.2 Spatial and Material Coordinate Systems	33
3.2.3 Segmental Kinematics	39
3.2.4 Joint Kinematics	40
3.2.5 Error Sources and Optimisation Algorithms	44
3.2.6 Summary	45
3.3 Finite Deformation of Anatomically-Based Models	47
3.3.1 Inverse Kinematics	47
3.3.2 Geometric-Based Deformation Techniques	48

CONTENTS

3.3.3	Mechanics-Based Deformation Techniques	52
3.3.4	Volume Conservation and Collision Detection	56
3.3.5	Summary	59
4	Study I: Muscle Volumes and Lengths in Children with CP	61
4.1	Introduction	61
4.1.1	Aim	62
4.2	Subjects and Method	63
4.2.1	Subjects	63
4.2.2	Data Acquisition	63
4.2.3	Data Processing	65
4.2.4	Data Analysis	67
4.3	Results	69
4.3.1	Regression Analysis	69
4.3.2	Muscle Volumes and Muscle Lengths	71
4.4	Discussion	71
5	Study II: Prediction of Muscle Deformation During Gait	75
5.1	Introduction	75
5.1.1	Aim	76
5.2	Subjects and Methods	77
5.2.1	The Lower Limb Model	77
5.2.2	Kinematic Data	78
5.2.3	Modelling Soft-Tissue Muscle Deformation	80
5.2.4	Validation	83
5.3	Results	85
5.3.1	Walking Simulation	85
5.3.2	Validation	85
5.4	Discussion	88
6	Study III: Accuracy in Modelled Muscle-Tendon Lengths	91
6.1	Introduction	91
6.1.1	Aim	92
6.2	Subjects and Methods	93
6.2.1	Reference Kinematic Data	93
6.2.2	Musculoskeletal Model	93
6.2.3	Soft Tissue Artifacts	94
6.2.4	Error Propagation Analysis	95

6.3	Results	98
6.4	Discussion	101
7	Study IV: Visualisation of Muscle Activation During Gait	103
7.1	Introduction	103
7.1.1	Aim	104
7.2	Method	105
7.2.1	Musculoskeletal Model	105
7.2.2	Graphical User Interface	105
7.2.3	Functionalities	107
7.2.4	Validation	109
7.3	Results	109
7.4	Discussion	111
8	Conclusion	115
8.1	Summary	115
8.2	Impact	116
8.3	Limitations	118
8.4	Outlook	120
A	Ethical Approval Letter	123
B	Updating Nodal Derivatives	127
C	Singular Value Decomposition	129
D	Lower Limb Mesh Parameters	131
E	Questionnaire GUI	133
F	Supplementary Movies	135
	References	137

List of Figures

2.1	Series-of-line-segments simplification	10
2.2	Collection of anatomically-based models	14
2.3	Neuromusculoskeletal pathology in cerebral palsy	16
3.1	MRI data acquisition	19
3.2	Data digitisation	21
3.3	Face Fitting	25
3.4	Host Mesh Fitting	28
3.5	Flowchart fitting techniques	30
3.6	Vicon MX motion analysis system	32
3.7	Marker sets	34
3.8	Anatomical coordinate systems	38
3.9	Segmental kinematics	41
3.10	Euler/Cardan angles	43
3.11	Joint coordinate system	44
3.12	Inverse kinematics	48
3.13	Muscle soft-tissue deformation based on inverse kinematics	51
3.14	Host Mesh Fitting of several muscles	58
4.1	MRI slice of shank and thigh in children	66
4.2	Lower limb models of children	68
4.3	Results of linear regression analysis	70
4.4	Results in normalised muscle volumes and lengths	72
5.1	Refitting of glutei in standing position	78
5.2	Lower limb model in neutral position	79
5.3	Flowchart of gait simulation	81
5.4	Control points and skin-based host mesh	82
5.5	Positions in MRI during validation trial	84
5.6	Gait simulation including host mesh	85
5.7	Gait simulation from anterior, lateral and posterior	86
5.8	Validation results A	87
5.9	Validation results B	87
6.1	Musculoskeletal model for the error analysis	94
6.2	Flowchart error analysis	96

LIST OF FIGURES

6.3	Reference data error analysis	99
6.4	Resulting errors in muscle-tendon lengths	100
7.1	Muscle activation during gait	106
7.2	GUI functionalities	110
7.3	GUI screenshots	112
A.1	Ethical approval letter page 1a	123
A.2	Ethical approval letter page 1b	124
A.3	Ethical approval letter page 2a	124
A.4	Ethical approval letter page 2b	125
F.1	StaticChildrenModel.wmv	135
F.2	StaticLowerLimbs.wmv	135
F.3	GaitHost.wmv	136
F.4	Gait.wmv	136
F.5	GaitPelvis.wmv	136
F.6	GaitMuscleActivation.wmv	136

List of Tables

3.1	Anatomical landmarks	37
3.2	Mooney-Rivlin constants for muscle tissue	55
3.3	Deformation techniques for FE models	58
4.1	Characteristics control subjects	64
4.2	Characteristics CP subjects	64
4.3	Segmental lengths and joint angles during MRI	65
4.4	Results normalised muscle volumes and muscle lengths	71
5.1	Validation results	88
6.1	Resulting errors in knee joint angles	98
6.2	Resulting errors in muscle-tendon lengths	99
7.1	Muscle activation patterns during gait	108
D.1	Lower limb bone mesh parameters	131
D.2	Lower limb muscle mesh parameters	132
E.1	GUI questionnaire general layout	133
E.2	GUI questionnaire content information	133
E.3	GUI questionnaire pedagogical usability	134

List of Symbols

\mathbf{u}_i	Spatial position of node i
Φ_1, Φ_2	Linear Lagrange interpolation functions
ξ	Normalised element coordinates
$\Psi_1^0, \Psi_1^1, \Psi_2^0, \Psi_2^1$	Cubic Hermite interpolation functions
\mathcal{F}	Face Fitting objective function
\mathcal{H}	Host Mesh Fitting objective function
\mathbf{T}	4×4 transformation matrix
\mathbf{R}	3×3 rotation matrix
\mathbf{t}	3×1 translation vector
ψ, θ, ϕ	Cardan angles
α, β, γ	Joint angles
\mathcal{D}	Direct Least-Squares Method objective function
\mathbf{F}	Deformation gradient tensor
\mathbf{U}	Right symmetric stretch tensor
\mathbf{v}	Left symmetric stretch tensor
\mathbf{C}	Right Cauchy-Green strain tensor
\mathbf{b}	Left Cauchy-Green strain tensor
$\delta\omega$	Virtual work of forces acting on a body
σ	Cauchy stress tensor
Ψ	Strain-energy density function
$c_{1,2}$	Mooney-Rivlin parameters

LIST OF TABLES

\mathcal{V}	Volume of Finite Element Mesh
Δf	Standard deviation (error) in variable f
\mathbf{m}_i^g	Global coordinates of muscle attachment point i
l	Muscle-tendon length
\mathcal{S}	Singular Value Decomposition objective function

List of Acronyms

ABI	Auckland Bioengineering Institute
CP	Cerebral Palsy
CT	Computer Tomography
DICOM	Digital Imaging and Communications in Medicine
DOF	Degree(s) of Freedom
FE	Finite Element
FF	Face Fitting
GMFC	Gross Motor Function Classification
GUI	Graphical User Interface
HMF	Host Mesh Fitting
ISB	International Society of Biomechanics
IUPS	International Union of Physiological Sciences
MRI	Magnetic Resonance Imaging
RMS	Root Mean Squared
SD	Standard Deviation
STA	Soft Tissue Artefact(s)
VRML	Virtual Reality Modeling Language

1

Introduction

1.1 Motivation

The analysis of human walking has a long history, probably starting in ancient Greece with Aristotle's treatise *About the Movement of Animals* where he writes: "If a man were to walk parallel to a wall in sunshine, the line described by the shadow of his head would not be straight but zigzag." However, the study of human walking remained an observational one until the invention of moving images as important new scientific tools in the late 19th century (Paul, 1998). The explosion of experimental methods for quantifying walking and the development of computers in the 20th century allowed results to be produced in minutes rather than days and gait analysis to be introduced into clinical settings (Andriacchi & Alexander, 2000).

Winter (1990) gives a basic definition of walking as "a method of locomotion involving the use of the two legs, alternately, to provide support and propulsion". However, successful walking is not as simple as it sounds and depends on a coordinated interplay of numerous muscles crossing several joints. The hierarchical system of motor controls begins in the cerebral cortex and ends at the motor neuron. The mechanical performance of each muscle actuator is predetermined by its geometric and material properties, and alterations in the musculoskeletal system affect the resulting motion pattern upon active muscle contraction (Lieber & Friden, 2000). To date, physiological measurements of muscle structures in vivo have been fundamentally limited, and detailed analyses of the musculoskeletal system during walking crucially depend on computational

modelling. Investigations of muscle functioning are of special importance in a medical context if musculoskeletal impairments result in pathological gait.

Skeletal muscle structures in gait analysis have commonly been modelled as a series of points connected by straight-line segments with no consideration for the 3D architecture (Anderson & Pandy, 2001; Damsgaard et al., 2006; Delp & Loan, 1995). Investigations of muscle-tendon lengths during walking using straight-line models based on adult male dimensions have been performed numerously in children with Cerebral Palsy (CP)¹, aimed at improving treatment decision making and better evaluating surgical procedures (Molenaers et al., 2006). However, concerns have been expressed in terms of the accuracy of straight-line models, and caution is suggested when interpreting the results, especially for muscles with complex geometries and broad areas of attachment (Blemker & Delp, 2005; Scheepers et al., 1997; Wren et al., 2004).

More accurate anatomically-based models of the muscle continuum have been developed in biomechanics, orthopaedics and computer graphics research. Thereby, significant work has been done to derive the deformation of the muscle continuum based on kinematic data using the Finite Element (FE) method (Blemker & Delp, 2006; Roehrlé & Pullan, 2007; Teran et al., 2005). Results from FE analyses suggest that the complex architectures and anisotropic material properties of skeletal muscles significantly affect the directions of muscle forces acting on the muscle-bone boundary (Roehrlé & Pullan, 2007). However, the non-linear relationship between the muscle deformation and the internal stresses have led to computationally very expensive models; even more so if contact between muscle structures is needed to be taken into account. Hence, studies, which have deployed the FE method in finite elasticity, have generally been confined to simple motor tasks or only a few muscle structures (Blemker & Delp, 2006; Roehrlé & Pullan, 2007).

Subject-specific, anatomically-based modelling techniques have not yet been successfully applied to children, and the prediction of muscle soft-tissue deformation during walking using anatomically-based models remains a major challenge despite efforts in many research areas. The modelling techniques for investigating muscle functioning during walking have either only captured the muscle-tendon paths without taking the 3D muscle architectures into account, or have been

¹A heterogeneous collection of clinical syndromes caused by a non-progressive lesion in the immature brain and characterised by progressive abnormal motor patterns and postures (Graham & Selber, 2003).

computationally too complex to be applied to gait analysis. To date, no modelling approach has been shown to efficiently and accurately help surgeons coping with the diversity of musculoskeletal impairments observed in children with CP.

1.2 Aim

The present PhD study has built on a combined effort between the Auckland Bio-engineering Institute (ABI) and the Department of Surgery, University of Auckland, for introducing anatomically-based, subject-specific modelling techniques into clinical gait analysis. In particular, the potential use of anatomically-based models in medical research related to CP was explored. The present study extends the work of Fernandez (2004) which was also performed at the ABI. In a preliminary study, Fernandez et al. (2005) successfully predicted the lengths in two lower limb muscles during walking using anatomically-based modelling techniques in combination with kinematic data from gait analysis.

Research at the ABI has strongly focused on the International Union of Physiological Sciences (IUPS) Physiome Project², which has promoted the development of anatomically-based models for analysing the human physiology from cell level up to whole organs. As part of the IUPS Physiome Project, the present study aimed at deploying the capabilities of the modelling environment CMISS³ for modelling lower limb motion during gait. The modelling software CMISS has been a major component of the ABI's effort within the IUPS Physiome Project, allowing the development and visualisation of anatomically-based models, the customisation of the models to subject-specific data, and the analysis of finite deformations. CMISS consists of a number of modules including a graphical frontend called CMGUI, which is a 3D visualisation software package with advanced modelling capabilities, and a computational backend called CM, which can remotely run on powerful workstations or supercomputers.

Ethical approval was obtained from the New Zealand Northern Y Regional Ethics Committee on the 8th of September 2006, reference number NTY/06/07/064, in order to acquire data of children with CP and a group of typically-developing children. A copy of the ethical approval letter is provided in the Appendix A.

²<http://www.physiome.org.nz>

³An interactive computer program for Continuum Mechanics, Image analysis, Signal processing and System identification developed at the ABI (<http://www.cmiss.org/>).

Data acquisition included a Magnetic Resonance Imaging (MRI) scan of the lower limbs at the Centre for Advanced MRI, University of Auckland, and gait analysis at the Biomechanics and Gait Laboratory, Department of Sport and Exercise Science, University of Auckland. More insights into clinical gait analysis were gained during a one-month visit at the Hugh William Gait Laboratory, Murdoch Children's Research Institute, Victoria, Australia, held in February 2008.

1.3 Thesis Overview

In order to reach the objective of the present work, interdisciplinary skills had to be acquired in (i) anatomically-based, subject-specific modelling, (ii) clinical gait analysis and (iii) finite deformation techniques for soft-tissue muscle models. The Theoretical Background related to these three areas is established in Chapter 3, subsequent to the Introduction in Chapter 1 and the Literature Review in Chapter 2.

Chapter 1 outlines the motivation behind the present work, specifies the main objectives, gives a thesis overview and lists the thesis contributions.

Chapter 2 provides a general literature review of the current state of knowledge in the research areas of clinical gait analysis, anatomically-based, subject-specific modelling and CP.

Chapter 3 is divided into three sections describing the theoretical background in (i) developing anatomically-based, subject-specific models from medical images, (ii) deriving segmental and joint kinematics from optical motion capture data and (iii) deforming anatomically-based FE models based on segmental kinematics. Each section concludes with a short summary.

The acquired skills, outlined in Chapter 3, are applied to four different studies in the Chapters 4 - 7 with the overall goal of introducing anatomically-based, subject-specific modelling of lower limb motion during gait into clinical research related to CP.

Chapter 4 outlines a study for the development of a library of anatomically-based, subject-specific models of children with and without CP, and the investigation of the differences in lower limb muscle volumes and muscle lengths between the two groups.

Chapter 5 depicts a study for the prediction and validation of soft-tissue muscle deformation in the lower limbs during walking by combining anatomically-based, subject-specific modelling techniques with data from optical motion capture.

Chapter 6 details a study for the introduction of an analytical approach to estimate the error propagation from kinematic data to modelled muscle-tendon lengths during walking.

Chapter 7 describes a study for the development of an interactive, web-based teaching tool for gait courses. In particular, the muscle activation patterns during walking were aimed to be visualised using the anatomically-based model of the lower limbs described in Chapter 5.

The Chapters 4 - 7 are each divided into Introduction, Method, Results and Discussion. The Introduction includes a specific literature review related to the particular study. The Method provides more information to the subjects, refers to relevant techniques introduced in Chapter 3 and outlines new methods which have been developed in the specific context.

A Conclusion is given in Chapter 8, which is the last chapter of the present work.

Chapter 8 provides a summary of the four studies, analyses their impact in the context of clinical research related to CP, outlines limitations and addresses future investigations that may emerge.

1.4 Thesis Contributions

The following papers have been successfully published as research articles in scientific journals or conference proceedings:

- Oberhofer, K., Mithraratne, K., Stott, S., and Anderson, I. A., 2009. *Anatomically-based musculoskeletal modelling: prediction and validation of muscle deformation during walking*. The Visual Computer, 2009, p. 1-11, published online first
- Oberhofer, K., Mithraratne, K., Stott, S., and Anderson, I. A., 2009. *Error propagation from kinematic data to modelled muscle-tendon lengths during walking*. Journal of Biomechanics, 5;42(1), p. 77-81

CHAPTER 1. INTRODUCTION

- Oberhofer, K., Mithraratne, K., Walt, S., Stott, S., and Anderson, I. A., 2007. *A novel approach to compute muscle length during walking using subject-specific musculoskeletal models*. IASTED Proceedings Applied Simulation and Modelling, p. 451-456

The following papers have been submitted to be published as research articles in scientific journals:

- Oberhofer, K., Mithraratne, K., Stott, S., and Anderson, I. A., 2009. *Subject-Specific Modelling of Lower Limb Muscles in Children with Cerebral Palsy*. Clinical Biomechanics, submitted

The following oral presentations have been given at international conferences:

- 4th Asian Pacific Conference on Biomechanics, *Comparison Between Two Modelling Techniques in Predicting Muscle-Tendon Lengths Changes During Walking*. Christchurch, New Zealand, 14-17 April, 2009
- Workshop on 3D Physiological Human, *Anatomically-based musculoskeletal modelling: prediction and validation of muscle deformation during walking*. Zermatt, Switzerland, 1-4 Dec, 2008
- 10th Symposium on 3D Analysis of Human Movement. *Anatomically-based finite element modelling of muscle structures during walking*. Santpoort-Amsterdam, Holland, 29-31 Oct, 2008
- 13th Annual Scientific Meeting of the Australian and New Zealand Orthopaedic Research Society. *Musculoskeletal modelling of the lower limbs to investigate gait of children with cerebral palsy*. Auckland, New Zealand, 17-18 Oct, 2007
- 6th Annual Meeting of the European Society of Movement Analysis for Adults and Children. *Subject-specific musculoskeletal models for computation of muscle lengths during walking in children with cerebral palsy*. Athens, Greece, 27-29 Sep, 2007
- 16th International Conference on Applied Simulation and Modelling. *A novel approach to compute muscle length during walking using subject-specific musculoskeletal models*. Palma de Mallorca, Spain, 29-31 Aug, 2007

2

Literature Review

The following literature review provides a general introduction into previous research in (i) clinical gait analysis, (ii) anatomically-based, subject-specific modelling and (iii) CP. More specific literature reviews are given in the first sections of Chapters 4 - 7 in the context of the four studies which have emerged from the present work. Keywords which were used for searching the literature included *Lower Limbs, Skeletal Muscle, Walking, Human Locomotion, Optical Motion Capture, Gait Analysis, Muscle-Tendon Length, Musculoskeletal Modelling, Anatomically-Based, Finite Element Method, Soft-Tissue Deformation, Subject-Specific, Magnetic Resonance Imaging, Cerebral Palsy, Spasticity*.

2.1 Clinical Gait Analysis

Clinical gait analysis aims to quantitatively assess the degree of impairment in patients with gait disorders and compare the results with normal gait¹. Clinical gait analysis comprises the acquisition of kinematic data from optical motion capture, kinetic data from dynamometers such as force plates, muscle activity from electromyography, and in recent times, measures of metabolic expenditure from indirect calorimetry (Sutherland, 2001, 2002, 2005). The introduction of clinical gait analysis in the assessment of children with CP has led to changes in surgical recommendations and postoperative treatments (Andriacchi & Alexander, 2000), a reduction in the number of surgical procedures (Molenaers et al., 2006; Simon, 2004), and hence, a reduction in the total medical costs.

¹ *Gait* is generally used to describe a particular manner or style of walking; the term *normal gait* refers those qualitative and quantitative parameters that have been generalised across sex, age and anthropometric variables by means of gait analysis (Medved, 2001).

Kinematics, or the study of motion, has always been central to clinical gait analysis, and has evolved around the measurement of segmental displacements based on externally trackable body points (Sutherland, 2002). Joint angles have been derived from kinematic measurements by representing the human body as system of rigid segments connected by idealised joints (Nigg & Herzog, 1999). The comparison of clinically meaningful joint angles during walking in healthy subjects and patients with walking disorders has set the standards for the categorisation of walking into normal and pathological gait (Sutherland, 2002).

The extension of rigid body models to include muscle structures has been a relevant objective in gait analysis for many years, targeting at the derivation of physiological parameters such as muscle-tendon lengths and muscle forces during walking (Cappozzo et al., 2005; Nigg & Herzog, 1999). The quantification of muscle functioning has been of particular importance in the clinical analysis of pathological gait that is caused by neuromuscular disorders. However, in order for computational models to be useful in clinical settings, output measures have to be received in a timely efficient and understandable manner without the need for high expertise in computational modelling (Simon, 2004). It was not until the introduction of the modelling software SIMM² that musculoskeletal models found more widespread use in clinical gait analysis (Andriacchi & Alexander, 2000).

SIMM is a graphics-based software system which was developed by Delp & Loan (1995) to facilitate the development and analysis of musculoskeletal models in motion. The software can nowadays be coupled with commercially available optical motion capture systems, and part of its functionalities have been released open source under the name OpenSIMM³. The geometry of each muscle-tendon structure in SIMM is defined by a series of points which are connected by straight-line segments. The muscle-tendon path around joints can be further prescribed using so-called wrapping surfaces, Fig. 2.1. Joint kinematics from optical motion capture are commonly used as input data to quantify the effects of skeletal motion on the muscle-tendon geometry and function during walking.

Several studies have used SIMM for investigations of muscle-tendon lengths and lengthening velocities during walking in children with CP (Arnold et al., 2005, 2006b,a; Delp et al., 1996; Jonkers et al., 2006; Wren et al., 2004). Most studies have relied on a generic musculoskeletal model based on adult male dimen-

²Software for Interactive Musculoskeletal Modelling
(MusculoGraphics Inc., <http://www.musculographics.com>)

³<http://simtk.org>

sions and have only crudely scaled the model to subject-specific data from gait analysis. Two studies assessed the influence of variations in musculoskeletal geometry on psoas and hamstring lengths. Psoas lengths during walking were found to be sensitive to an altered femoral architecture due to age or bone deformities (Arnold et al., 2001; Scheepers et al., 1997). For three of four subjects, the generic model underestimated the normalised lengths of psoas throughout gait and scaling of the model along the anatomical axes did not improve the results (Arnold et al., 2001). No study has been done to determine if skeletal deformities affect the lengths of muscles other than psoas and hamstrings.

Further attempts have been made to introduce musculoskeletal models into clinical gait analysis (Chao et al., 2007; Damsgaard et al., 2006; Fernandez et al., 2005). However, the development of musculoskeletal models which enable the analysis of muscle functioning during walking in clinical settings poses several challenges including accurate representation of the musculoskeletal system, efficient algorithms, convenient graphical user interfaces, and compatibility with output data from optical motion capture. The generic musculoskeletal model within SIMM has remained the leading approach in clinical gait analysis, even though it holds several limitations: the muscle-tendon geometry is represented as a series of 1D straight-line segments, the generic musculoskeletal model is generally crudely scaled to subject-specific geometries and the estimation of muscle-tendon lengths depends on the prior calculation of joint kinematics from optical motion capture data.

2.2 Anatomically-Based, Subject-Specific Modelling

More realistic anatomically-based models of the musculoskeletal system have been developed in biomechanics, orthopaedics and computer graphics research to predict muscle soft-tissue deformations during different motor tasks. The computer graphics community has often adopted triangular surface meshes with a linear interpolation scheme, and the deformation has been derived based on kinematic constraints without complying to the balance principles of physics. In contrast, the FE method has been the common approach in biomechanical studies involving large deformations of soft-tissue (Nash & Hunter, 2000). Thereby, the local coordinates of the discretised continuum have generally provided the basis for the discretisation of the governing equations of finite elasticity.

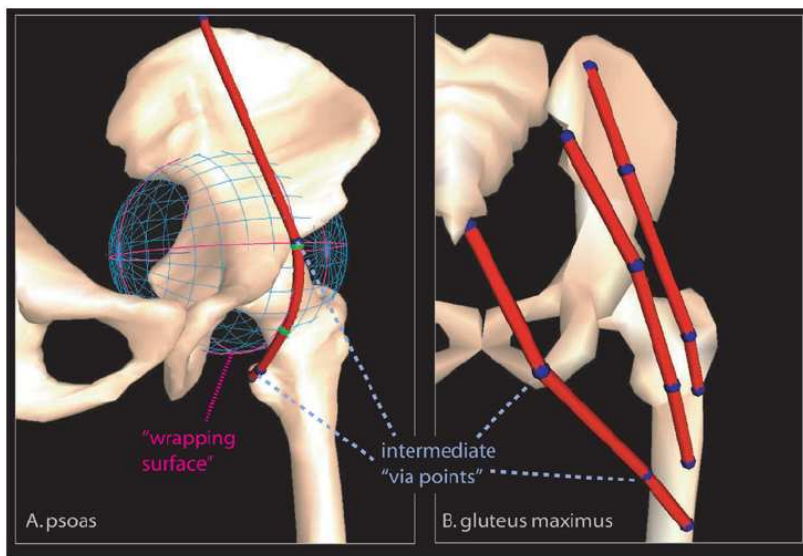


Figure 2.1: Series-of-line-segments simplification generally used in musculoskeletal modelling. The psoas muscle (A) has a complex path that bends, or wraps, around the pelvic brim, hip joint capsule and the femoral neck. With the 1D techniques, via-points (blue) and wrapping surfaces (wireframe) are used to prevent the muscles from penetrating these structures. However, it is difficult to define via points and wrapping surfaces that work robustly for multiple degrees of freedom. The gluteus maximus muscle (B) is also difficult to model because it has broad areas of attachment and the fibres have a complex geometric arrangement. Reprinted with kind permission from Springer Science + Business Media: *Annals of Biomedical Engineering, Three-Dimensional Representation of Complex Muscle Architecture and Geometries*, 33(5), 2005, 661-673, S. S. Blemker and S. L. Delp, Fig. 1.

2.2. ANATOMICALLY-BASED, SUBJECT-SPECIFIC MODELLING

The development of realistic 3D muscle models in computer graphics has been promoted by the growing interest in anatomically-based models in medical research and visualisation (Aubel & Thalmann, 2001; Dong et al., 2002; Scheepers et al., 1997). Thereby, muscles have commonly been modelled in two layers, i.e. an underlying line to define the path of action and a surrounding surface mesh to capture the geometry. The deformation of the muscle mesh has then been derived from the deformation of the action line, either purely based on geometric considerations (Scheepers et al., 1997) or by assigning lumped-parameter material properties to the action lines (Aubel & Thalmann, 2001). However, none of the two-layered models could address muscle-muscle penetration satisfactorily due to computational complexity involved in collision detection. Furthermore, triangular surface meshes have been limited in their use for any further biomechanical analyses.

Using the FE method, biomechanical studies on the muscle continuum have been performed for a few muscles and simple motor tasks including biceps brachii during elbow flexion-extension (Blemker et al., 2005), tibialis anterior during ankle plantar and dorsi flexion (Lemos et al., 2005), rectus femoris and vastus intermedius during knee flexion-extension (Blemker & Delp, 2006) and the masseter muscles during mastication (Roehrle & Pullan, 2007). Muscle tissue has commonly been modelled as an incompressible, transversely isotropic, hyperelastic material. The transversely isotropic properties have been obtained by modifying the stress components in the fibre direction of an isotropic material (Blemker et al., 2005; Lemos et al., 2005; Roehrle & Pullan, 2007). Studies on individual muscles in continuum mechanics have shown that the muscle architecture has a significant influence on the stress and strain distributions, and consequently, on the muscle's capacity to generate force.

Traditionally, linear functions have been used to interpolate the outer surfaces of musculoskeletal structures (Arnold et al., 2000; Aubel & Thalmann, 2001; Blemker et al., 2005; Lemos et al., 2005). A high number of elements is required to accurately capture the architecture of biological structures using linear elements, which leads to very large computational problems. In contrast, Bradley et al. (1997) demonstrated that the use of high-order, cubic interpolation functions had a number of advantages including a significant reduction in the total Degree(s) of Freedom (DOF) of the mesh without losing geometric accuracy. The resulting FE formulations for finite elasticity were shown to be less complex and solutions were obtained in a more efficient manner.

High-order FE models can be handled within the modelling software CMISS at all levels of the modelling process from fitting and customisation to mechanical simulations, post-processing and visualisation (Bradley et al., 1997; Fernandez et al., 2004; Roehrlé & Pullan, 2007). Fernandez et al. (2004) presented a collection of anatomically-based, high-order FE geometries of the musculoskeletal system based on the widely used Visible Human data set (Spitzer & Whitlock, 1998a), Fig. 2.2. The hierarchical modelling ontologies were aimed at contributing to the IUPS Physiome Project as part the ABI model library to facilitate data exchange among scientists.

Subject-specific, anatomically-based models have been developed from medical image data such as Computer Tomography (CT) or MRI using mesh generation algorithms for triangular surface meshes (Arnold et al., 2000; Teran et al., 2005) or fitting techniques for 3D FE models (Bradley et al., 1997; Fernandez et al., 2004). In particular, a fitting technique called the Host Mesh Fitting (HMF) technique allowed for customising an already existing generic FE model to a limited number of subject-specific data (Fernandez et al., 2004). The HMF methodology drew on the *free-form* idea of deriving the deformation of a complex mesh from the deformation of a surrounding simple mesh (Sederberg & Parry, 1986). However, the development of subject-specific models from medical images has often remained a time-consuming procedure because of the manual identification of muscle boundaries in each image slice. Most studies have either kept the number of subjects small (Arnold et al., 2000, 2001) or have introduced a generic musculoskeletal model based on the Visible Human data set (Fernandez et al., 2004; Roehrlé & Pullan, 2007; Teran et al., 2005).

Fernandez et al. (2005) adopted the HMF technique to predict muscle-tendon lengths of gastrocnemius and semimembranosus during walking in three subjects with CP using anatomically-based models and kinematic data from optical motion capture. Muscle soft-tissue deformation was derived from the deformation of a simple surrounding host mesh, and muscle-tendon length was calculated as average arc-length in longitudinal direction of the deformed muscle mesh. Despite promising results, the validity of the HMF technique for gait analysis has never been assessed, and its applicability to an entire model of the lower limbs has remained unclear. In particular, multi-body contact constraints were required to avoid penetration of structures into each other, thus, leading to a significant increase in model complexity upon addition of further muscle structures.

Undoubtedly, anatomically-based, subject-specific models of the musculoskeletal system offer many advantages over straight-line, generic models in providing new insights into the 3D architectures of skeletal muscles and their function during walking. However, the non-linear material properties of muscle tissue, the complex paths of muscles across several joints, the large deformations that occur during gait, and the interaction of individual muscle structures with surrounding tissue pose major challenges. Musculoskeletal models, which are meant to be useful in clinical gait analysis, need to consider all muscles which could contribute to pathological gait. To date, none of the proposed modelling methods for anatomically-based FE models has enabled the accurate deformation of more than two muscles throughout gait. Furthermore, the development of anatomically-based, subject-specific musculoskeletal models of children with CP has been very limited and most studies have adopted generic models based on the Visible Human data set for their analyses.

2.3 Cerebral Palsy

CP results from a non-progressive lesion in the developing brain, which often leads to spasticity in skeletal muscles, Fig. 2.3. Spasticity is associated with a hyperexcitability of the stretch reflex, resulting in a velocity-dependent increase in muscle tone, stiffness, and eventually fixed contractures (Foran et al., 2005; Scholtès et al., 2006). The progressive musculoskeletal impairments often lead to impaired gait and contribute to a decline in mobility in most affected patients. Despite medical advances, the incidence of CP has remained unchanged or has even increased in recent decades (Gage, 2004). Higher survival rates due to better medical health care or increased usage of artificial fertilisation techniques may be reasons for this tendency.

One of the most striking features of CP is the diversity of gait deviations observed (Rodda & Graham, 2001). Depending on the location of the brain injury, different muscles are affected and spasticity may occur on one side of the body, a condition termed *hemiplegic CP*, or on both sides of the body, a condition termed *diplegic CP*. According to Rodda & Graham (2001), the basis of most pathological gait patterns is *toe walking* or *equinus gait*, resulting from a contracture of gastrocnemius and soleus. The transition from equinus gait to *crouch gait* is seen in many children with severe spastic diplegia CP, whereby crouch gait is associ-

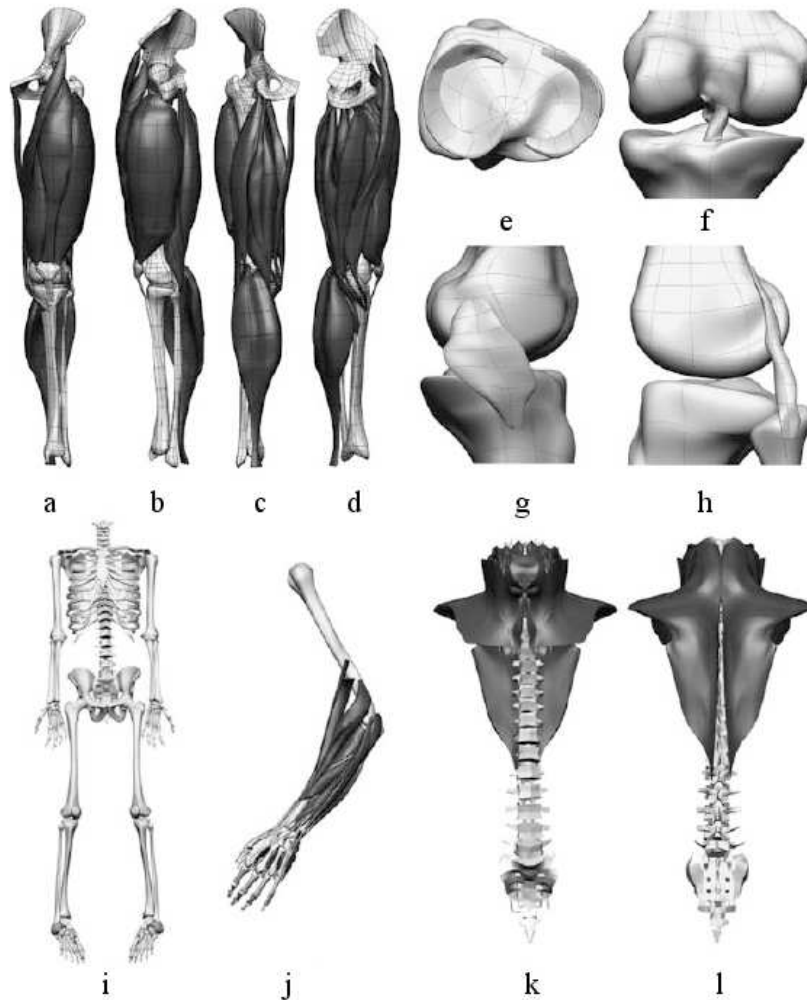


Figure 2.2: A collection of anatomically-based models based on the Visible Human data set including the lower limb bones and skeletal muscles crossing the knee joint shown from anterior, lateral, posterior and medial views (a-d). The knee joint showing the menisci, the cruciate ligaments, the tibial ligament and the fibular ligament (e-h), the skeleton frame (i), muscles of the left forearm (j) and the muscles of the neck, shoulder and back from the anterior and posterior view (k-l). Reprinted with kind permission from Springer Science + Business Media: *Biomechanics and Modeling in Mechanobiology, Anatomically based geometric modelling of the musculo-skeletal system and other organs*, 2, 2004, 139-155, J.W. Fernandez, P. Mithraratne, S.F. Trupp, M.H. Tawhai, P.J. Hunter, Fig. 10.

ated with a contraction of the hamstrings and psoas. However, a categorisation of the gait deviations in children with CP into specific patterns is difficult, which complicates the treatment decision making process (Dobson et al., 2007).

The primary aim in the management of the musculoskeletal impairments in children with CP is to prevent the development of contractures and fixed deformities (Graham & Selber, 2003). Common methods to assess the degree of dynamic and fixed contractures include physical examination, observational analysis of walking, and clinical gait analysis. In a review study by Scholtes et al. (2006), thirteen clinical instruments were identified to assess spasticity in children with CP by passively stretch the muscles of interest during physical examination. However, most methods did not comply with the concept of spasticity as a velocity-dependent increase in muscle tone, and the testing posture of the patients was seldom standardised.

The most widely used treatment methods are Botulinum Toxin Type A injections for dynamic contractures, and orthopaedic surgery involving muscle-tendon lengthening for fixed contractures (Rodda & Graham, 2001). Thereby, children with distal involvements, such as equinus gait, are most often treated by lengthening of gastrocnemius and soleus, whereas children with proximal involvements, such as crouch gait, most often undergo more extensive multilevel surgeries (Graham & Selber, 2003). Non-operative treatments such as physical therapy, mobility aids or orthotics usually precede and accompany the more invasive procedures.

Spastic muscles in children with CP present structural alterations which are inconsistent with the changes that occur due to chronic increased or decreased stimulation (Foran et al., 2005; Lieber et al., 2004), but there is no agreement on the details of the structural changes that occur secondary to the neurological disorder (Lieber et al., 2004). Furthermore, the single muscle's contribution to the movement abnormality is not well understood, and the degree of lengthening and the impact a surgery has on gait are still poorly evaluated. Even though orthopaedic surgery undoubtedly improves function and quality of most patients' lives, evidence for the efficacy of most orthopaedic operations is still lacking (Graham & Selber, 2003).

The main difficulty in the assessment and management of children with CP arises from the limitations in measuring muscle functioning *in vivo*. Computational models of the musculoskeletal system have the potential to help identify spastic

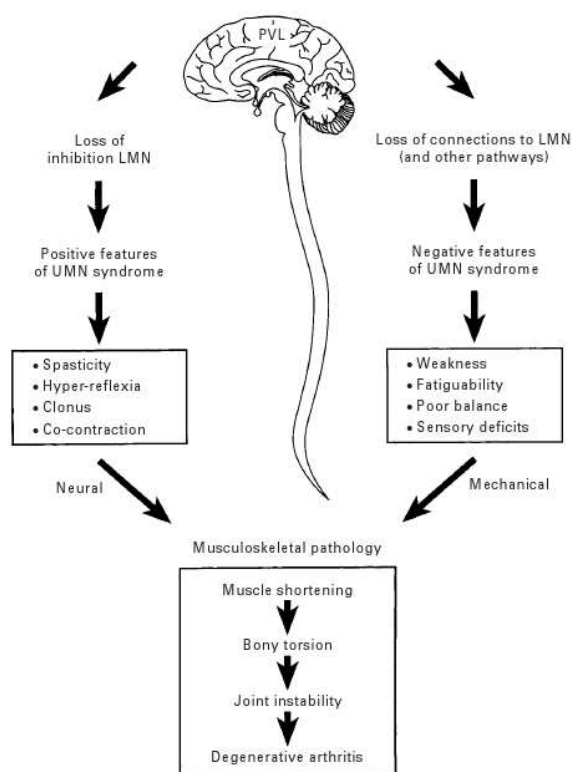


Figure 2.3: Diagram showing the neuromusculoskeletal pathology in CP. In motor terms, CP results in an Upper Motor Neurone (UMN) lesion which in this diagram is considered to have a series of positive and negative features that interact to produce the familiar musculoskeletal pathology. Historically, clinicians have concentrated on the positive features and the negative features have been relatively ignored. It is probable that the optimum management of children with CP will require integrated management of both the positive features and the negative features. Reproduced with permission and copyright © of the British Editorial Society of Bone and Joint Surgery (Graham & Selber, 2003).

muscles in children with CP, and define the correct surgical procedure based on data from clinical gait analysis. However, commonly used musculoskeletal models in gait analysis have not allowed for detailed studies of the muscle architecture and function during walking, and their clinical use has been limited. Advancements in the assessment and management of children with CP crucially depend on the improvement and the successful application of anatomically-based, subject-specific modelling techniques to clinical settings.

3

Theoretical Background

The following chapter provides the theoretical background for (i) developing anatomically-based, subject-specific models of the lower limbs from medical images, (ii) deriving segmental and joint kinematics from optical motion capture data, and (iii) deforming anatomically-based FE models based on segmental kinematics. Each section concludes with a short summary which emphasises the most important aspects of the outlined techniques. The theoretical framework is later applied to four different studies in the Chapters 4 - 7, aiming to explore the potential use of anatomically-based modelling in clinical gait analysis and medical research related to CP.

3.1 Development of Anatomically-Based, Subject-Specific Models of the Lower Limbs

The development of anatomically-based, subject-specific models of the lower limbs comprises four steps: (i) the acquisition of medical images such as MRI, (ii) the digitisation of the structures of interest, (iii) the discretisation of the geometry into a finite number of elements and (iv) the fitting of the initial mesh to the subject-specific image data.

3.1.1 Magnetic Resonance Imaging (MRI)

MRI is a medical imaging technique that enables the non-invasive acquisition of internal structures in vivo without exposing the subject to harmful radiation. MRI provides good contrast between the different soft-tissues of

the body, and consequently, allows for accurately assessing muscle and bone geometries at the same time (Moro-oka et al., 2007). Previous studies have used MRI for the development of subject-specific models of the lower limbs of adults and children (Arnold et al., 2000; Blemker & Delp, 2005; Elder et al., 2003; Lampe et al., 2006).

The standard MRI unit comes as a large cylinder-shaped tube with a moveable examination table that slides into its centre, Fig. 3.1. The scanned subject can either lie in prone or supine posture with the body part of interest in the centre of the tube. Straps and cushions may be used to help maintain the correct position during imaging. If large areas of the body are scanned, such as the lower limbs, the table needs to be repositioned during the scan, resulting in multiple image stacks. The stacks are assembled after the scan using the spatial position information of each image with respect to the MRI scanner.

The MRI scanner consists of three major components: a magnet, a radio frequency transmission system and gradient coils. The magnet is the largest and most expensive component of the scanner, and the remainder of the scanner is built around it. The radio frequency transmission system is usually built into the body of the scanner and consists of a synthesiser, power amplifier and transmitter coils. A variety of coils, including transmitter and gradient coils, are available to be fitted around smaller parts of the body such as the knee.

MRI is based on the principle of nuclear magnetic resonance in particular of hydrogen atoms (Young, 1987). In brief, nuclear magnetic fields align with an externally applied magnetic field which creates a magnetic vector. Radio frequency pulses are then used to deflect the magnetic vector. When the pulses are switched off, the magnetic vector returns to its resting state thereby emitting a radio frequency signal that can be detected by the gradient coils and used to create a diagnostic image (Berger, 2002). Different tissues relax at different rates when the transmitted radio frequency pulse is switched off. Depending on the medical context, different sequence parameters (TR, TE, flip angle, field of view matrix) are chosen to optimise contrast and spatial resolution of the images.

Artefacts impair image quality, lead to a loss of diagnostic information and can make it difficult to recognise the boundaries of internal structures. One of the main causes of artefacts is physiological movement such as respiratory motion or physical movement of subjects. Motion artefacts can be prevented by restricting acquisition time or restricting the movement of the subject using cushions and

3.1. DEVELOPMENT OF ANATOMICALLY-BASED MODELS



Figure 3.1: MRI data acquisition using a Siemens MAGNETOM Avanto System at the Centre for Advanced MRI, Faculty of Medical and Health Sciences, University of Auckland, New Zealand.

straps. Prevention of motion artefacts, without using chemical sedation, requires the active cooperation of the subject.

In general, MRI examination poses almost no health risks when appropriate safety guidelines are followed. Medical implants such as pacemakers, insulin pumps or metallic implants pose potential risks and safety aspects need to be considered on an individual basis. Due to the construction of the scanner, people with claustrophobia are sometimes unable to tolerate an MRI scan. Some management strategies for claustrophobic subjects include closing eyes, listening to music or chemical sedation. Each person has to fill in an MRI screening form and sign a consent form prior a scan.

3.1.2 Data Digitisation

MRI images are generally stored in the Digital Imaging and Communications in Medicine (DICOM) standard. DICOM facilitates access to medical images by ensuring interoperability between all medical imaging devices and electronic health record systems (John & Lim, 2007). DICOM files contain metadata such as image size, image dimension and equipment settings. The numerical computing environment MATLAB (The MathWorks Inc.) is capable to handle DICOM files and access the stored information. The Java-based image processing and

analysis software ImageJ¹ can compress a series of DICOM images and supports standard image processing functions for smoothing, edge detection and contrast manipulation.

Multiple image stacks from MRI can be reconstructed and segmented within the modelling software CMISS given the compressed images and their spatial positions with respect to the scanner, Fig. 3.2. The reconstruction involves the definition of a corresponding stack of 2D linear elements using the MRI images for texturing. Image segmentation refers to the process of defining discrete points on the boundaries of anatomical structures and extracting their 3D coordinates with respect to a given coordinate system. Image segmentation results in clouds of data points which serve as basis for the development of subject-specific, parameterised (FE) models.

Image segmentation can either be done automatically or manually. Automatic image segmentation is only feasible if high contrast is provided between the structure of interest and the surrounding tissue. The boundaries between individual skeletal muscles are often difficult to identify because they are tightly packed within the human body. At the time of the model development, no automatic segmentation algorithm was available that enabled the robust and accurate segmentation of lower limb muscles from MRI. The manual identification of individual muscles is generally supported by cross-sectional photographs from medical textbooks, such as the Atlas of the Visible Human Male from the Visible Human Project (Spitzer & Whitlock, 1998b).

3.1.3 Finite Element Representation of the Geometry

The FE method provides a tool to mathematically approximate the geometry of a continuum by a finite number of elements (Zienkiewicz & Taylor, 2000). The discretisation of the continuum into finite elements is accomplished by specifying the location of certain material points (nodes) in space and then connecting the nodes to form elements. The variations in the spatial geometric coordinates are described as functions of element local coordinates with the local coordinates generally normalised to range from 0 to 1. The interpolation functions, also known as basis or shape functions, consist of polynomials of different degrees, depending on the desired accuracy of the approximation.

¹<http://rsbweb.nih.gov/ij/>

Linear or 1st order polynomials require one nodal parameter (DOF) to be defined, which is generally the nodal value \mathbf{u}_i , thus preserving continuity of the geometric coordinates (C_0 continuity) across element boundaries.

Cubic Hermite Basis Function

Given the same 1D element, the cubic interpolation of the geometric coordinates \mathbf{u} is defined as

$$\mathbf{u}(\xi) = \Psi_1^0(\xi)\mathbf{u}_1 + \Psi_1^1(\xi)\frac{\partial\mathbf{u}}{\partial\xi}|_1 + \Psi_2^0(\xi)\mathbf{u}_2 + \Psi_2^1(\xi)\frac{\partial\mathbf{u}}{\partial\xi}|_2 \quad , \quad (3.3)$$

where Ψ_1^0 , Ψ_1^1 , Ψ_2^0 and Ψ_2^1 are known as the four cubic Hermite interpolation functions of the element coordinate $\xi \in [0, 1]$ given by

$$\begin{aligned} \Psi_1^0(\xi) &= 1 - 3\xi^2 + 2\xi^3 \quad , & \Psi_1^1(\xi) &= \xi(\xi - 1)^2 \quad , \\ \Psi_2^0(\xi) &= \xi^2(3 - 2\xi) \quad , & \Psi_2^1(\xi) &= \xi^2(\xi - 1) \quad . \end{aligned} \quad (3.4)$$

Subscript 1 and 2 refer to node numbers and superscripts 0 and 1 are the zeroth and first derivatives, respectively.

In contrast to a linear interpolation, cubic or 3rd order polynomials also preserve continuity of the first derivatives of the geometric coordinates with respect to element local coordinates (C_1 continuity). C_1 continuity offers many advantages in constructing FE geometries of biological tissue because it allows the realistic representation of complex geometries with a minimum number of elements (Bradley et al., 1997).

However, preserving C_1 continuity does not ensure continuity of the derivatives in the spatial domain. In particular, discontinuity will arise when two adjacent elements are of unequal physical lengths. Hence, continuity is in practice preserved with respect to a physically more meaningful parameter such as arc-length (G_1 -continuity). The ξ -derivatives, Eq. 3.3, are then rewritten as

$$\frac{\partial\mathbf{u}}{\partial\xi}|_n = \frac{\partial\mathbf{u}}{\partial s}|_{\Delta(n,e)} \cdot \frac{ds}{d\xi}|_e \quad , \quad (3.5)$$

where $\Delta(n, e)$ is the global node number of node n in element e , and $\frac{ds}{d\xi}|_e$ is termed an element scale factor which scales the arc-length derivative to the ξ -derivative.

C_1 continuity is achieved by defining the scale factors to be the same for neighbouring elements. In theory, the scale factor can have any value as long as it is nodally based. However, average arc-length scaling across two elements is often chosen to achieve a uniform spacing of ξ with respect to arc-length (Bradley et al., 1997).

Interpolation in Higher Dimensions

The bicubic Hermite interpolation function for a 2D element is formed from the tensor product of two 1D cubic Hermite basis functions, Eq. 3.3. The bicubic Hermite interpolation of the geometric coordinates \mathbf{u} within a 2D element connecting four nodes (1, 2, 3, 4) is then given as

$$\begin{aligned}
 \mathbf{u}(\xi_1, \xi_2) = & \Psi_1^0(\xi_1)\Psi_1^0(\xi_2)\mathbf{u}_1 + \Psi_2^0(\xi_1)\Psi_1^0(\xi_2)\mathbf{u}_2 & (3.6) \\
 & + \Psi_1^0(\xi_1)\Psi_2^0(\xi_2)\mathbf{u}_3 + \Psi_2^0(\xi_1)\Psi_2^0(\xi_2)\mathbf{u}_4 \\
 & + \Psi_1^1(\xi_1)\Psi_1^0(\xi_2)\frac{\partial\mathbf{u}}{\partial\xi_1}|_1 + \Psi_2^1(\xi_1)\Psi_1^0(\xi_2)\frac{\partial\mathbf{u}}{\partial\xi_1}|_2 \\
 & + \Psi_1^1(\xi_1)\Psi_2^0(\xi_2)\frac{\partial\mathbf{u}}{\partial\xi_1}|_3 + \Psi_2^1(\xi_1)\Psi_2^0(\xi_2)\frac{\partial\mathbf{u}}{\partial\xi_1}|_4 \\
 & + \Psi_1^0(\xi_1)\Psi_1^1(\xi_2)\frac{\partial\mathbf{u}}{\partial\xi_2}|_1 + \Psi_2^0(\xi_1)\Psi_1^1(\xi_2)\frac{\partial\mathbf{u}}{\partial\xi_2}|_2 \\
 & + \Psi_1^0(\xi_1)\Psi_2^1(\xi_2)\frac{\partial\mathbf{u}}{\partial\xi_2}|_3 + \Psi_2^0(\xi_1)\Psi_2^1(\xi_2)\frac{\partial\mathbf{u}}{\partial\xi_2}|_4 \\
 & + \Psi_1^1(\xi_1)\Psi_1^1(\xi_2)\frac{\partial^2\mathbf{u}}{\partial\xi_1\partial\xi_2}|_1 + \Psi_2^1(\xi_1)\Psi_1^1(\xi_2)\frac{\partial^2\mathbf{u}}{\partial\xi_1\partial\xi_2}|_2 \\
 & + \Psi_1^1(\xi_1)\Psi_2^1(\xi_2)\frac{\partial^2\mathbf{u}}{\partial\xi_1\partial\xi_2}|_3 + \Psi_2^1(\xi_1)\Psi_2^1(\xi_2)\frac{\partial^2\mathbf{u}}{\partial\xi_1\partial\xi_2}|_4
 \end{aligned}$$

The bicubic-linear interpolation function for a 3D element is formed from the tensor product of two 1D cubic Hermite, Eq. 3.6, and one 1D linear interpolation function, Eq. 3.1. A bicubic-linear element has four nodal DOF in each spatial direction that are the spatial position, the first-order derivatives in ξ_1 and ξ_2 direction, and a cross derivative.

3.1.4 Fitting Techniques

Two different fitting techniques are feasible within the modelling environment CMISS for developing subject-specific, anatomically-based models of muscle and bone structures based on data from MRI. The methods are called Face Fitting (FF) and HMF respectively, and are outlined in the following.

Face Fitting (FF)

The FF technique entails the development of an initial FE mesh and the subsequent fitting of the initial mesh to the subject-specific data from MRI. The design of the initial mesh, that is the nodal DOF and the connectivity of elements, predetermines the success of the FF method. Hence, the development of an initial mesh is a crucial step which requires time and expertise.

The FF formulation is set up to find the optimum set of nodal DOF of the generic mesh so that the distances between the subject-specific data points and their projection points onto the external faces of the mesh are minimised in a least-squares sense, Fig. 3.3 (Fernandez et al., 2004). The FF objective function \mathcal{F} of an element face with a vector of nodal mesh parameters \mathbf{u}_n is of the form

$$\mathcal{F}(\mathbf{u}_n) = \sum_{d=1}^D [(\mathbf{u}(\xi_d) - \mathbf{z}_d)^T (\mathbf{u}(\xi_d) - \mathbf{z}_d)] + \mathcal{G}_{2D}(\mathbf{u}_n, \gamma_i) \quad , \quad (3.7)$$

where \mathbf{z}_d are the global coordinates of data point d , $\mathbf{u}(\xi_d)$ are the coordinates of its projection point expressed as functions of local face coordinates; and $\mathcal{G}_{2D}(\mathbf{u}_n, \gamma_i)$ is a 2D Sobolev smoothing constraint which imposes penalty parameters $\gamma_i \in [0, 1]$ to the arc-lengths ($i = 1, 2$), the arc-curvatures ($i = 3, 4$) and the face area ($i = 5$).

The best fit is found by differentiating the FF objective function, Eq. 3.7, with respect to each nodal face parameter \mathbf{u}_n and setting the resulting expression to zero

$$\frac{\partial \mathcal{F}(\mathbf{u}_n)}{\partial \mathbf{u}_n} = \sum_{d=1}^D \sum_{m=1}^M \sum_{n=1}^N [(\Psi_n(\xi_d) \mathbf{u}_n - \mathbf{z}_d) \cdot \Psi_m(\xi_d)] + \frac{\partial \mathcal{G}_{2D}(\mathbf{u}_n)}{\partial \mathbf{u}_n} = 0 \quad . \quad (3.8)$$

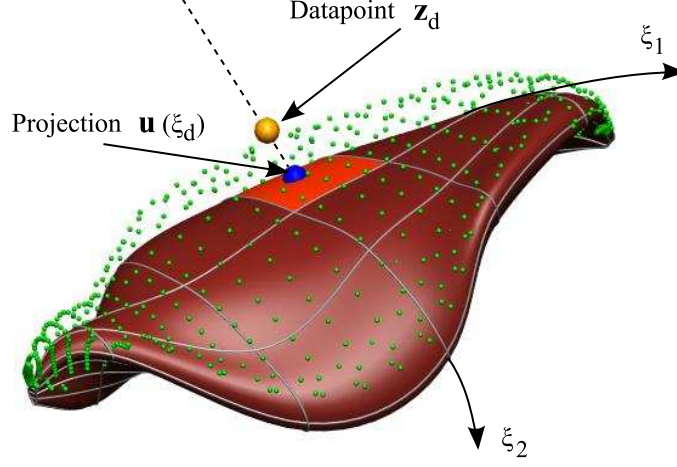


Figure 3.3: Projection of data point \mathbf{z}_d onto an element face with the element coordinates $\xi_i \in [0, 1]$ and resulting closest point $\mathbf{u}(\xi_d)$ for the FF technique.

Equation 3.8 is reformulated into a linear system of equations of the form $A_{mn}\mathbf{u}_n = B_m$ ($m = n$) where

$$\begin{aligned}
 A_{mn} &= \sum_{d=1}^D \sum_{m=1}^M \sum_{n=1}^N \Psi_M(\xi_d) \cdot \Psi_n(\xi_d) \quad , \\
 B_m &= \sum_{d=1}^D \sum_{m=1}^M \Psi_m(\xi_d) \cdot \mathbf{z}_d + \frac{\partial \mathcal{G}_{2D}(\mathbf{u}_n)}{\partial \mathbf{u}_n} \quad .
 \end{aligned}
 \tag{3.9}$$

The second term on the left-hand side of B_m , Eq. 3.9, which is the contribution of the Sobolev smoothing term, is numerically evaluated over the face using a scheme such as Gaussian quadrature. The face equations for all external faces of the generic mesh are assembled to form the global set of equations. Assemblage is carried out to satisfy continuity of the nodal parameters across faces.

In the case of cubic Hermite interpolation, the resulting expression is non-linear in \mathbf{u}_n because of the scale factors (arc lengths), which are non-linear functions of nodal face parameters. Solving a large number of non-linear equations is computationally expensive. It can be avoided by fixing the scale factors and iteratively solving the resulting linear equations until the Root Mean Squared (RMS) between the data and the projection points reaches a certain value,

Fig. 3.5. Thereby, scale factors are updated after each iteration, and the nodal parameters are modified accordingly. The modification of the mesh geometry results in a new optimum of the FF objective function for the next iteration.

The FF technique enables the generation of highly accurate subject-specific models if a large number of data points over the entire volume are given and if the data points are already closely aligned with the initial mesh. However, the initial projection of the data points onto the external faces is prone to errors if the data points are not in line with the initial mesh, and scarce data may result in physically unrealistic distortion of individual faces or whole regions of the mesh.

Host Mesh Fitting (HMF)

The HMF technique is a free-form deformation method that was introduced into the modelling software CMISS to customise an already existing, generic FE mesh to a limited number of subject-specific data (Fernandez et al., 2004). The anatomically-based models based on the Visible Human data set, Fig. 2.2, have commonly served as generic meshes for the development of subject-specific models. The concept behind any free-form deformation technique is the deformation of a complex mesh according to the fitting solution of a surrounding simple mesh (Sederberg & Parry, 1986). As the surrounding mesh generally constitutes less nodal DOF than the enclosed mesh, a limited number of subject-specific points are sufficient for obtaining a realistic solution. In the HMF, the enclosed FE mesh is termed *slave mesh* and the surrounding mesh is termed *host mesh*.

The HMF technique depends on the definition of so-called *landmark* and *target* points on the generic mesh and the subject-specific data respectively. The HMF objective function is then set up to minimise the distances between the *landmark* and *target* points in a least-squares sense, Fig. 3.4. Each pair of landmark and target point is preferably chosen as a unique feature of the biological structure, such as the prominence of the greater trochanter on femur. Between 30 and 50 well-positioned landmark and target points are needed to obtain reasonable solutions for the bones in the lower limbs.

The slave mesh and the landmark points need to be completely enclosed inside the host mesh. The nodal parameters of the slave mesh and the positions of the

landmark points can then be recorded as functions of local host mesh coordinates

$$\mathbf{u}(\xi) = \sum_{n=1}^N \Psi_n(\xi) \mathbf{u}_n \quad , \quad (3.10)$$

whereby \mathbf{u}_n is a vector of N host mesh nodal parameters associated with the interpolation functions Ψ_n . The HMF objective function \mathcal{H} is set to minimise the distances between landmarks and targets in a least-square sense as

$$\mathcal{H}(\mathbf{u}_n) = \sum_{d=1}^D \sum_{n=1}^N [(\Psi_n(\xi_d^l) \mathbf{u}_n - \mathbf{p}_d^t)^T (\Psi_n(\xi_d^l) \mathbf{u}_n - \mathbf{p}_d^t)] + \mathcal{G}_{3D}(\mathbf{u}_n) \quad , \quad (3.11)$$

where ξ_d^l denotes the local coordinates of the landmarks with respect to the host mesh and \mathbf{p}_d^t are the global coordinates of the targets. The second term in the objective function $\mathcal{G}_{3D}(\mathbf{u}_n)$ is the 3D Sobolev smoothing constraint which imposes preassigned penalty parameters $\gamma_i \in [0, 1]$ to the arc-lengths ($i = 1, \dots, 3$), the curvatures in element coordinate directions ($i = 4, \dots, 6$), the surfaces area terms ($i = 7, \dots, 9$) and the volume ($i = 10$) of the host.

The deformed host mesh configuration is found by differentiating Equation 3.11 with respect to each host mesh nodal parameter \mathbf{u}_n and setting the expression to zero

$$\frac{\partial \mathcal{H}(\mathbf{u}_n)}{\partial \mathbf{u}_n} = \sum_{d=1}^D \sum_{m=1}^M \sum_{n=1}^N [(\Psi_n(\xi_d^l) \mathbf{u}_n - \mathbf{p}_d^t) \cdot \Psi_m(\xi_d^l)] + \frac{\partial \mathcal{G}_{3D}(\mathbf{u}_n)}{\partial \mathbf{u}_n} = 0 \quad . \quad (3.12)$$

Equation 3.12 is reformulated into a linear system of equations of the form $A_{mn} \mathbf{u}_n = B_m$ ($m = n$) where

$$\begin{aligned} A_{mn} &= \sum_{d=1}^D \sum_{m=1}^M \sum_{n=1}^N \Psi_m(\xi_d^l) \cdot \Psi_n(\xi_d^l) \quad , \quad (3.13) \\ B_m &= \sum_{d=1}^D \sum_{m=1}^M \Psi_m(\xi_d^l) \cdot \mathbf{p}_d^t + \frac{\partial \mathcal{G}_{3D}(\mathbf{u}_n)}{\partial \mathbf{u}_n} \quad . \end{aligned}$$

Since local coordinates do not change during deformation, the nodal coordinates of the slave mesh in deformed state can readily be determined by substituting the deformed host mesh nodal parameters back into Equation 3.10, Fig. 3.5.

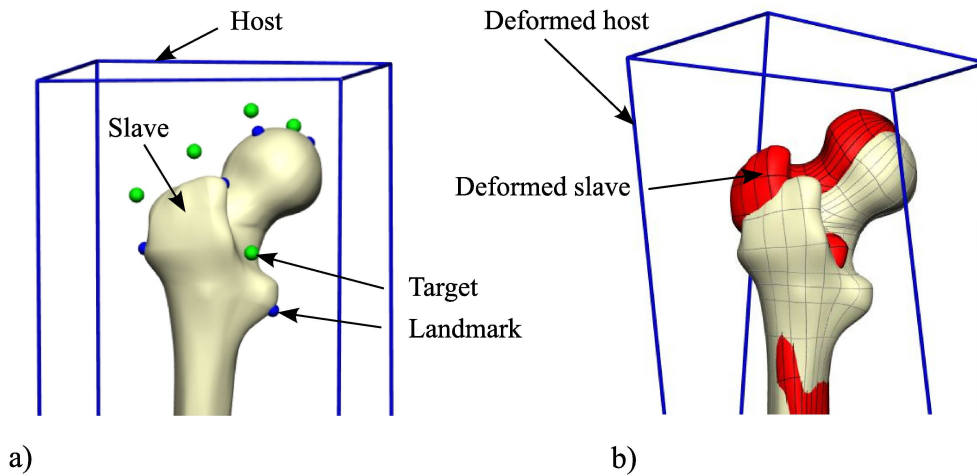


Figure 3.4: a) The FE model of the femur (slave mesh) based on the Visible Human data set embedded into a host mesh with landmark and target points defined on the slave mesh and on the subject-specific data respectively. b) The deformed host mesh and deformed femur according to the HMF solution.

Given the bicubic-linear interpolation scheme, not only nodal coordinates but also nodal derivatives and nodal cross derivatives of the slave mesh have to be updated. The calculation of the nodal derivatives is outlined in the Appendix B.

The success of the HMF technique largely depends on the design of the host mesh and the location and distribution of the landmark and target points. A high number of host mesh DOF will allow for capturing more details of the subject-specific geometries, provided that a sufficient number of landmark and target points are given. The development of the host mesh and the definition of the landmark and target points largely depend on experience and can only partly be based on objective criteria.

3.1.5 Summary

- MRI is an attractive method for obtaining subject-specific image data of bone and muscle structures without exposing the subject to harmful radiation. The choice of sequence parameters predetermines the quality of the images and should be done after consultation with experienced people in the field. Long image acquisition times should be avoided as they increase the risk of voluntary physical movement, leading to a loss in image clarity.

3.1. DEVELOPMENT OF ANATOMICALLY-BASED MODELS

- The image information from MRI, stored in the DICOM file format, can be converted and reconstructed within the modelling software CMISS. Bone and muscle structures can subsequently be digitised by manually defining the structures' boundaries. The resulting data clouds are used for the development of anatomically-based, parameterised (FE) models.
- The bicubic-linear interpolation scheme allows for approximating the geometries of bones and muscles by a finite number of elements. Cubic Hermite basis functions not only preserve continuity of the geometric coordinates across element boundaries but also of the first derivatives of the geometric coordinates with respect to the local element coordinates. As such, they allow for smoothly approximating a curved surface with a small number of elements.
- The FF and the HMF technique provide two fitting methods for developing subject-specific models based on the image data from MRI. The FF technique depends on the development of an initial mesh and on a high number of well-distributed data points from MRI. In contrast, the HMF technique makes use of an already existing generic mesh, and requires significantly fewer subject-specific data than the FF technique to lead in a reasonable fit. However, the HMF method is not capable to capture all subject-specific features in detail. Hence, the FF technique results in a more accurate solution than the HMF technique, provided that a sufficient number of data points are given and that they are already closely in line with the initial mesh.

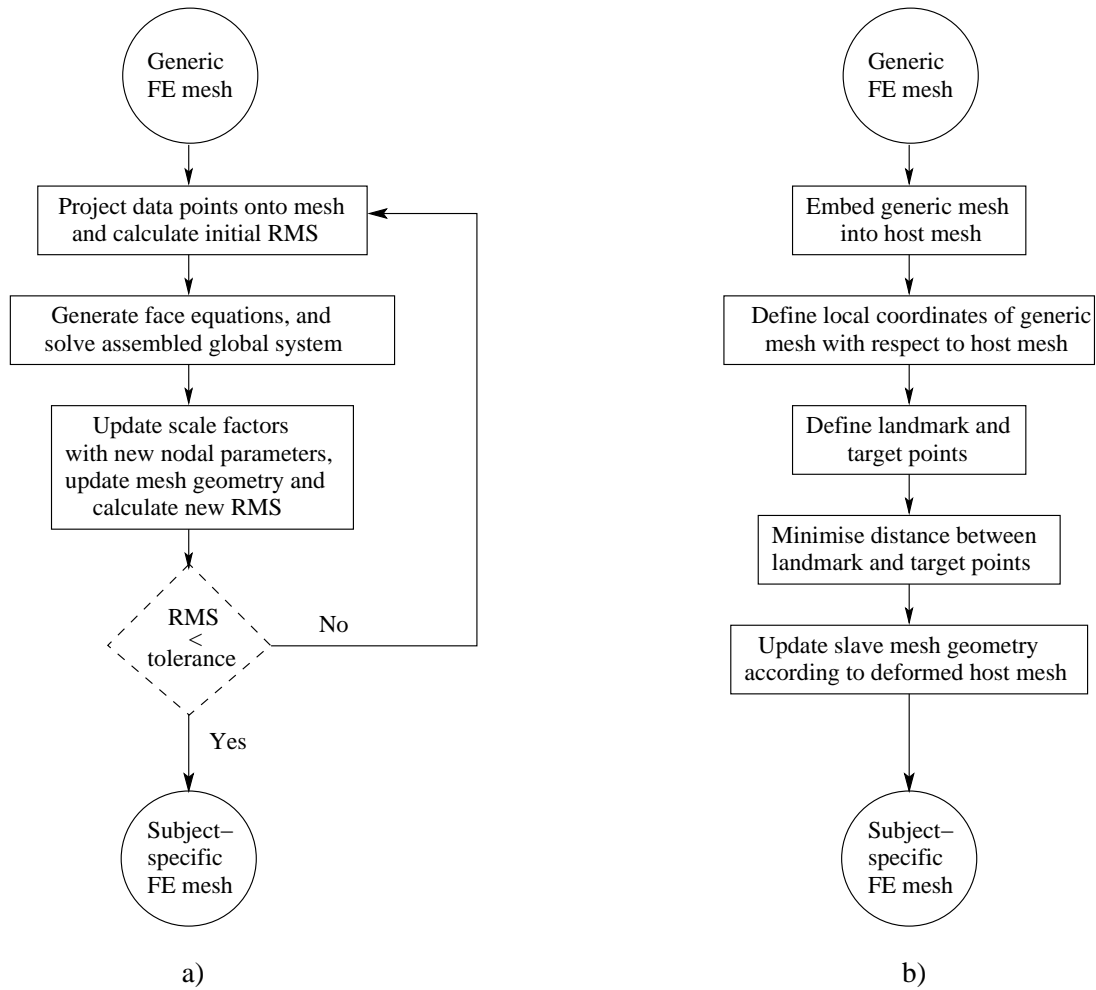


Figure 3.5: Flowchart of a) Face Fitting (FF) and b) Host Mesh Fitting (HMF).

3.2 Derivation of Segmental and Joint Kinematics During Walking

Bone structures are assumed to be rigid objects and their movement during walking can be approximated using kinematic data from optical motion capture. The following section details (i) the optical motion capture system, (ii) the definition of spatial and material coordinate systems, (iii) the derivation of segmental kinematics, (iv) the calculation of joint kinematics, and (v) the error sources of optical motion capture and optimisation strategies.

3.2.1 Optical Motion Capture System

Optical motion capture has found widespread use in 3D gait analysis, aiming the derivation of segmental and joint kinematics based on the positions of so-called *markers* which are attached to the skin. While a participant is walking, the marker positions are recorded in 3D space using several optical cameras which are distributed around the measurement field. The skeletal movement is then approximated from the marker positions under the assumption that the markers are rigidly attached to the underlying bones.

One of the main providers of optical motion capture systems is Vicon Motion Systems². The Vicon MX motion analysis system consists of 8 - 12 infrared cameras which are synchronised and linked to a control unit and then to a PC, Fig. 3.6. The Vicon retro-reflective markers come in various sizes from 25 mm spheres down to 3 mm hemispheres for capturing small objects. The markers can either be placed directly on the skin or mounted on fixtures which are attached to the body using, for instance, an elastic band, Fig. 3.6. Reflective markers should be visible to at least two cameras throughout the gait trial to allow for a reconstruction of the marker positions in 3D space. The cameras need to be calibrated to the measurement field prior to data acquisition in order to allow for an accurate reconstruction based on the optical information.

Different Vicon software packages are available for processing, analysing and summarising the captured data. In particular, the package Vicon Workstation is used to control the Vicon system, to calibrate the cameras, and to manage

²<http://www.vicon.com>



Figure 3.6: The Vicon MX motion analysis system at the Hugh Williamson Gait Laboratory, Victoria, Australia, showing a) the measurement field, b) an infrared camera and c) retro-reflective markers and different devices for attaching them.

and reconstruct the data. The package Vicon Bodybuilder allows for advanced data editing, for the definition of body segments based on a given marker set, and for exporting the marker trajectories in the ASCII file format for further external data processing. The two main file types which are handled within Vicon Software are .c3d files and .mkr files. The .c3d file is created during data capture and contains all the raw data and information related to a gait trial. The .mkr file specifies the labels to be used for a given marker set in Vicon Workstation.

Surface Marker Configuration

Different marker sets have been deployed in 3D gait analysis depending on the objective, the subjects and the external circumstances of a study. In theory, three

3.2. DERIVATION OF SEGMENTAL AND JOINT KINEMATICS

markers are sufficient for deriving the position and orientation of a rigid object in 3D space. However, skin markers are not rigidly connected to the underlying bones but move with the skin. Hence, more than three markers may be used on each segment to improve the approximation of the segment's position and orientation throughout walking.

The marker sets can roughly be divided into two groups: standard marker sets and customised marker sets. Standard marker sets have been developed for clinical purposes to facilitate motion capture in case of limited assessment time or in the presence of clinical gait patterns which complicate marker placement. The two main standard marker sets are the Helen Hayes marker set (Kadaba et al., 1989) and the Cleveland Clinic marker set (Sutherland, 2002). The Helen Hays marker set was developed in the mid eighties at the Helen Hayes Hospital, New York, USA, as part of the first clinical software for gait laboratories.

The Cleveland Clinic marker set was developed shortly after at the Cleveland Clinic Foundation, Ohio, USA. The marker set consists of 15 skin markers on anatomical landmarks of the lower limbs; and an additional 12 markers which are grouped in triads on rigid plates and wrapped around shank and thigh, Fig. 3.7a-c. Further markers, not shown in Figure 3.7, are placed on the shoulder, the elbow, the wrist and the head. Less variability in the transversal plane kinematics was observed for the Cleveland Clinic marker set when compared with the Helen Hays marker set (Sutherland, 2002).

With technological and methodological advancements and with increased awareness of the limitations of optical motion capture, the Helen Hays and Cleveland Clinical marker sets are nowadays redefined and new customised marker sets are introduced into clinical settings, Fig. 3.7d-i. Customised marker sets, generally consisting of a redundant number of markers, have been developed for research purposes. Optimisation algorithms, later discussed in this section, have then been adopted to determine segmental kinematics.

3.2.2 Spatial and Material Coordinate Systems

Different coordinate systems need to be defined in gait analysis to derive segmental and joint kinematics. The coordinate system which is fixed within the gait laboratory is also termed the *global*, *spatial* or *Eulerian* coordinate system. The infrared cameras are calibrated with respect to the spatial coordinate system, and

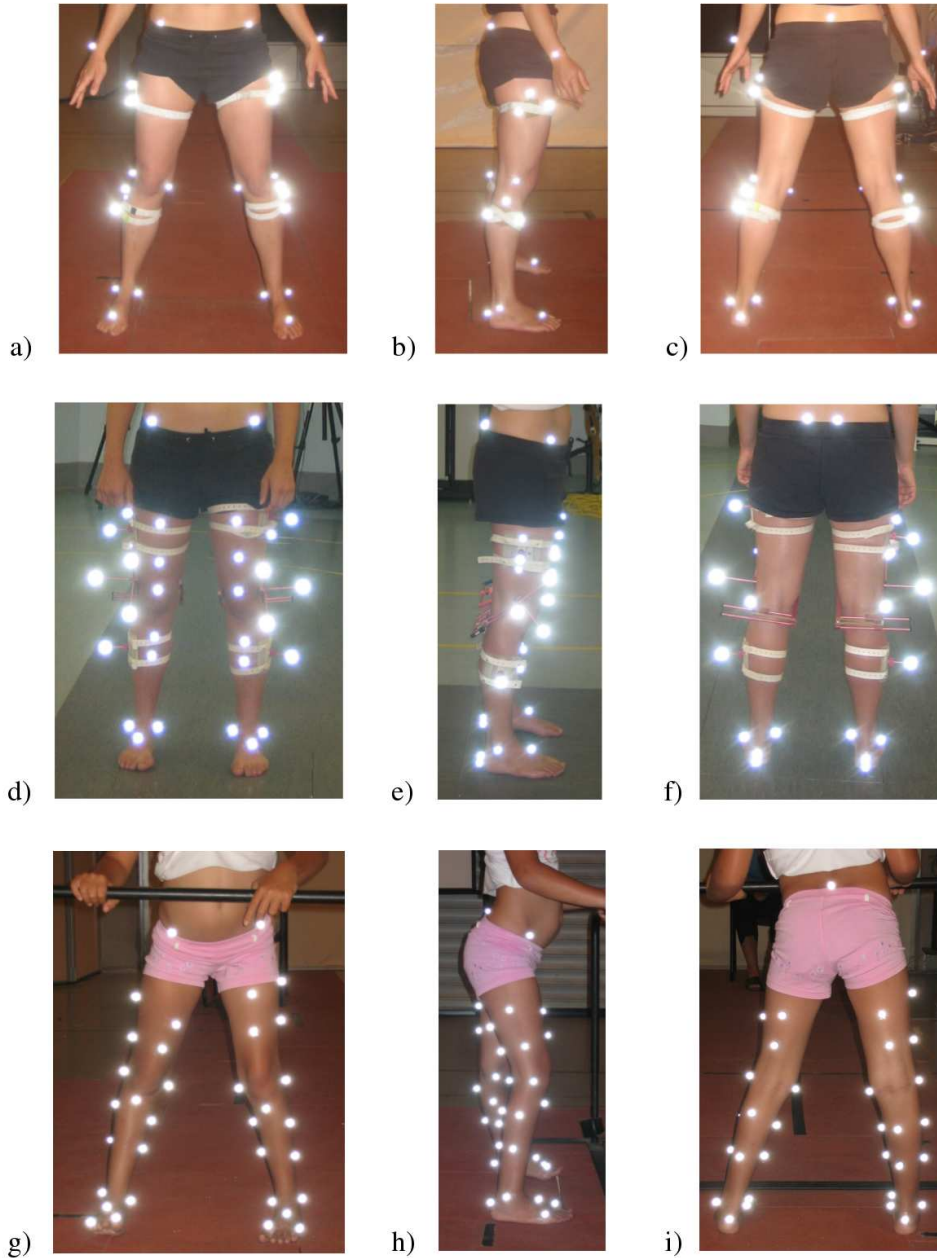


Figure 3.7: a) - c) The standard Cleveland Clinic marker set, d) - f) a redefined marker set developed and used at the Hugh Williamson Gait Laboratory, Victoria, Australia, g) - h) a customised marker set used at the Tamaki Gait Laboratory, University of Auckland, New Zealand, from frontal, lateral and posterior view.

hence, the marker positions from optical motion capture are given with respect to the spatial frame. The spatial coordinate system is generally a right-handed, orthogonal system with an arbitrary origin. It is common in gait analysis that the x-axis coincides with the walking direction and the z-axis is pointing upwards.

In contrast, any coordinate system which is fixed to a body is termed *material*, *local* or *Lagrangian* coordinate system. Material coordinate systems move with the body and the position of any segmental point with respect to a material frame remains unchanged during movement. In the case of a rigid body, an initial orthogonal material coordinate system remains orthogonal.

Two material coordinate systems need to be defined in the scope of 3D gait analysis in order to relate the marker positions to the underlying anatomical axes of the bones (Cappozzo et al., 2005): an anatomical coordinate system and a technical coordinate system. The anatomical coordinate system is defined with respect to the anatomical axes of each bone structure and generally standardised beyond the scope of gait analysis, while the technical coordinate system depends on the adopted marker configuration.

Anatomical Coordinate System

Anatomical coordinate systems are defined with respect to the anatomical axes of each bone structure according to the Standardisation and Terminology Committee of the International Society of Biomechanics (ISB) (Wu, 2002). The anatomical axes of bones are derived from the locations of so-called *anatomical landmarks*. A detailed description and illustration of all anatomical landmarks in the lower limbs are provided in Cappozzo et al. (2005). The anatomical landmarks which were used in the scope of the present work for defining the anatomical coordinate systems of bone structures in the lower limbs are given in Table 3.1. The corresponding anatomical coordinate systems are illustrated in Figure 3.8.

Most of the anatomical landmarks given in Table 3.1 are defined on bony prominences which are palpable through the skin. However, some anatomical landmarks, in particular joint centres, can not be externally assessed. Different methods have been proposed to derive the positions of internal anatomical landmarks from the external information (Bell et al., 1989; Besier et al., 2003; Lu & O'Connor, 1999; Schache et al., 2006). The methods can roughly be divided into two groups that are predictive and functional methods.

Predictive methods relate the positions of externally palpable landmarks to internal landmarks based on anatomical measurements in a normal population. In clinical gait analysis, the hip joint centre has commonly been derived using the predictive equations described in Bell et al. (1989) who measured the size of 41 adult pelvi from frontal and lateral radiographs, and established an empirical relationship between the externally palpable landmarks of the pelvis and the hip joint centre. The average position of the hip joint centre amongst the 41 subjects given in % of pelvis width was found to be 14 % medial, 22 % posterior and 30 % distal of the anterior superior iliac spine.

However, concerns have been expressed in terms of the accuracy of predictive equations for the hip joint centre, especially when applied to children, and functional methods have been introduced into clinical gait analysis (Harrington et al., 2007; Stagni et al., 2000). Functional methods require participants to move the lower limbs through a range of movements, and the hip joint centers are then derived by fitting spheres to the data clouds (Besier et al., 2003; Schache et al., 2006).

Given subject-specific lower limb models based on MRI, the position of internal anatomical landmarks can accurately be derived and related to external landmarks without the need of predictive or functional methods (Harrington et al., 2007). Instead, the hip joint centre is determined by fitting a sphere to the femoral head of the subject-specific model, Fig. 3.8b. A review of methods and techniques for deriving the hip joint centre is provided in Ehrig et al. (2006).

Technical Coordinate System

The technical coordinate system refers to the material coordinate system which is arbitrarily defined from the positions of at least three retro-reflective markers. The determination of its axes during gait is always an estimate due to the non-rigid movement of skin markers. If markers are positioned on externally palpable anatomical landmarks, the axes of the marker-based technical coordinate system approximately coincide with the anatomical axes of the bones. However, anatomical landmarks are not always the ideal choice for marker placements due to a limited visibility during gait or due to increased movement of the skin with respect to the underlying bones at these particular points (Cappozzo et al., 1995). Hence, markers are sometimes positioned arbitrarily with a non-repeatable geometric relationship to the relevant bone, see for example the triads on the rigid

3.2. DERIVATION OF SEGMENTAL AND JOINT KINEMATICS

Table 3.1: Anatomical landmarks for defining the anatomical coordinate systems of the pelvis, femur, patella, tibia, fibula and foot (Cappozzo et al., 2005).

<i>Pelvis</i>	
ASIS	anterior superior iliac spine
PSIS	posterior superior iliac spine
<i>Femur & patella</i>	
HJC	hip joint centre
ME	medial femoral epicondyle
LE	lateral femoral epicondyle
KJC	knee joint centre
<i>Tibia & fibula</i>	
KJC	knee joint centre
MM	distal apex of the medial malleolus
LM	distal apex of the lateral malleolus
AJC	ankle joint centre
<i>Foot</i>	
AJC	ankle joint centre
CA	upper ridge of the calcaneus posterior surface
SM	dorsal aspect of the second metatarsal head

CHAPTER 3. THEORETICAL BACKGROUND

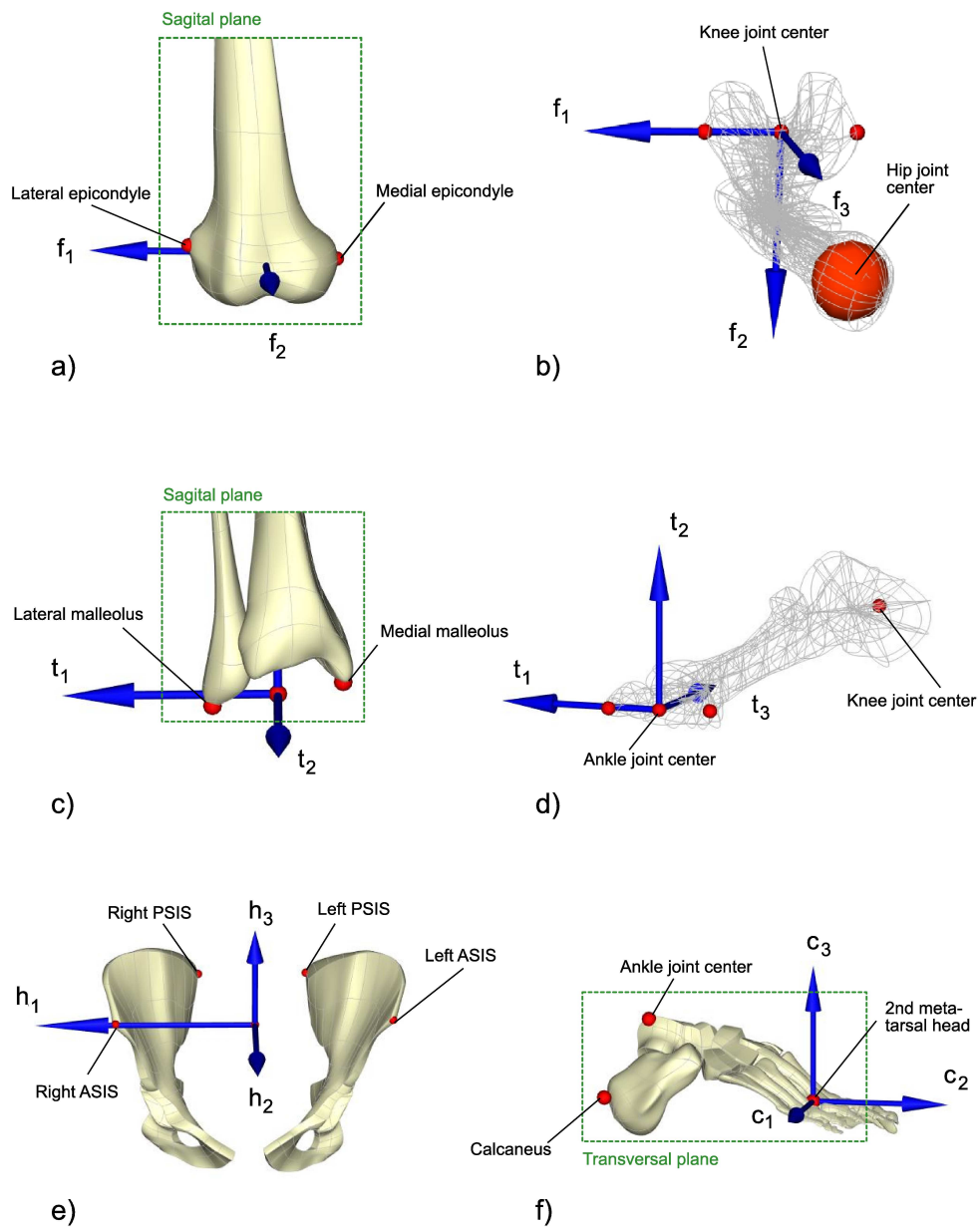


Figure 3.8: The anatomical coordinate system for a) and b) femur, c) and d) tibia/fibula, e) pelvis and f) foot.

plates of the Cleveland Clinic marker set in Figure 3.7a-c.

In the case of arbitrary marker positioning, the relationship between the technical and the anatomical coordinate system is established during a so-called static trial. Thereby, additional markers are temporarily positioned on relevant anatomical landmarks, and their local positions with respect to the technical coordinate system is derived. The spatial positions of the additional markers during walking are reconstructed via coordinate transformations between the technical and the spatial coordinate system under the assumption that the local positions remain constant during motion.

3.2.3 Segmental Kinematics

In 3D gait analysis, the human skeleton has commonly been modelled as kinematic chain consisting of rigid segments which are inter-connected by joints (Cappozzo et al., 2005; Nigg & Herzog, 1999). The objective of segmental kinematics is the mathematical description of the motion of the kinematic chain based on the skin marker coordinates. Kinematics is generally defined as the study of motion and deformation of an object without reference to the forces that cause the motion (Bonet & Wood, 1997).

Transformation matrices, which describe mappings of bone structures between consecutive time frames, are the basis for the description of segmental kinematics, Fig. 3.9. The transformation matrix \mathbf{T} with entries t_{ii} which transforms all particles \mathbf{p}_i of a body from state A to state B is given as

$$\begin{bmatrix} p_{1i} \\ p_{2i} \\ p_{3i} \\ 1 \end{bmatrix}_B = \begin{bmatrix} t_{11} & t_{12} & t_{13} & t_{14} \\ t_{21} & t_{22} & t_{23} & t_{24} \\ t_{31} & t_{32} & t_{33} & t_{34} \\ 0 & 0 & 0 & 1 \end{bmatrix} \begin{bmatrix} p_{1i} \\ p_{2i} \\ p_{3i} \\ 1 \end{bmatrix}_A . \quad (3.14)$$

In the case of a rigid body, which does not deform during motion, the transformation matrix \mathbf{T} , Eq. 3.14, comprises a rotation followed by a translation. Such a transformation is also called *Euclidean* transformation. An Euclidean transformation matrix can be expressed in terms of a rotation matrix \mathbf{R} with entries

r_{ii} and a translation vector \mathbf{t} with entries t_i in the following form

$$\mathbf{T} = \begin{bmatrix} r_{11} & r_{12} & r_{13} & t_1 \\ r_{21} & r_{22} & r_{23} & t_2 \\ r_{31} & r_{32} & r_{33} & t_3 \\ 0 & 0 & 0 & 1 \end{bmatrix} . \quad (3.15)$$

The Euclidean transformation matrix \mathbf{T} , Eq. 3.15, is generally non-singular and can be inverted. It can be derived in various ways given the positions of at least three points of the rigid body in state A and B.

The most common way in 3D gait analysis is to establish a relationship between the axes of the anatomical coordinate systems in the two positions. Assuming that the anatomical axes of the rigid body in state A and B are known as $[\mathbf{f}_1 \ \mathbf{f}_2 \ \mathbf{f}_3]$ and $[\mathbf{f}'_1 \ \mathbf{f}'_2 \ \mathbf{f}'_3]$ respectively, the rotation to align the two sets of axes with respect to each other is specified by an orthogonal rotation matrix \mathbf{R} derived from

$$\mathbf{R} = \begin{bmatrix} \mathbf{f}_1 \cdot \mathbf{f}'_1 & \mathbf{f}_2 \cdot \mathbf{f}'_1 & \mathbf{f}_3 \cdot \mathbf{f}'_1 \\ \mathbf{f}_1 \cdot \mathbf{f}'_2 & \mathbf{f}_2 \cdot \mathbf{f}'_2 & \mathbf{f}_3 \cdot \mathbf{f}'_2 \\ \mathbf{f}_1 \cdot \mathbf{f}'_3 & \mathbf{f}_2 \cdot \mathbf{f}'_3 & \mathbf{f}_3 \cdot \mathbf{f}'_3 \end{bmatrix} . \quad (3.16)$$

Proof of Equation 3.16 is provided in Bonet & Wood (1997), recalling that the dot product of two vectors equals the cosine of the angle between them. The translation vector \mathbf{t} , which translates the origin \mathbf{p} of the anatomical coordinate system $[\mathbf{f}_1 \ \mathbf{f}_2 \ \mathbf{f}_3]$ to coincide with the origin \mathbf{p}' of $[\mathbf{f}'_1 \ \mathbf{f}'_2 \ \mathbf{f}'_3]$, is given as

$$\mathbf{t} = \mathbf{p}' - \mathbf{R} \cdot \mathbf{p} . \quad (3.17)$$

A Euclidean transformation not only describes a mapping of a rigid body between two positions, but generally a coordinate transformation between two orthogonal coordinate systems. Hence, it can also be used to transform the local coordinates of anatomical landmarks into the spatial coordinate system or the anatomical axes of one rigid segment with respect to another.

3.2.4 Joint Kinematics

The Euclidean transformation matrix, Eq. 3.15, provides a description of the position of two rigid bodies with respect to each other, or generally, a description of the relationship between two orthogonal coordinate systems. However, it does

3.2. DERIVATION OF SEGMENTAL AND JOINT KINEMATICS

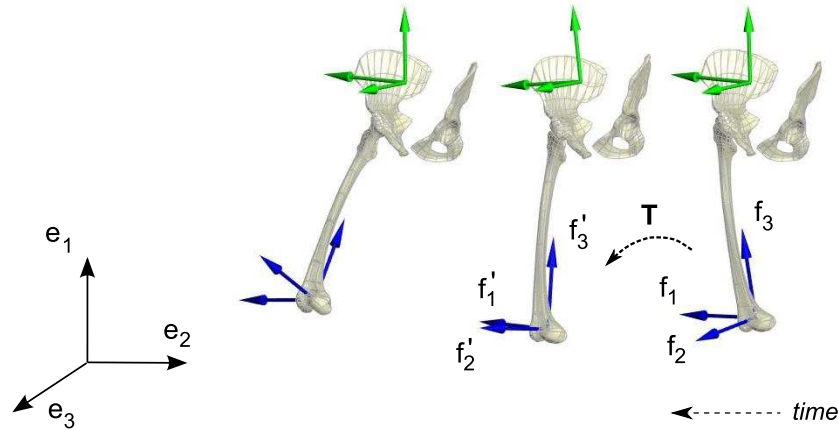


Figure 3.9: Segmental kinematics is described via Euclidean transformation matrices, \mathbf{T} , which are commonly derived from the axes of anatomical coordinate systems $[\mathbf{f}_1 \ \mathbf{f}_2 \ \mathbf{f}_3]$ in consecutive time frames.

not specify the path of motion which led to a given configuration. The objective of joint kinematics is the description of joint movement that is the motion of a distal segment relative to a proximal segment.

Joint motion is generally constrained due to the architecture of the joining bones and due to ligaments and muscle-tendon structures that cross the joint. The hip joint is considered the only true ball-and-socket joint in the body, allowing the femur to rotate within the acetabulum of the pelvis but not to translate (Whittle, 2002). The motion in the knee joint is controlled by five ligaments and is a combination of sliding and rolling of the femur on the tibia. The flexion axis is thereby not fixed but changes with the angle of flexion. The ankle joint has only one significant type of motion and that is dorsi and plantar flexion.

The translational DOF in the knee joint are generally too small to be accurately assessed by means of optical motion capture (Cappozzo et al., 2005). Hence, joint kinematics is mainly concerned with a clinical meaningful description of the rotational DOF, referring to the orientation of one rigid body with respect to another. Many paths may be followed by a rigid body moving from one position to another; thus different conventions have been proposed to describe it. In clinical gait analysis, the Euler/Cardan convention and the convention based on Grood & Suntay (1983) are most widely used (Robertson et al., 2004). The reader is referred to the literature for a description of other conventions such as

the helical or screw axis (Spoor & Veldpaus, 1980), the attitude vector (Woltring, 1994) or the quaternions (Altmann, 1986).

Euler/Cardan Convention

According to Euler's displacement theorem, a rigid body displacement can not only be described as a rotation followed by a translation, but the rotation can further be parametrised using three angles. The three angles represent three planar rotations around three axes³.

Different Euler/Cardan conventions emerge depending on the axes about which the rotations are carried out. The conventions which include a repetition of rotations about one particular axis, for example a 'z-x-z' order, are also referred to as Eulerian conventions. The corresponding angles are called Euler angles. In contrast, the Cardan type of successive rotations are generally characterised by rotations about all three axis. In 3D gait analysis, the Cardan sequence 'x-y-z' appears to be used the most (Robertson et al., 2004), Fig. 3.10. The corresponding rotation matrix \mathbf{R} is written as the matrix product of the three planar rotations ψ , θ and ϕ as given in Equation 3.18.

$$\mathbf{R} = \begin{bmatrix} \cos \psi & \sin \psi & 0 \\ -\sin \psi & \cos \psi & 0 \\ 0 & 0 & 1 \end{bmatrix} \begin{bmatrix} \cos \theta & 0 & -\sin \theta \\ 0 & 1 & 0 \\ \sin \theta & 0 & \cos \theta \end{bmatrix} \begin{bmatrix} 1 & 0 & 0 \\ 0 & \cos \phi & \sin \phi \\ 0 & -\sin \phi & \cos \phi \end{bmatrix} \quad (3.18)$$

Remembering that matrix multiplication is non-commutative, it becomes clear that a change of the sequence given the same angles will lead to a different joint configuration. One must be careful in interpreting the Cardan angles ψ , θ and ϕ in a clinical context as the second rotation around an intermediate axis is difficult to visualise, and employing different sequences for different segments complicates the analysis (Allard et al., 1995).

Grood and Suntay Convention

A sequence independent angle convention for the clinical description of joint kinematics was proposed by Grood & Suntay (1983). Thereby, a so-called joint

³Weisstein, Eric W. "Euler's Displacement Theorem.", MathWorld, Wolfram Web Resource (<http://mathworld.wolfram.com/EulersDisplacementTheorem.html>)

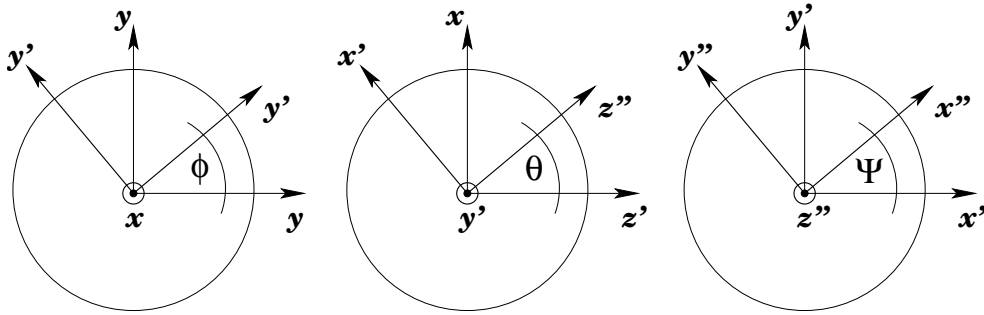


Figure 3.10: The Cardan sequence 'x-y-z' describes a rotation around the x-axis by an angle ϕ , followed by a rotation around the rotated y-axis denoted y' by an angle θ and a final rotation around the new z-axis denoted z'' by an angle ψ .

coordinate system is defined with respect to the anatomical axes of neighbouring segments. The joint coordinate system is composed of the medio-lateral axis of the proximal segment, the longitudinal axis of the distal segment, and an intermediate or *floating* axis which is defined normal to the latter two, Fig. 3.11. The joint coordinate system is generally not orthogonal except for special segmental positions.

Given the axes of the proximal and distal anatomical coordinate system as $[\mathbf{f}_1 \ \mathbf{f}_2 \ \mathbf{f}_3]$ and $[\mathbf{t}_1 \ \mathbf{t}_2 \ \mathbf{t}_3]$ respectively, the clinical rotations flexion-extension, abduction-adduction and internal-external rotation can be derived from the following angles

$$\alpha = \arcsin(-\mathbf{f}_1 \cdot \mathbf{f}_3) \quad , \quad \beta = \arcsin(\mathbf{f}_1 \cdot \mathbf{t}_3) \quad , \quad \gamma = \arcsin(\mathbf{t}_1 \cdot \mathbf{f}_1) \quad (3.19)$$

whereby \mathbf{f}_1 denotes the floating axis. Note that the clinical rotation angles are slightly different from α , β , and γ depending on the joint and the body side. The relationship between the angles α , β and γ and the rotation matrix \mathbf{R} , Eq. 3.16, is provided in Grood & Suntay (1983).

The Grood and Suntay convention facilitates the derivation of clinically relevant data and allows for a more standardised comparison of joint kinematics between subjects. The Committee on Standardisation of ISB has published a proposal on kinematics standardisation in which the Grood and Suntay convention is recommended (Wu, 2002).

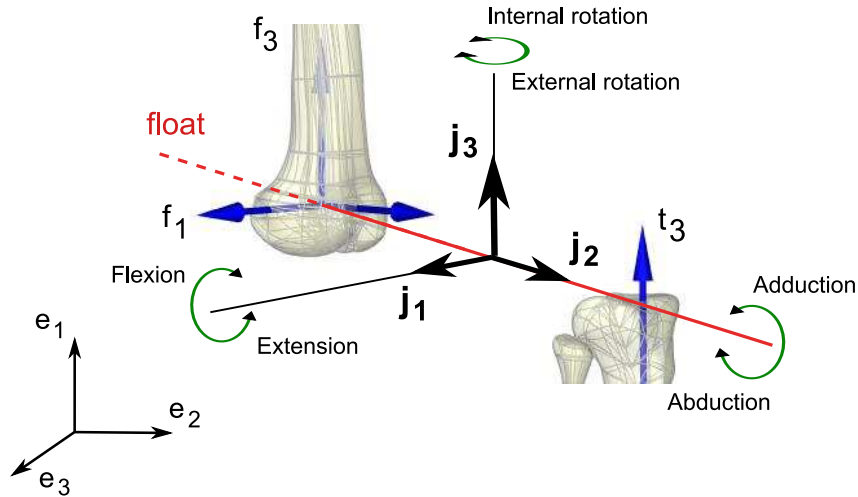


Figure 3.11: The joint coordinate system $[j_1 \ j_2 \ j_3]$ for the right knee according to Grood & Suntay (1983) with the floating axis defined as $j_2 = t_3 \times f_1$; and the remaining two axes as $j_1 = f_1$ and $j_3 = t_3$ respectively.

3.2.5 Error Sources and Optimisation Algorithms

Unfortunately, different error sources bias the results from 3D gait analysis. A series of four papers has recently provided a broad review of the problems associated with reconstructing and analysing segmental and joint kinematics from optical motion capture data (Cappozzo et al., 2005; Chiari et al., 2005; Della Croce et al., 2005; Leardini et al., 2005). The three main error sources, discussed within the series, are instrumental errors, anatomical landmark displacement and Soft Tissue Artefact(s) (STA).

Instrumental errors represent the uncertainty of the skin marker reconstruction within the laboratory frame using a particular motion capture system; anatomical landmark displacements emerge if skin markers are not accurately placed onto externally palpable anatomical landmarks, and STA refer to the motion of the skin with respect to the underlying bones. While instrumental errors and anatomical landmark displacements are error sources which can be reduced by proper calibration of the system (Chiari et al., 2005) and careful experimental design (Stagni et al., 2006), the reduction of STA is more challenging.

3.2. DERIVATION OF SEGMENTAL AND JOINT KINEMATICS

Studies quantifying STA through use of intracortical pins (Benoit et al., 2006; Fuller et al., 1997; Reinschmidt et al., 1997), external fixators (Cappozzo et al., 1996) or fluoroscopy-based tracking (Stagni et al., 2005) have reported STA ranging from a few millimetres for shank markers through to 40 mm for femoral epicondyle markers in the anterior-posterior direction during 120 degree knee flexion. Generally, the artefacts were found to be greater on thigh than on shank, whereby the magnitude of STA depend on the subject, the location of the skin markers and the motion being performed (Cappozzo et al., 1996; Fuller et al., 1997; Stagni et al., 2005).

Several optimisation algorithms have been developed, aiming to compensate for STA (Andriacchi et al., 1998; Arun et al., 1987; Challis, 1995; Soederkvist & Wedin, 1993). Some of them were recently compared and their stabilities were analysed in case of highly ill-conditioned marker configurations (Carman & Milburn, 2006; Cereatti et al., 2006). Cereatti et al. (2006) showed that the stability of an optimisation algorithm proposed by Challis (1995), which is based on singular value decomposition, was significantly better when compared with other techniques such as the point cluster method (Andriacchi et al., 1998). The optimisation algorithm based on singular value decomposition is outlined in the Appendix C.

3.2.6 Summary

- Optical motion capture systems, such as the Vicon MX motion analysis system, allow for capturing and simultaneously reconstructing the positions of skin markers during walking. The Cleveland Clinic marker set has been most often used in clinical gait analysis, while customised marker sets with a redundant number of markers have been deployed for research purposes. The Vicon software enables the trajectories of skin markers to be exported for further analysis.
- An anatomical coordinate system can be defined for each segment based on three anatomical landmarks according to the Standardisation and Terminology Committee of ISB. In contrast, a technical coordinate system is arbitrarily defined for each segment from at least three non-collinear markers. The positions of externally-palpable anatomical landmarks are recorded with respect to the technical frame during a static trial, allowing

their spatial position to be reconstructed during walking. The positions of anatomical landmarks, which are not palpable through the skin such as the joint centres, are commonly derived using predictive equations based on anthropometric measurements.

- The objective of segmental kinematics is the derivation of rigid bone motion based on the skin marker positions from optical motion capture. Segmental kinematics is described by Euclidean transformation matrices which comprise a rotation followed by a translation. Euclidean transformation matrices can be thought of as mappings of body particles between two orthogonal coordinate systems, and can also be used to reconstruct the spatial coordinates of anatomical landmarks during gait.
- Joint kinematics is mainly concerned with the description of the rotational DOF of joint motion because the translational components are generally too small to be measured by means of optical motion capture. The angle convention proposed by Grood & Suntay (1983) allows for a sequence-independent description of the orientation of one segment with respect to another in terms of the clinically meaningful angles flexion-extension, abduction and internal-external rotation.
- The three main error sources in optical motion capture are instrumental errors, anatomical landmark displacements and STA. The reduction of STA, which refer to the non-rigid movements of skin markers with respect to the underlying bones, is difficult. Optimisation algorithms have been developed to minimise STA given a redundant number of markers. An optimisation algorithm based on singular value decomposition proposed by Challis (1995) was shown to result in a better approximation of segmental kinematics when compared with other techniques.

3.3 Finite Deformation of Anatomically-Based FE Models

The following section details techniques for deforming anatomically-based FE models of skeletal muscles based on segmental kinematics from optical motion capture by (i) introducing the term inverse kinematics, (ii) outlining geometric-based and (iii) mechanics-based deformation techniques, and (iv) discussing the issues of volume conservation and collision detection.

3.3.1 Inverse Kinematics

In real life, muscle contractions drive bone motion. Hence, it would be desirable to derive segmental kinematics from the generated muscle forces, an approach termed *forward dynamics*. Forward dynamic methods depend on the prior estimation of how much force is generated by a single muscle at each instant in time during a particular motor task. This prediction is difficult to make because it requires the knowledge of either the neural excitation patterns or the generated muscle forces themselves (Zajac, 1993).

The accurate assessment of excitation patterns or muscle forces is challenging given current measurement techniques, in particular for complex motion patterns such as gait. Instead of solving a forward dynamics formulation, the deformation of muscles is commonly derived from the bone position. Thereby, the term *inverse kinematics* refers to the prior derivation of segmental and joint kinematics from optical motion capture data described in Section 3.2. The term *inverse dynamics* refers to the further derivation of muscle forces given the ground reaction forces and an appropriate description of the material properties of muscle tissue. The basic concepts behind inverse kinematics, inverse dynamics and forward dynamics are schematically outlined in Figure 3.12.

The present work is primarily concerned with the prediction of muscle soft-tissue deformation based on inverse kinematics. From inverse kinematics, certain points of the muscles are given throughout gait. These points generally comprise the attachment points as well as further points along the muscle paths which have a given kinematic relationship to the bones. Examples of such additional points are the via-points illustrated in Figure 2.1. A modelling technique is then required which allows the deformation of the muscles based on the limited number of known material points.

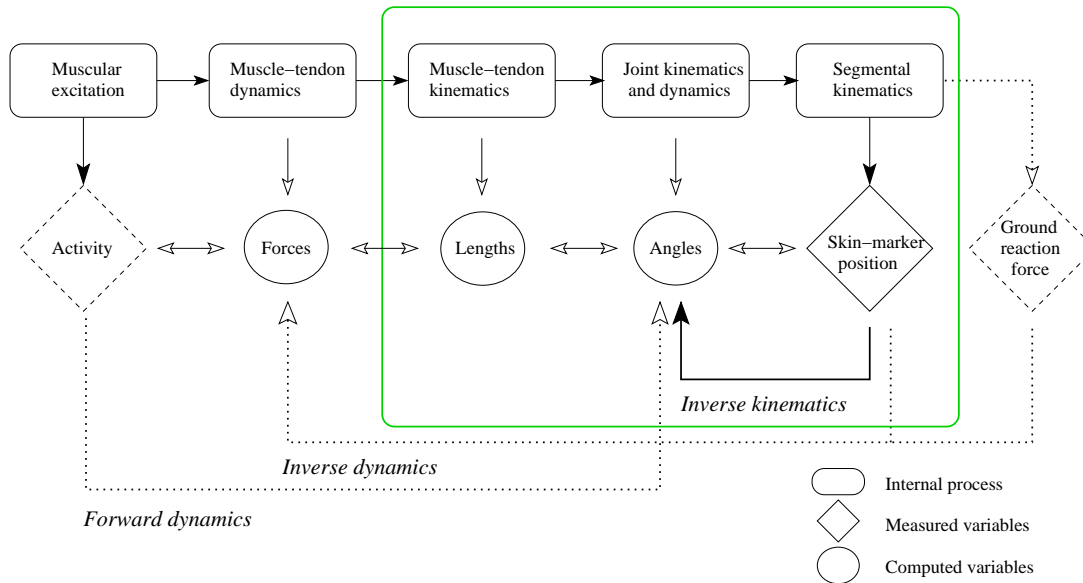


Figure 3.12: Muscle-tendon lengths is commonly derived from inverse kinematics which refers to the calculation of joint angles based on the measured skin marker position (green box). Inverse dynamics refers to the derivation of muscle forces based on kinematic and kinetic data from 3D gait analysis, while forward dynamics refers to the calculation of joint angles based on the measured muscle activation from electromyography.

Three techniques are outlined in the following for deriving soft-tissue muscle deformations for anatomically-based FE models from inverse kinematics. Two techniques are so-called *geometric-based* methods, which are purely based on the kinematics of the given material points without paying attention to the forces that have caused the deformation. The third technique is the so-called *mechanics-based* approach, which refers to the derivation of muscle deformation by solving the governing equations of finite elasticity on the muscle continuum using the known points as boundary condition. A comparison between the three approaches is given in Table 3.3 at the end of this section.

3.3.2 Geometric-Based Deformation Techniques

For geometric-based deformation techniques, a FE muscle model is regarded as a geometric object without intrinsic material properties. Such a geometric object can be deformed randomly in any direction, without taking into account the relationship between forces acting on the body and the resulting motion.

Geometric-based deformation techniques are purely based on the theory of kinematics, which is the study of motion and deformation without reference to the cause (Bonet & Wood, 1997).

A mapping of material points between two states can be described by a transformation matrix as outlined in Section 3.2, Eq. 3.14. In the case of a non-rigid deformation, the transformation matrix comprises rotation, translation, scaling and shearing. Such a transformation is also called *affine* transformation. The twelve entries of the affine transformation matrix can be uniquely derived if four points of the body are given in the undeformed and the deformed state. However, the resulting transformation matrix does not ensure the accurate mapping of all body particles between the two states. In fact, four different body points would probably lead to a different result.

The challenge of finding an optimal transformation matrix for each body particle based on a limited number of known points can be approached in different ways. Two techniques are outlined in the following namely the direct least-squares method and the HMF technique. Further geometric-based modelling techniques have been developed in computer graphics research for deforming 3D muscle structures based on segmental kinematics (Dong et al., 2002; Scheepers et al., 1997). However, these techniques are generally not useful for deforming anatomically-based FE models and are not further discussed in the present work.

The Direct Least-Squares Method

The aim of the direct least-squares method is the calculation of an optimal transformation matrix \mathbf{T} for the entire body given four or more material points in the deformed and undeformed state, Fig. 3.13. The direct least-squares formulation is set up to minimise the objective function \mathcal{D}

$$\mathcal{D} = \sum_{d=1}^D [(\mathbf{p}_d^{\text{def}} - \mathbf{T} \cdot \mathbf{p}_d^{\text{un}})^T (\mathbf{p}_d^{\text{def}} - \mathbf{T} \cdot \mathbf{p}_d^{\text{un}})] \quad , \quad (3.20)$$

with \mathbf{p}_d^{un} and $\mathbf{p}_d^{\text{def}}$ ($d \geq 4$) being the material points in the undeformed and deformed state (Mithraratne & Hunter, 2006). The direct least-squares solution is obtained by differentiating the objective function, Eq. 3.20, with respect to each unknown entry of \mathbf{T} and setting the expression to zero.

The nodal positions of the FE mesh in deformed state are found by applying the resulting transformation matrix to all nodal coordinates in the undeformed state, Eq. 3.14. If higher order interpolation functions are used to represent the geometry, not only the nodal values but also the nodal derivatives need to be transformed. This is done by differentiating Equation 3.14 with respect to each host mesh local coordinate, and applying the resulting expression to the nodal derivatives in undeformed state.

Using the direct least-squares approach, the same affine transformation matrix is applied to all body particles. As such, the method is not capable to capture local deformations along a single muscle structure. For instance, the direct-least squares method could not capture an isolated deformation of the long head of biceps femoris due to a movement of the pelvis with the short head remaining undeformed.

Host-Mesh Fitting (HMF)

The HMF technique has previously been described in Section 3.1 as a method for customising a generic FE mesh to a limited number of subject-specific data from MRI. The geometric free-form technique can be used to derive soft-tissue muscle deformation during walking by embedding the complex anatomically-based FE muscle model into a simple host mesh, and deforming the host mesh based on the limited number of points on the muscle structures that are given from segmental kinematics (Fernandez et al., 2005). The material points in consecutive time frames are thereby used as landmark and target points for deforming the host mesh, Fig. 3.13.

Unlike the direct least-squares method, the HMF objective function, Eq. 3.11, is not solved for the unknown entries of one transformation matrix but for the host mesh nodal values themselves. As a result, each node of the host mesh undergoes a different transformation which is then passed onto the slave mesh. Hence, local deformations of muscle structures can be captured using the HMF technique if the host mesh is designed wisely.

The host mesh nodal DOF determine the number of material points that are required for obtaining a reasonable solution. For example, a trilinear one element host mesh has 24 DOF, requiring only 8 data points to result in a determined system. In contrast, a bicubic-linear one element host mesh has already 96 DOF,

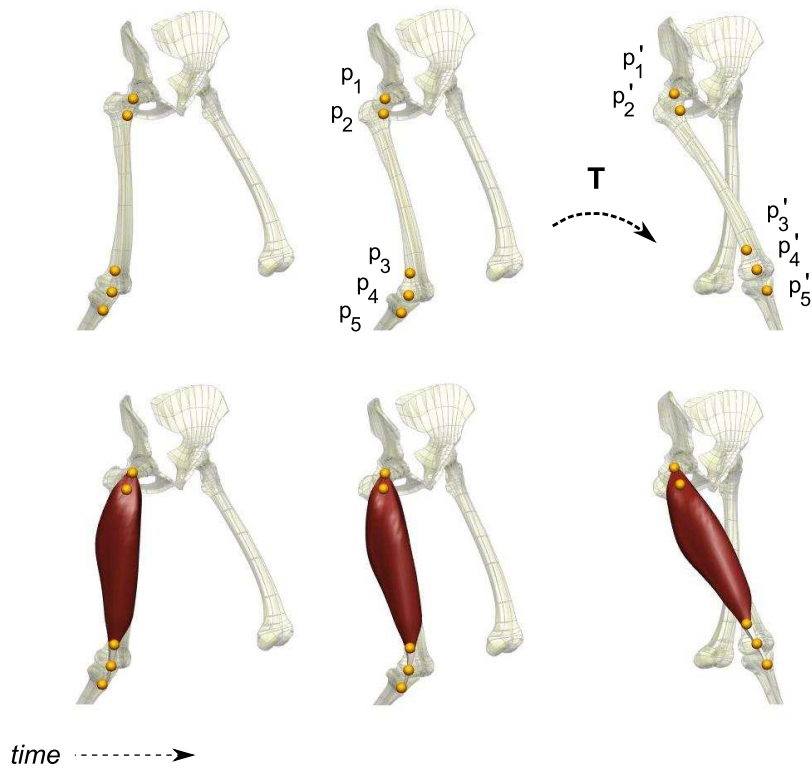


Figure 3.13: Three different approaches are feasible for deriving soft-tissue muscle deformation from inverse kinematics: (i) The geometric-based Direct Least-Squares method aims to find the optimal transformation matrix \mathbf{T} based on the known material points \mathbf{p}_i , (ii) the geometric-based HMF method uses the known material points \mathbf{p}_i and \mathbf{p}'_i as landmark and target points for deforming a simple host mesh; and (iii) the mechanics-based formulation aims to find the displacement fields of all material particles given the displacements $\mathbf{u}_i = \mathbf{p}'_i - \mathbf{p}_i$ of only a few points as boundary condition.

requiring 32 data points to lead in a determined system. Depending on the number, as well as the distribution of the landmark and target points, additional constraints need to be imposed to avoid any undesirable distortion of the host mesh. Constraints have been implemented into the HMF formulation within CMISS in the form of the Sobolev penalty function, Eq. 3.11.

3.3.3 Mechanics-Based Deformation Techniques

In the case of mechanics-based deformations, a FE mesh is regarded as a continuum body, which is an assembly of particles with specific material properties. A continuum body deforms as a response to stress, whereby the degree of the deformation depends on the mechanical behaviour of the respective soft tissue. Mechanics-based deformation techniques draw on the theory of continuum mechanics, which is the study of motion and deformation of a material that is subjected to internal and external forces.

Muscle structures undergo large deformations during walking, resulting in non-linear relationships between the stresses and the strains. The theory of continuum mechanics in finite elasticity comprises three basic topics that are kinematics, balance principles and constitutive theory. A brief introduction into each topic is given in the following. The reader is referred to Bonet & Wood (1997) for more details on the theory of non-linear continuum mechanics and to Fernandez (2004) for more details on the mathematical implementation within CMISS.

Kinematics of the Continuum

Large deformations in continuum mechanics are generally described via transformations between the spatial and the material coordinate system. The most fundamental kinematic quantity in finite elasticity is then derived as the gradient of the transformation matrix with respect to the material coordinate system, also known as the deformation gradient tensor. The deformation gradient tensor \mathbf{F} transforms a line element from a material description $d\mathbf{X}$ to a spatial description $d\mathbf{x}$ as

$$d\mathbf{x} = \mathbf{F} \cdot d\mathbf{X} \quad , \quad \text{with} \quad (3.21)$$

$$\mathbf{F} = \begin{bmatrix} \frac{\partial x_1}{\partial X_1} & \frac{\partial x_1}{\partial X_2} & \frac{\partial x_1}{\partial X_3} \\ \frac{\partial x_2}{\partial X_1} & \frac{\partial x_2}{\partial X_2} & \frac{\partial x_2}{\partial X_3} \\ \frac{\partial x_3}{\partial X_1} & \frac{\partial x_3}{\partial X_2} & \frac{\partial x_3}{\partial X_3} \end{bmatrix} .$$

The deformation gradient tensor can be decomposed into an orthogonal rotation tensor \mathbf{R} and a right \mathbf{U} or left \mathbf{v} symmetric stretch tensor as $\mathbf{F} = \mathbf{R}\mathbf{U} = \mathbf{v}\mathbf{R}$. Stretch tensors are independent of any rigid body motion and only comprise scaling and shearing.

Strains are introduced into the theory of finite elasticity based on a concept to facilitate the analysis of the continuum under deformation. Strain quantities relate to the change in lengths of line elements due to deformation. Strain tensors are generally defined in terms of the stretch components of the deformation gradient tensor. The right and left Cauchy-Green strain tensors, \mathbf{C} and \mathbf{b} , are given as

$$\begin{aligned} \mathbf{C} &= \mathbf{F}^T \mathbf{F} = \mathbf{U}\mathbf{U} = \mathbf{C}^T \quad , \\ \mathbf{b} &= \mathbf{F}\mathbf{F}^T = \mathbf{v}\mathbf{v} = \mathbf{b}^T \quad , \end{aligned} \tag{3.22}$$

whereby both strain tensors are symmetric and can be decomposed into principle stretches and principle directions according to the spectral theorem.

The deformation gradient tensor and, hence, the strain tensors can be expressed as functions of displacement fields, which are measurable kinematic quantities. Displacement vectors relate the positions of particles in the undeformed state to their positions in deformed state. So-called boundary value problems in finite elasticity aim to find the displacement fields of all material particles given the displacements of only a few material particles as boundary condition, Fig. 3.13.

Balance Principles

The governing equations of continuum mechanics are derived from four conservation principles that are the principles of conservation of mass, conservation of linear momentum, conservation of angular momentum and conservation of energy. The basis for the conservation of linear and angular momentum are the Newton's laws of motion which describe the relationship between forces acting on a body and the motion or deformation of the body.

Newton's laws of motion can be written as functions of the Cauchy stress tensor, leading in Cauchy's first and second equation of motion. Stress, which is based on a concept introduced by Cauchy into the theory of elasticity, relates the force acting on an infinitesimal small area of the continuum body to the outward normal of the same area.

For the static equilibrium, Cauchy's first equation of motion is given as

$$\int_v (\operatorname{div}(\sigma) + \mathbf{b}) \, dv = 0 \quad , \quad (3.23)$$

whereby $\operatorname{div}(\sigma)$ denotes the divergence of the Cauchy stress tensor σ and \mathbf{b} are the body forces per unit volume. It can be shown from Cauchy's second equation of motion that the Cauchy stress tensor σ is symmetric, allowing a spectral decomposition into principle stresses and principle directions (Bonet & Wood, 1997).

The so-called virtual work equation is obtained from the weak form of the governing equation, Eq. 3.23, as

$$\delta\omega = \int_v (\operatorname{div}(\sigma) + \mathbf{b}) \cdot \delta\mathbf{u} \, dv = 0 \quad . \quad (3.24)$$

Equation 3.24 is a fundamental scalar equation in finite elasticity and states that a continuum is only in equilibrium if the virtual work $\delta\omega$ of all forces acting on the body is zero in a virtual displacement $\delta\mathbf{u}$.

Constitutive Theory

The relationships between the stresses and the deformation are known as constitutive equations. Constitutive equations describe the behaviour or intrinsic physical properties of the continuum. Biological tissues are generally considered to be hyperelastic. A material is termed *elastic* if the work done by the stresses only depends on the initial state and the current state of the continuum but not the path inbetween. A material is termed *hyperelastic* if a stored strain-energy density function or elastic potential can additionally be established. The strain-energy density function Ψ describes the work done by the stresses from the initial to the current configuration on an unit volume, and hence establishes a relationship between the stresses and the strain.

3.3. FINITE DEFORMATION OF ANATOMICALLY-BASED MODELS

Table 3.2: Mooney-Rivlin material parameters for muscle tissue adopted in previous studies

Constant	Value	Constant	Value
c_1	0.01 MPa [†]	c_2	0.01 MPa [†]
c_1 muscle	0.03 MPa [‡]	c_2	0.01 MPa [‡]
c_1 tendon	0.06 MPa [‡]	c_2	0.01 MPa [‡]

[†] Anatomically-based FE model of skeletal muscles (Meier & Blickhan, 2000; Roehrlé & Pullan, 2007)

[‡] Upper limb muscle model for application in computer graphics and simulation (Teran et al., 2005)

Skeletal muscle tissue has most commonly been modelled as an isotropic, incompressible Mooney-Rivlin material with sometimes additional terms for active forces in fibre directions (Meier & Blickhan, 2000; Roehrlé & Pullan, 2007; Teran et al., 2005). The response of isotropic materials to deformation is the same in all directions, which simplifies the analysis to the principle stretches and principle strains. The strain-energy density function Ψ of an isotropic Mooney-Rivlin material is given as

$$\Psi = c_1(I_1 - 3) + c_2(I_2 - 3) \quad , \quad (3.25)$$

where $c_{1,2}$ are the Mooney-Rivlin parameters and $I_{1,2}$ are the first and second invariant of the right Cauchy-Green strain tensor \mathbf{C} .

The derivation of accurate constitutive parameters from experimental data is crucial for obtaining accurate physiological results for mechanics-based formulations. A list of the Mooney-Rivlin constants, previously adopted for skeletal muscle tissue and passive deformation, is given in Table 3.2.

Solution Procedure

Numerical methods are required to solve boundary-value problems in finite elasticity and the FE method provides the most convenient framework (Nash & Hunter, 2000). The FE local coordinates, described in Section 3.1, are normalised element coordinates which deform with the body, and they generally provide the basis for the discretisation.

Two solution procedures are feasible to solve the boundary-value problem for the displacements fields of the continuum using the FE method. One can either discretise the equilibrium equation, Eq. 3.23, using the Galerkin FE method; or one can discretise the virtual work equation, Eq. 3.24, by approximating the

virtual displacement using a FE displacement field. Both approaches result in the same set of non-linear equations which can be solved using the Newton-Raphson iterative scheme.

The Newton-Raphson method depends on an initial guess of the final displacement field which is typically chosen to be the undeformed geometry and the prescribed displacement. The likelihood of convergence is increased if the initial guess is already close to the final solution. In case of large deformations between two time steps, commonly presenting during walking, the Newton-Raphson iterative process is likely to divert to a point that cannot be recovered from.

3.3.4 Volume Conservation and Collision Detection

Muscle structures are generally considered to be incompressible bodies which maintain their volume during deformation (Blemker & Delp, 2006; Roehrlé & Pullan, 2007; Teran et al., 2005). Volume constraints are commonly implemented into mechanics-based and geometric-based approaches based on the requirement that the Jacobian of an incompressible body has to be one. The Jacobian is defined as the determinant of the deformation gradient tensor \mathbf{F} , Eq. 3.21, and is a measure of volume change (Bonet & Wood, 1997).

Constitutive laws for incompressible hyperelastic materials in finite elasticity have been implemented into CMISS via the Lagrange multiplier method (Fernandez et al., 2005; Roehrlé & Pullan, 2007). Thereby, an additional term is added to the strain-energy function, Eq. 3.25, leading to

$$\Psi = c_1(I_1 - 3) + c_2(I_2 - 3) - \kappa(J - 1) \quad , \quad (3.26)$$

where the scalar κ serves as a Lagrangian multiplier that can, under certain circumstances, be associated with the hydrostatic pressure. κ is introduced as an additional DOF that needs to be solved for.

A volume constraint has also been implemented into the HMF formulation within CMISS which applies to the host mesh deformation (Fernandez et al., 2005). Thereby, the Jacobian at selected Gauss points of the host mesh is constrained by penalising any deviation from the initial volume. This is done by modifying the initial system of linear equations, Eq. 3.13, as

$$[A_{mn} + K(F_v)]\mathbf{u}_n = [B_m - R(F_v)] \quad . \quad (3.27)$$

3.3. FINITE DEFORMATION OF ANATOMICALLY-BASED MODELS

The additions to the stiffness matrix and the residual, K and R , are both dependent on a forcing function F_v

$$F_v(\xi_1, \xi_2, \xi_3) = k_j(J_c - J_i) \quad , \quad (3.28)$$

which weights any deviation from the initial volume, with $k_j \in [0, 1]$ being the penalty stiffness, and J_c and J_i the initial and current Jacobian values respectively. However, the volume constraint of the host mesh does not ensure volume conservation of the enclosed slave mesh, in particular if the host mesh is not in close alignment with the embedded muscle structure. Hence, muscle incompressibility can only be approximated using the HMF technique.

Apart from volume constraints, collision detection is an important aspect of any modelling technique which aims to accurately capture the muscle deformations during walking. Muscle-muscle collisions occur in areas where neighboring muscles are in contact and moving in opposite directions. They can be detected by checking the intersections of one muscle model against the surface area of the neighboring model.

Collision detection algorithms are generally mathematically complex and lead to a significant increase in computation time (Fernandez, 2004). Improved search techniques have been developed for speeding up the initial detection of overlapping regions between muscles (Dong et al., 2002). However, the adjustment of the models in response to collision remains complex because the volume has to be conserved for every small mesh deformation, leading to potential new collisions in different regions of the mesh. The process of collision detection, mesh adjustment and volume conservation needs to be repeated in each time frame until there is no detectable interaction between muscle models.

Using the geometric-based HMF technique, muscle-muscle collision can be avoided by embedding several muscles meshes into the same host mesh. As an analogy for any free-form deformation technique, Sederberg & Parry (1986) talks about the deformation of clear, flexible plastic in which several objects are embedded and deform along with the plastic that surrounds them. Hence, the HMF technique enables the deformation of neighbouring muscle structures without the need for complex contact constraints because the positions of muscles with respect to each other are maintained as long as their deformation is derived from the same host mesh, Fig. 3.14.

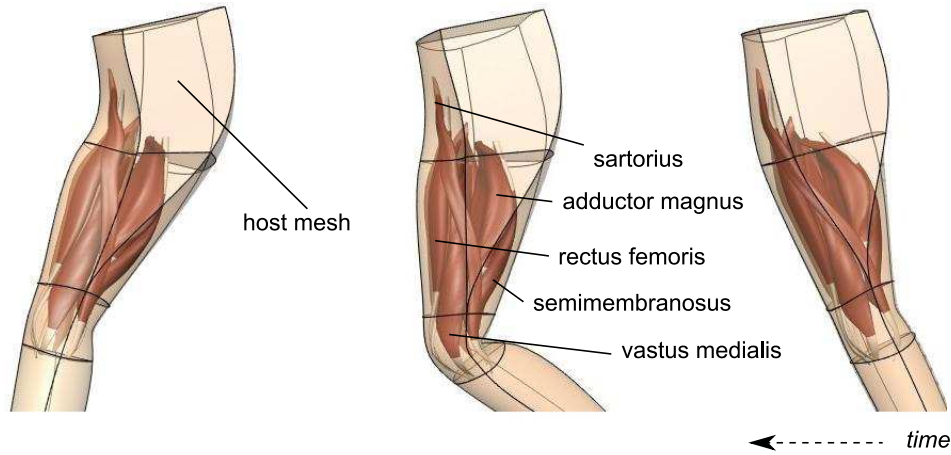


Figure 3.14: The HMF technique enables several muscle structures to be embedded into the same host mesh, thereby ensuring that their positions with respect to each other are maintained during deformation.

Table 3.3: Comparison between geometric-based deformation techniques, that are the direct least-squares method and the HMF technique, and mechanics-based techniques which are based on the theory of continuum mechanics in finite elasticity.

	least-squares	HMF	finite elasticity
Segmental constraints	boundary	boundary	boundary
Physical laws	-	-	force balance
Constitutive laws	-	-	hyperelastic
Volume conservation	-	host	muscle
Collision detection	non-linear	avoided	non-linear
Solved for	overall mesh \mathbf{T} , Eq. 3.20	DOF (host) \mathbf{u} , Eq. 3.11	DOF (muscle) $\sigma(\mathbf{u})$, Eq. 3.23
System of equations	linear	linear	non-linear

3.3.5 Summary

- Muscle soft-tissue deformations during walking are generally derived based on inverse kinematics. Given the segmental and joint kinematics from optical motion capture, certain points of the muscles, such as the attachment points, are known and are used as boundary condition to derive the muscle deformation. The modelling techniques for deforming FE muscle models based on the kinematic constraints can be put into two categories that are geometric-based or mechanics-based techniques.
- Geometric-based deformation methods, such as the least-squares method or the HMF technique, are not based on the physics laws of motion but the deformation is purely derived based on the kinematic constraints. The number and distribution of the known points predetermine the success of the direct least-squares method and the HMF technique. The direct least-squares method aims to find one optimal transformation matrix which is then applied to the entire body. In contrast, the HMF technique is capable of capturing spatial variations in the muscle deformation, depending on the host mesh design and the distribution of the known material points.
- Mechanics-based deformation techniques comply with the theory of continuum mechanics for finite elasticity. The governing equation of finite elasticity is derived from the conservation of linear momentum. The relationship between the forces and the deformation depends on the material properties and is described in the constitutive equations. Muscle tissue has often been modelled as incompressible, isotropic Mooney-Rivlin material. The experimental assessment of Mooney-Rivlin parameters for muscle tissue is crucial for obtaining valid solutions of mechanics-based formulations.
- Non-linearity in mechanics-based formulations derive from the non-linear material properties or from the complex geometry of the deforming body. The Newton-Raphson iterative scheme can be used to solve the non-linear system of equations. However, convergence of the Newton-Raphson iterative process may not be reached in the case of large displacements of the material between consecutive time steps. The computational complexity has restricted the application of mechanics-based techniques to only a few muscles for simple motor tasks (Blemker & Delp, 2005; Roehrl & Pullan, 2007; Teran et al., 2005).

- Volume conservation and collision detection are two important aspects of deformation techniques for musculoskeletal models that need to be addressed. The constitutive equations for finite elasticity and the HMF objective function have been extended within CMISS to account for incompressibility of muscle tissue (Fernandez, 2004). Muscle-muscle collision detection is generally mathematically complex, and significantly increases the computation time for deforming extensive musculoskeletal models such as the lower limbs during walking. The HMF technique enables the deformation of several muscles without the need for complex contact mechanics formulations by embedding several muscle structures into the same host mesh.

4

Study I: Muscle Volumes and Lengths in Children With Cerebral Palsy

The following chapter outlines the first study, which was conducted in order to develop a library of anatomically-based, subject-specific lower limb models of children with and without CP and investigate the differences in muscle volumes and muscle lengths between the two groups. The study has been summarised in a journal article and submitted to the journal *Clinical Biomechanics* (Oberhofer et al., 2009c). The chapter is divided into (i) Introduction, (ii) Subjects and Methods, (iii) Results and (iv) Discussion.

4.1 Introduction

Anatomically-based, subject-specific models of muscle structures allow for the derivation of muscle volumes and muscle lengths. Muscle volume and muscle length are two important parameters for improving management strategies in children with CP as they provide more insight into the structural alterations that occur secondary to the neurological disorder. Muscle volume is linearly related to the maximal force generating capabilities (Fukunaga et al., 2001; Lieber & Friden, 2000) and may further help in better defining the dosing standards for Botulinum Toxin A injections (Bandholm et al., 2007). However, no study has yet reported on volumes and lengths in the muscles of the shank and the thigh in children with CP compared to typically developing children because of the limitations in measuring lower limb muscles *in vivo*.

Ultrasound-based imaging techniques allow the estimation of muscle architecture *in vivo*. However, ultrasound measurements are largely restricted to su-

perforial muscles in the calf (Bandholm et al., 2007), and have mainly been adopted to investigate the morphological alterations of gastrocnemius in children with CP (Fry et al., 2007; Malaiya et al., 2007; Mohagheghi et al., 2008; Shortland et al., 2002). Generally, a reduced volume and a shorter length of gastrocnemius have been reported in the affected limbs of children with hemiplegic CP compared to the non-affected limbs (Malaiya et al., 2007; Mohagheghi et al., 2007) and compared to age-matched control children (Fry et al., 2007). Interestingly, Malaiya et al. (2007) found a significant relationship between the normalised volume and the normalised length of gastrocnemius in children with CP but not in the control group.

In contrast to ultrasound measurements, MRI provides an attractive imaging technique that enables the accurate acquisition of all lower limb muscles without exposing the subject to harmful radiation (Elder et al., 2003; Fukunaga et al., 1992, 2001; Lampe et al., 2006). Elder et al. (2003) assessed muscle volume in the shank of five children with CP and a group of children without neurological impairment using MRI. Muscle volume was calculated as the sum of the anatomical cross-sectional areas plus the area between the slices. Muscle volumes in the affected legs of children with CP were found to be reduced between 25 to 30 %.

Lampe et al. (2006) measured muscle volume of 13 lower limb muscles in 16 young adults with hemiplegic CP by interpolating the distances between 2D-spline contour lines. All lower limb muscles in the affected limbs of the subjects with CP were found to be smaller than in the unaffected limb. The atrophy was more significant in the muscles of the shank with a reduction up to 28 % compared to the thigh with a reduction up to 16 %. The results were not compared to a group of typically developing adults, and no study has confirmed these findings in children with CP.

4.1.1 Aim

The aim of the present study was to use MRI and anatomically-based, subject-specific modelling techniques to compare the lengths and volumes of six lower-limb muscles between children with CP and typically developing children. It was hypothesised that the overall muscle volume in the affected leg of children with CP is significantly smaller compared to the age-matched control group, with the volume reduction being more dominant in the shank than the thigh.

Muscle lengths of the calf muscles in children with CP were expected to be shorter compared to children without CP, whereby the shorter muscle lengths in children with CP were expected to be related to the smaller muscle volumes.

4.2 Subjects and Method

4.2.1 Subjects

Four children with spastic diplegic CP, two children with spastic hemiplegic CP and five age-matched children without neurological disorder were recruited. Children with CP were recruited by a clinical nurse at the Wilson Centre and the Starship Children's Hospital, Auckland, New Zealand. Children for the control group were recruited through advertisements within the ABI and the Medical School at the University of Auckland.

The children with CP were all diagnosed with calf tightness in the affected leg. Spasticity was measured according to the modified Ashworth Scale (Bohannon & Smith, 1987), and ranged between Ashworth grade 1 and 2. All children, except one child with spastic hemiplegia CP, also had spasticity in the hamstrings and rectus femoris (Ashworth grades 1 - 2). Their functional motor abilities, classified by a physiotherapist according to the Gross Motor Function Classification (GMFC) system, ranged between I and II, i.e. able to walk without ambulatory aides (Rosenbaum et al., 2008). None of the children had previous orthopaedic surgery to the lower limbs and had not received Botulinum Toxin A injection in the six months prior to data acquisition. The characteristics of the participants are given in Table 4.1 and Table 4.2.

4.2.2 Data Acquisition

MRI scans of the lower limbs of all subjects were acquired on a Siemens 1.5T MAGNETOM Avanto System at the Centre of Advanced MRI, University of Auckland. After consultation with a clinical radiographer, the scan parameters were set to: TR-3690 ms, TE-67 ms, slice thickness 4 mm, base resolution 320, and gap between slices 10 mm. The chosen values of 4 mm for slice thickness and 10 mm gap between slices resulted in the minimum number of images possible to ensure sufficient data for developing accurate muscle models of each subject.

Table 4.1: Subject characteristics of the children without CP.

	gender	age [y]	weight [kg]	height [cm]	CP	GMFC
001	m	10.3	36	148	-	-
002	m	8.6	30	138	-	-
003	f	11.0	26	135	-	-
005	f	11.5	44	160	-	-
006	m	9.4	32	144	-	-
Avg	-	10.2	34	145	-	-
Std	-	1.2	6.8	9.8	-	-

Table 4.2: Subject characteristics of the children with CP.

	gender	age [y]	weight [kg]	height [cm]	CP	GMFC
004	g	9.4	28	129	hem	I-II
007	g	12.3	36	146	dip	II
008	g	8.8	21	118	dip	II
009	m	8.9	29	135	dip	I
010	m	7.9	27	131	dip	II
011	m	10.2	31	132	hem	I
Avg	-	9.6	29	132	-	-
Std	-	1.5	4.9	9.1	-	-

MRI slices were taken from the upper rim of the pelvis to the tip of the toes with the subject lying in supine posture with the ankle, knee and hip in neutral relaxed position. A total of three stacks had to be taken to scan the entire lower limbs. The scan time for one stack was approximately three minutes. The overall scan time, including an initial test trial to set up the scan parameters, was approximately 15 minutes.

Anatomical coordinate systems were derived from the MRI data as described in Section 3.2, allowing the calculation of joint angles and segmental lengths. Joint angles were calculated according to Grood & Suntay (1983); thigh and shank lengths were defined as the distances between hip and knee joint centers and knee and ankle joint centers respectively, Table 4.3.

Table 4.3: Segmental lengths and joint flexion angles during the MRI scan computed according to Grood & Suntay (1983). The values are given for the left legs of the control group (n=5), the children with spastic diplegia CP (n=4) and the children with spastic hemiplegia CP (n=2).

Parameter	Unit	control	CP di	CP hemi
Thigh length [†]	[cm]	34 (3.0)	32 (2.3)	30 (0.6)
Shank length [†]	[cm]	35 (2.9)	33 (2.8)	31 (1.7)
Hip flexion	[°]	15 (4.9)	11 (7.2)	18 (2.4)
Knee flexion	[°]	8 (3.7)	7 (14.1)	2 (3.1)
Ankle plantarflexion	[°]	26 (5.5)	22 (3.3)	26 (2.5)

[†] Significant difference between the children with and without CP (unpaired Student's t-Test, $p < 0.05$).

4.2.3 Data Processing

The development of subject-specific, anatomically-based models based on MRI data has previously been described in Section 3.1, and is only briefly addressed in this chapter. The soft tissue contrast of the images allowed for identification and manual digitisation of the muscle boundaries of soleus, gastrocnemius medialis and lateralis, semimembranosus, semitendinosus, rectus femoris, vastus lateralis, vastus medialis, vastus intermedius and the long head of biceps femoris, Fig. 4.1. Semimembranosus and semitendinosus as well as the vasti group were represented as one muscle. Note that only the muscle bellies were captured in the present study and the tendon parts were excluded from the analysis.

The FF technique was adopted to develop subject-specific, anatomically-based models of each muscle structure. A new FE mesh was developed for each structure, and twice fitted to the subject-specific data from MRI. The geometric coordinates of all FE meshes were interpolated using bicubic-linear interpolation functions. The Sobolev penalty parameters, Eq. 3.7, were set to 0.01 in the first fit and 0.001 in the second fit respectively. The accuracies in the representation of the muscle geometries were assessed by computing the RMS error between the digitised data points and their projection points onto the external faces of the final mesh. The final subject-specific models of one representative child of each group are shown in Figure 4.2 (supplementary movie, Appendix F.1).

The volume \mathcal{V} of each subject-specific muscle model was numerically evaluated

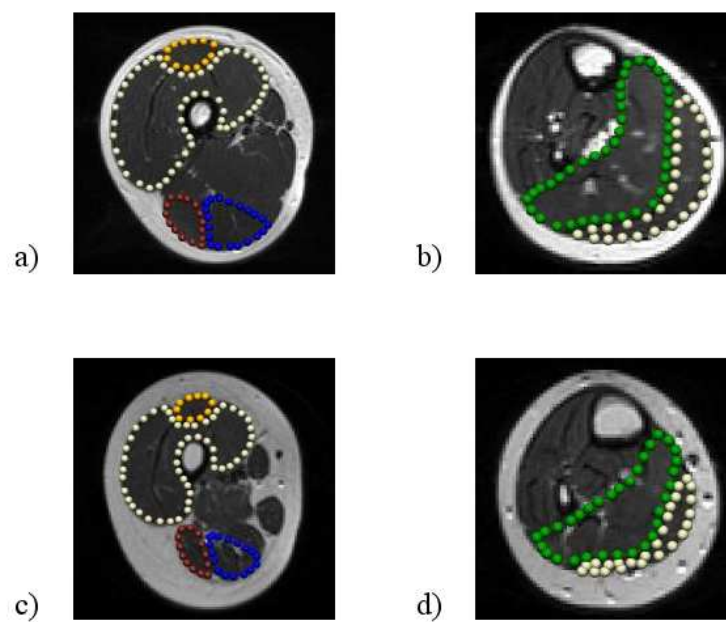


Figure 4.1: MRI slices of a) the thigh and b) the shank in a typically developing child (subject 005, Table 4.1), and b) the thigh and c) the shank in a child with hemiplegic CP (subject 004, Table 4.2). The muscles are coloured as follows: rectus femoris in gold, vasti in silver, biceps femoris in red, semimembranosus in blue, soleus in green and gastrocnemius in white.

using Gaussian quadrature

$$\mathcal{V} = \int_0^1 \int_0^1 \int_0^1 J_{3D}(\xi_1, \xi_2, \xi_3) d\xi_1 d\xi_2 d\xi_3 = \sum_{g=1}^{N_g} w_g J_{3D}(\xi_1^g, \xi_2^g, \xi_3^g), \quad (4.1)$$

where w_g is the weight associated with Gauss point g and $J_{3D}(\xi_1^g, \xi_2^g, \xi_3^g)$ the corresponding Jacobian respectively. N_g is the total number of Gauss points. Muscle volumes were normalised with respect to body mass.

Muscle length was defined as the average arc length between the most distal and most proximal end of the muscle model, which could be derived from the known nodal parameters of the FE mesh. Muscle lengths were normalised with respect to segmental lengths. Segmental length was defined as the distance between the ankle and the knee joint centre for the calf muscles and the distance between the knee and the hip joint centre for the thigh muscles. The joint centres were derived from the MRI images with the knee joint centre defined as the mid point between the femoral epicondyles, and the ankle joint centre as the midpoint between the lateral and medial malleolus respectively.

4.2.4 Data Analysis

All parameters were tested for a normal distribution prior to data comparison using the Kolmogorov and Smirnov method. Differences between the left and right leg in each child were examined using paired Student's t-test for muscle lengths (normally distributed) and Wilcoxon matched-pairs, signed-ranks test for muscle volumes (not normally distributed).

The normalised data from the left leg of the children with diplegia CP were combined with the data from the affected leg of the children with left hemiplegia CP to allow for statistical analyses of the differences between the CP group and the left legs of the control group. The relationships between (i) muscle volumes and body mass, (ii) muscle lengths and segmental lengths, and (iii) normalised muscle volumes and normalised muscle lengths were determined for the two groups by computing the coefficient of determination (R^2) from linear regression analysis. The differences in muscle volumes and muscle lengths in the left legs of the two groups were compared using unpaired Student's t-test.

Statistical analysis was done using the statistical software GraphPad IntStat. The level of significance was set at $p < 0.05$ for all statistical test.

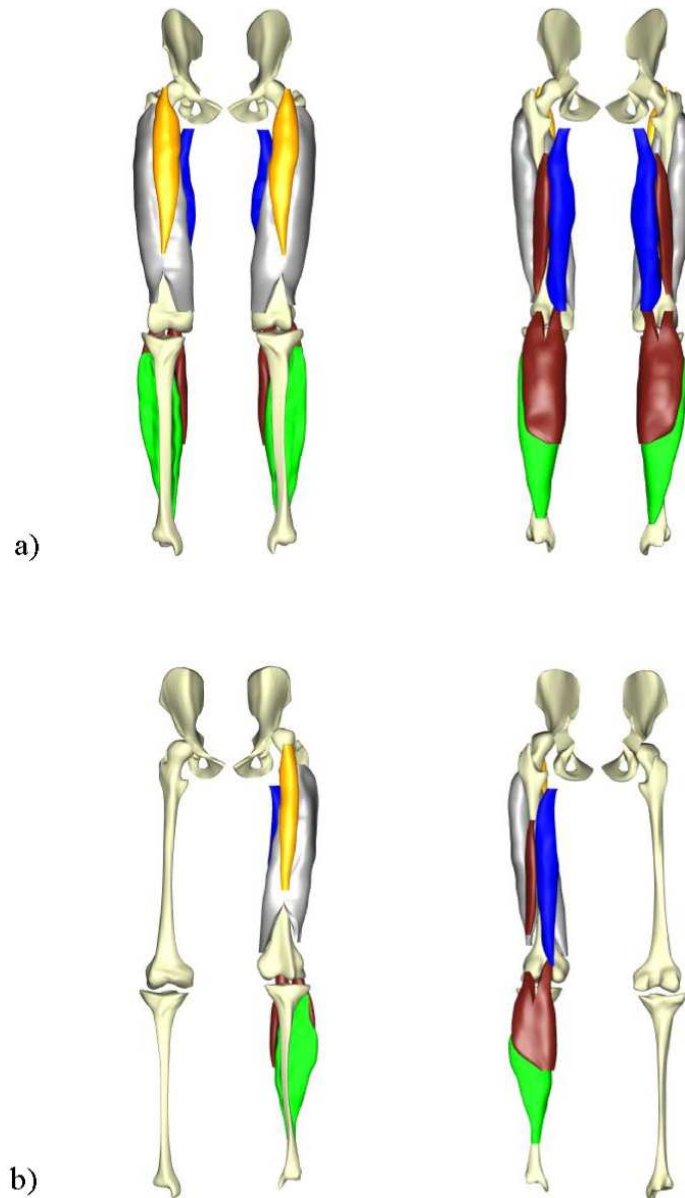


Figure 4.2: Subject-specific anatomically-based model from anterior and posterior view of a) a typically developing child (subject 005, Table 4.1) and b) a child with hemiplegic CP (subject 004, Table 4.2). The muscles are coloured as follows: rectus femoris in gold, vasti in silver, biceps femoris in red, semimembranosus in blue, soleus in green and gastrocnemius also in red (supplementary movie, Appendix F.1). Note that only the muscle bellies were captured in the present study and the tendon parts were excluded from the analysis.

4.3 Results

The two groups did not significantly differ in age, weight and height. However, the children with CP had significantly shorter shank lengths ($p = 0.001$) and thigh lengths ($p = 0.02$) than the children without CP. No statistically significant differences were found in the hip, knee and ankle flexion angles which were adopted during MRI data acquisition, Table 4.3. An average number of 686 data points per muscle structure were digitised based on the image data. A total of 120 subject-specific muscle structures were developed with an average RMS error of 0.7 ± 0.24 mm.

4.3.1 Regression Analysis

A significant relationship was found between body mass and the volumes of gastrocnemius, biceps, vasti, semimembranosus and semitendinosus in both groups, and soleus in the children without CP. There was a trend towards a linear relationship between soleus volumes and body mass in the children with CP with $R^2 = 0.440$ ($p = 0.073$), and between rectus volumes and body mass in both groups with $R^2 = 0.453$ ($p = 0.068$) in the children with CP and $R^2 = 0.559$ ($p = 0.053$) in the typically developing children.

A significant relationship was found between segmental lengths and the lengths of rectus, vasti, semimembranosus and semitendinosus. The relationship between biceps lengths and thigh lengths was not statistically significant in both groups with $R^2 = 0.042$ ($p = 0.626$) in the children with CP and $R^2 = 0.533$ ($p = 0.062$) in the typically developing children. No significant relationship was found between soleus lengths and shank lengths in the children with CP ($R^2 = 0.375$, $p = 0.106$) and between gastrocnemius lengths and shank lengths in the typically developing children ($R^2 = 0.443$, $p = 0.103$), Fig. 4.3.

No significant relationship was found between normalised muscle volumes and normalised muscle lengths for all muscles in both groups, Fig. 4.3.

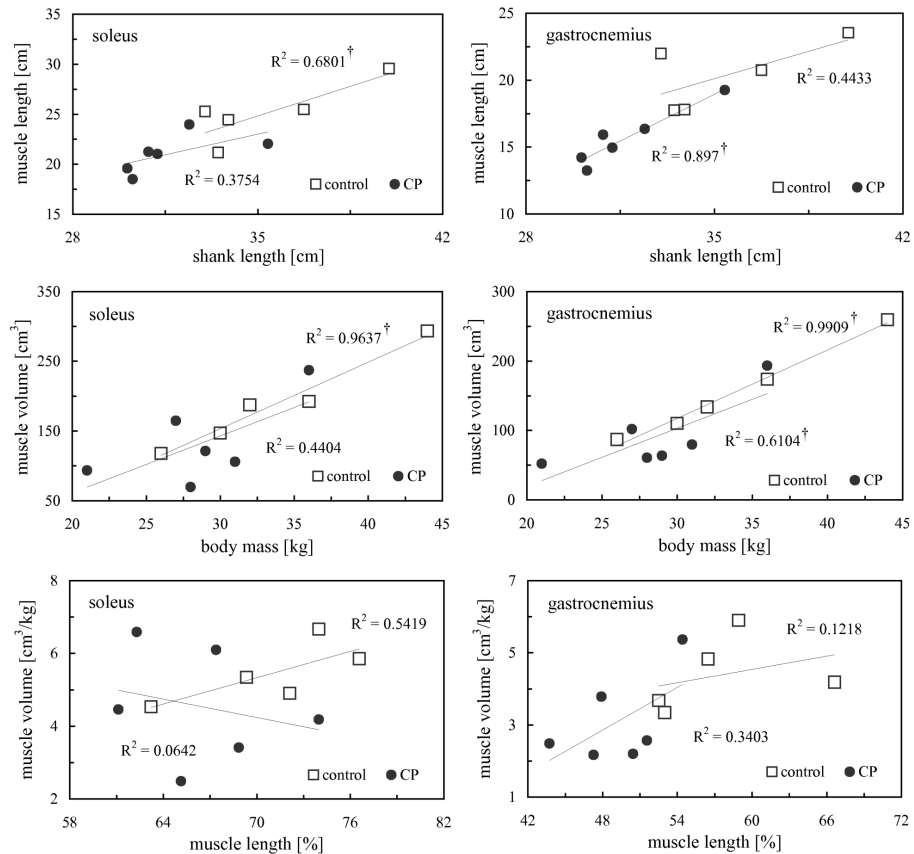


Figure 4.3: Results from linear regression analysis for soleus and gastrocnemius including coefficient of determination R^2 between muscle lengths and segmental lengths (top), muscle volume and body mass (middle), and normalised muscle volume and normalised muscle length (bottom).

† A linear relationship was found between the two variables ($p < 0.05$).

Table 4.4: Mean normalised muscle volume and normalised muscle length (SD) in the left legs of the control group (n=5) and the children with CP (n=6).

	muscle volume [$\frac{cm^3}{kg}$]			muscle length [%]		
	control	CP	p-value	control	CP	p-value
soleus	5.5 (0.84)	4.5 (1.56)	0.270	71 (5.1)	66 (4.7)	0.157
gastro	4.4 (1.01)	3.1 (1.26)	0.099	58 (5.8)	49 (3.9)	0.018 †
biceps	2.3 (0.44)	1.6 (0.41)	0.028 †	58 (4.6)	54 (3.7)	0.285
semi	5.1 (0.91)	3.9 (0.88)	0.051	82 (3.3)	76 (7.2)	0.008 †
rectus	3.6 (0.69)	2.6 (0.63)	0.032 †	76 (1.3)	68 (3.1)	< 0.001 †
vasti	20.3 (2.80)	15.9 (3.20)	0.043 †	90 (4.8)	82 (3.0)	0.004 †

† The difference between the two groups is statistically significant (unpaired Student's t-test, $p < 0.05$).

4.3.2 Muscle Volumes and Muscle Lengths

The mean normalised volumes and lengths of all muscles in the children with diplegia CP and hemiplegia CP were smaller compared to the typically developing children, Fig. 4.4. Overall, the lower limb muscles in the children with hemiplegia CP showed a trend towards being smaller but longer when compared to the children with diplegia CP, except rectus femoris which was smaller and shorter.

The mean normalised muscle volume in the left legs of all children with CP was 77 (18) % of the mean volume in the typically developing children, which was statistically significant ($p = 0.049$). The mean volume of the calf muscles in the children with CP was 78 (27) %, the volume of the hamstrings 74 (17) % and the volume of the quadriceps 78 (16) % of the corresponding mean volumes in the typically developing children. Only the differences in the volumes of the hamstrings and the quadriceps were statistically significant ($p = 0.036$, $p = 0.038$). Neither gastrocnemius nor soleus were found to be significantly smaller in the children with CP when compared to the typically developing children, Table 4.4.

4.4 Discussion

Subject-specific, anatomically-based models of muscle structures were shown to provide useful insights into the structural alterations of spastic muscles in children with CP. Bicubic-linear FE models were fitted to the MRI data using the FF technique, resulting in an average fitting error of less than 1 mm for 120

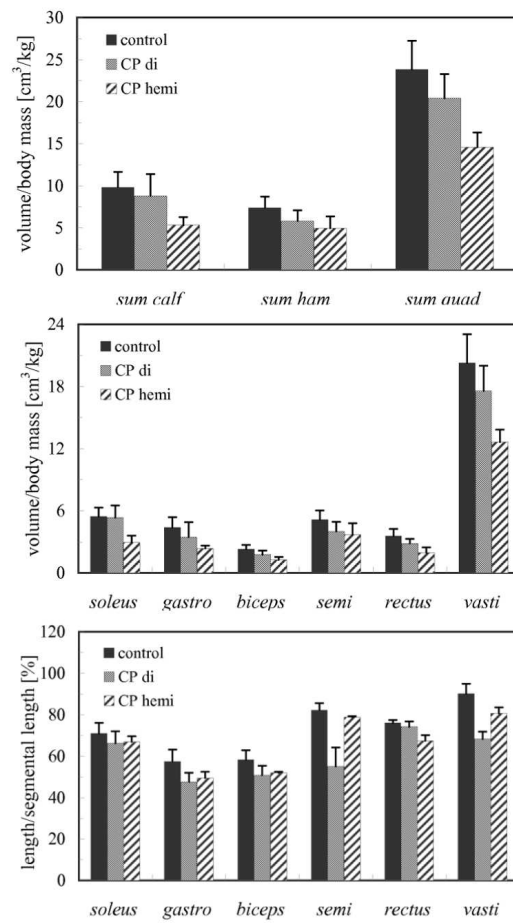


Figure 4.4: Mean normalised muscle volumes and lengths (SD) in the left legs of the control group (n=6), the children with diplegia CP (n=4) and the children with hemiplegia CP (n=2).

muscle structures. The hypothesis that the lower limb muscles in children with CP are generally smaller when compared to typically developing children was corroborated. We found an overall muscle volume reduction of 22 % in the calf muscles, 26 % in the hamstrings and 22 % in the quadriceps respectively. Only the differences in the hamstrings and the quadriceps were statistically significant ($p = 0.036$, $p = 0.038$). Normalised muscle lengths in the children with CP were significantly shorter ($p < 0.05$), except for soleus and biceps femoris.

Our findings extend the results of Lampe et al. (2006) and show that the thigh and shank muscles are not only smaller in the affected legs of young adults with spastic hemiplegic CP but also in children with CP compared to typically developing children. The small differences in the lengths and volumes of soleus between the two groups may have been due to the high functional level of the children with CP (GMFCS I - II), i.e. able to walk independently without ambulatory aids. In normal gait, a large proportion of power is generated by the plantarflexors during terminal stance and push off (Gage, 2004). Interestingly, the muscles in the paretic legs of the children with hemiplegia CP showed overall a trend to be smaller but longer than in the children with diplegia CP, Fig. 4.4. The smaller volume might be explained by a compensation mechanism of the non-paretic leg to account for the reduced functional level of the paretic leg (Malaiya et al., 2007; Mohagheghi et al., 2007).

Most of the muscles were found to be significantly shorter in the children with CP when normalised to segmental lengths. The normalisation of muscle lengths to segmental lengths has been assumed to minimise the non-clinical variation of these parameters (Fry et al., 2007; Malaiya et al., 2007; Shortland et al., 2002); though, no significant relationship was found for soleus and biceps femoris. The small number of subjects in each group could explain some of these results. However, it may also be possible that the relationship between segmental lengths and muscle lengths in the children with CP is altered due to abnormal muscle functioning. This assumption would be supported by the significantly smaller shank and thigh lengths found in the children with CP compared to the typically developing children even though there was no difference in overall height between the two groups.

The small fitting error between the image data and the subject-specific models supports previous studies and highlights the value of MRI and high-order finite element models in capturing the architecture of skeletal muscles in the lower

limbs (Bradley et al., 1997; Fernandez et al., 2004). However, taking MRI of the entire lower limbs in children with CP poses several challenges. A long acquisition time increases the risk of voluntary physical movement, leading to a loss in image clarity, while a short acquisition time requires the number of images to be reduced, leading to a loss of information because of the wider gap between slices. The scan parameters in the present study were chosen to ensure sufficient data for developing subject-specific anatomically-based models using the FF technique. However, the accuracy in the anatomical representation of the muscle structures is limited both by the gap size and by motion artefacts which could not entirely be avoided.

The mechanical performances of skeletal muscles are largely determined by the material properties of muscle tissue and the architectural design of the muscle-tendon unit (Fukunaga et al., 2001; Lieber & Friden, 2000; Wickiewicz et al., 1983). Our results suggest that the volumes and lengths of lower limb muscles in children with CP are significantly altered compared to typically developing children. The generally shorter muscle lengths suggest that the tendons in children with CP are longer, resulting in an overall stiffer muscle-tendon unit (Nigg & Herzog, 1999). Recent studies suggest that the mechanical properties of muscles in children with CP are also altered at the cellular level; the stiffness of individual muscle cells from the upper limb in children with CP were found to be nearly double the stiffness of normal muscle cells (Friden & Lieber, 2003). Hence, both structural and cellular alterations may affect the mechanical performance of skeletal muscles in children with CP and impact on the ability to perform daily activities such as walking.

The extent of the functional weakness and the details of the altered mechanical properties in spastic muscles of children with CP are poorly understood, and their influences on motion patterns such as walking remains unclear. Future work in MRI imaging and musculoskeletal modelling should aim to capture the macro- and microscopic architecture of lower limb muscles in a larger group of children with CP, and link the resulting insights with dynamic simulations of walking. Extensive investigations of lower limb muscles in children with CP may not only provide new insights into the structural alterations that occur secondary to the neurological disorder but may also help for better evaluating treatment outcomes from serial castings or soft-tissue muscle surgeries.

5

Study II: Prediction and Validation of Muscle Deformation in the Low Limbs During Gait

The following chapter outlines a study for the development of an anatomically-based lower limb model that allows the accurate prediction of muscle soft-tissue deformation during walking. A summary of the study has been successfully published in *The Visual Computer* (Oberhofer et al., 2009a). The chapter is divided into (i) Introduction, (ii) Subjects and Methods, (iii) Results and (iv) Discussion.

5.1 Introduction

Muscle functioning during walking is of great interest in the clinical assessment of children with CP. However, measuring muscle functioning *in vivo* is difficult, and musculoskeletal models are needed for providing more insight into underlying muscle structures. To date, clinical gait analysis has relied on simplified 1D muscle models for the derivation of physiological parameters such as muscle lengths and muscle forces (Arnold et al., 2005, 2006b,a; Jonkers et al., 2006; Wren et al., 2004). However, experimental and computational results on the muscle structures suggest that muscle functioning is predetermined by material properties and by anatomical features such as cross-sectional area, fibre angle and fibre length (Blemker et al., 2005; Blemker & Delp, 2006; Lieber & Friden, 2000; Roehrlé & Pullan, 2007).

Anatomically-based FE models in biomechanical research allow for investiga-

tions of the mechanical behaviour of muscles under loading (Blemker et al., 2005; Blemker & Delp, 2006; Roehrlé & Pullan, 2007). However, solving the governing equations of finite elasticity for several muscles over multiple time steps is computationally expensive; even more so when contact between bodies becomes an issue. Hence, mechanics-based deformation techniques have largely been confined to small movements and are considered too mathematically involved for gait analysis (Blemker et al., 2005; Roehrlé & Pullan, 2007; Teran et al., 2005).

Geometric-based deformation methods, in particular free-form deformation techniques, have extensively been used in computer graphics research for obtaining visually realistic deformations of complex structures (Magnenat-Thalmann & Thalmann, 2005). However, the free-form deformation methodology, especially the HMF technique, has only recently been introduced in biomechanical modelling of the musculoskeletal system (Fernandez et al., 2004, 2005). The HMF technique has never been applied to more than two muscles, and its validity remains unclear.

The validation of a computational model is crucial if the model is to be used for wider applications. Musculoskeletal models have previously been validated by comparing predicted deformations with MRI data (Blemker & Delp, 2005; Vasavada et al., 2008), or by comparing output parameters with measurements on cadaveric specimens (Arnold et al., 2000). MRI provides an attractive methodology for validating computational models of the musculoskeletal system (Blemker & Delp, 2005; Vasavada et al., 2008); though, imaging under physiological loading is challenging. Dynamic and real-time MRI techniques have previously allowed for investigations of muscle deformation during motion (Asakawa et al., 2002, 2003). Furthermore, Gold et al. (2004) introduced a custom-designed open MRI scanner for accurately imaging patellofemoral cartilage under physiological weight-bearing conditions. However, difficulties have remained with image quality, the spatial boundaries of the scanner, and the image segmentation (Blemker et al., 2007).

5.1.1 Aim

The aims of the present study were to develop an anatomically-based, subject-specific model of the lower limbs, to adopt the geometric-based HMF technique for predicting muscle deformations during walking and to validate the model

prediction. The HMF solution was to be validated using MRI data in two different lower limb positions. Based on the preliminary results reported in Fernandez et al. (2005), it was expected that the HMF technique provides a useful methodology for accurately deriving the deformations of lower limb muscles from inverse kinematics.

5.2 Subjects and Methods

5.2.1 The Lower Limb Model

A subject-specific, anatomically-based FE model of the lower limbs of an adult female subject (age 29 y, height 165 cm, weight 63 kg) was developed from MRI as described in Section 3.1. The MRI scan was obtained using the same facility and scan parameters as for the study on children with CP outlined in Chapter 4 (Siemens 1.5T MAGNETOM Avanto System, scan parameters TR-3690 ms, TE-67 ms, slice thickness 4 mm, base resolution 320, gap between slices 10 mm). Image segmentation was done manually, whereby the soft tissue contrast of the images allowed for identification of skin, bone, tendon as well as muscle boundaries.

Subject-specific bone models were developed by customising a generic model from the ABI model library to the MRI data using the HMF technique. Subject-specific muscle models were developed using the FF technique. The geometric coordinates of the bone and muscle models were interpolated using bicubic-linear interpolation functions. The FE mesh details of the bone and muscle structures, including the number of landmark and target points that were used for the HMF customisation of the generic bone models from the ABI library, are given in the Appendix D in Table D.1 and Table D.2.

The MRI scan was taken with the subject lying in supine position; hence, the muscle shapes of the subject-specific lower limb model did not resemble the natural shapes in standing position. In order to more accurately capture the muscle shapes in standing position, in particular for gluteus maximus and medius, a surface scan of the lower limbs was taken at Industrial Research Limited, Auckland, New Zealand, using a custom-designed, purpose-built laser scanner. The data cloud from the surface scan was imported into CMISS and manually transformed to line up with the lower limb model. The shapes of gluteus maximus

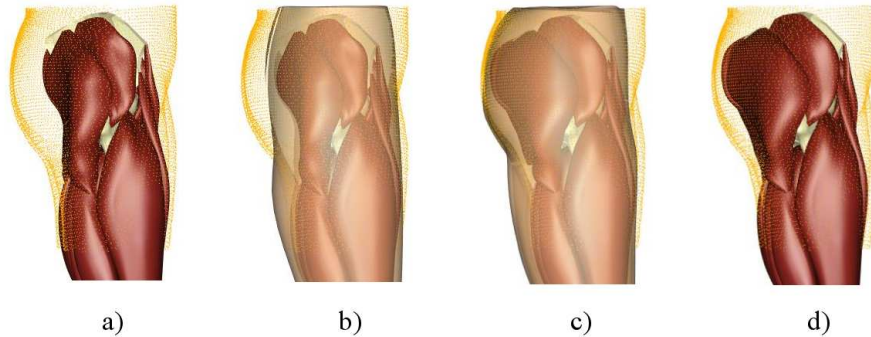


Figure 5.1: Refitting of gluteus maximus and medius to the data cloud from the surface scan with the model shown in a) initial position, b) with the initial skin-based mesh, c) with the deformed skin-based mesh and d) in the deformed position.

and medius in standing position were then derived by fitting a skin-based mesh to the data cloud using the FF technique, and updating the enclosed muscle structures accordingly, Fig. 5.1. The final anatomically-based model of the lower limbs in neutral standing position, comprising all lower limb bones and 20 muscle structures in each leg, is illustrated in Figure 5.2 (supplementary movie, Appendix F.2).

5.2.2 Kinematic Data

Kinematic data were acquired on the same subject at the Gait Laboratory, Tamaki Campus, University of Auckland, using an 8-camera VICON Workstation Version 5.0 (Oxford Metrics Ltd., Oxford, England) at 100 Hz. The subject walked barefoot at a self-selected speed on a 10 m walkway. The Cleveland Clinic marker set was adopted, Fig. 3.7a-c.

Segmental kinematics was derived from the skin marker positions as described in Section 3.2 using the mathematical computing environment and programming language MATLAB (The MathWorks Inc., Massachusetts, USA). The calculated Euclidean transformation matrices for each segment throughout gait were applied to every node of the FE bone models within CMISS by writing corresponding software using the scripting language perl. All joints were modelled as ball-and-socket joints with three rotational DOF only.

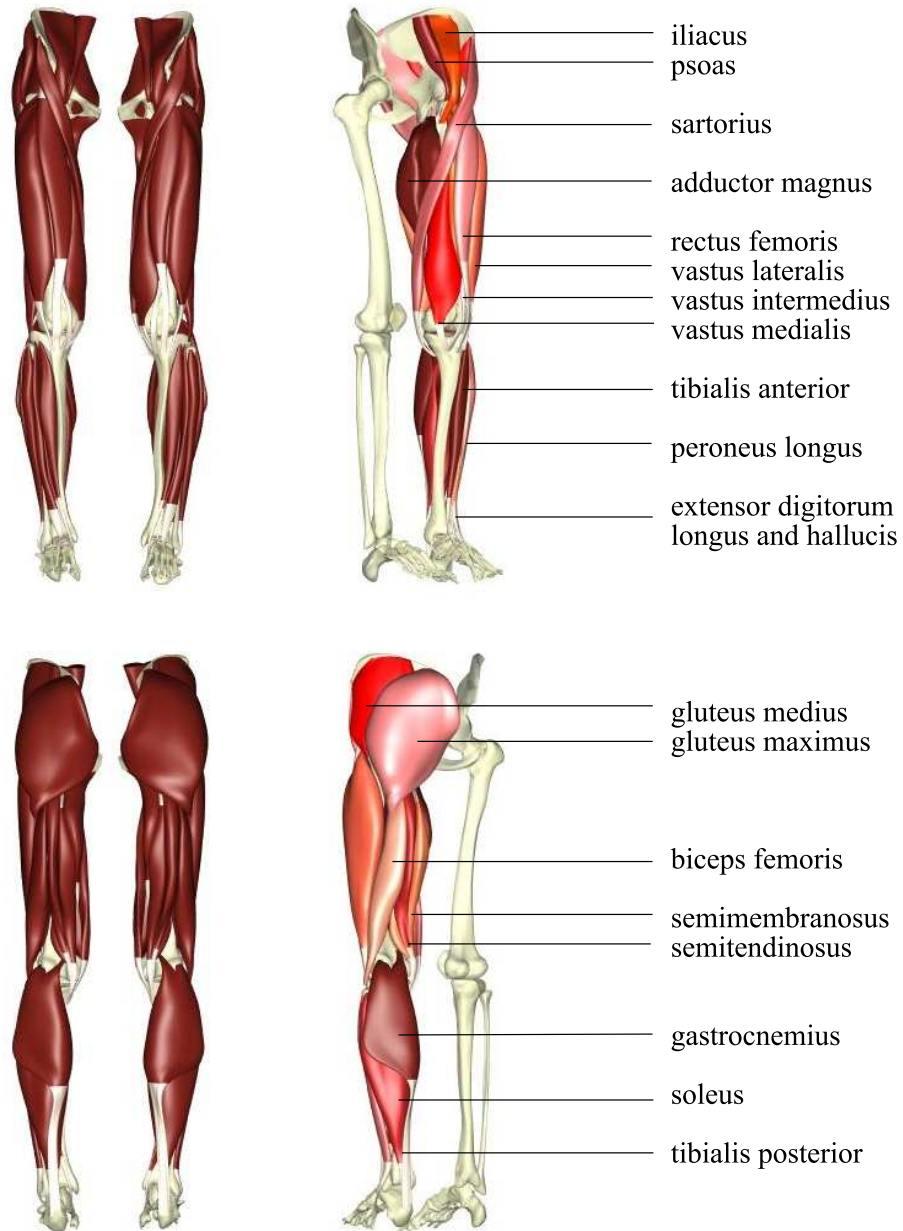


Figure 5.2: Subject-specific, anatomically-based model of the lower limbs including 20 muscles in each leg from anterior (top) and posterior (bottom) view (supplementary movie, Appendix F.2).

5.2.3 Modelling Soft-Tissue Muscle Deformation

The geometric-based HMF technique, introduced in Section 3.3, was adopted for predicting muscle soft-tissue deformation during walking based on segmental kinematics. All lower limb muscles were embedded into the same skin-based host mesh instead of defining an individual host mesh for each muscle structure as described in Fernandez et al. (2005). The skin-based host mesh was deformed according to the known position of so-called control points; and the geometries of the enclosed muscles were updated based on the HMF solution. A flowchart of the entire modelling process from the kinematic data to muscle soft-tissue deformations is given in Figure 5.3. The modelling process was made automatic by writing extensive software using the scripting language perl in order to link the individual calculations within CMISS.

Kinematic Constraints

Segmental kinematics provided the kinematic constraints for deriving soft-tissue muscle deformations during walking. In addition to the attachment points, further points along the centre lines of the FE muscle meshes were defined in the initial undeformed state, and were assumed to be rigidly connected to one particular bone, Fig. 5.4a. The additional points were based on the concept of via-points, Fig. 2.1, aimed at constraining the muscle paths around joints. The attachment points and the via-points combined were named *control points*. The number of control points for each muscle structure are given in the Appendix D in Table D.2. A total number of 272 control points were defined per limb.

The Skin-Based Host Mesh

As described in Section 3.3, free-form deformation techniques allow for deforming several structures in accordance with the deformation of a surrounding simple mesh. We took advantage of this special feature of the HMF technique by embedding all lower limb muscles of one leg into a skin-based host mesh. The skin-based host mesh was then deformed based on the positions of the control points during walking, and the enclosed muscle structures were updated accordingly.

Initially, a very simple linear host mesh was developed for each leg based on the digitised skin boundary from MRI. The simple host mesh was then iteratively re-

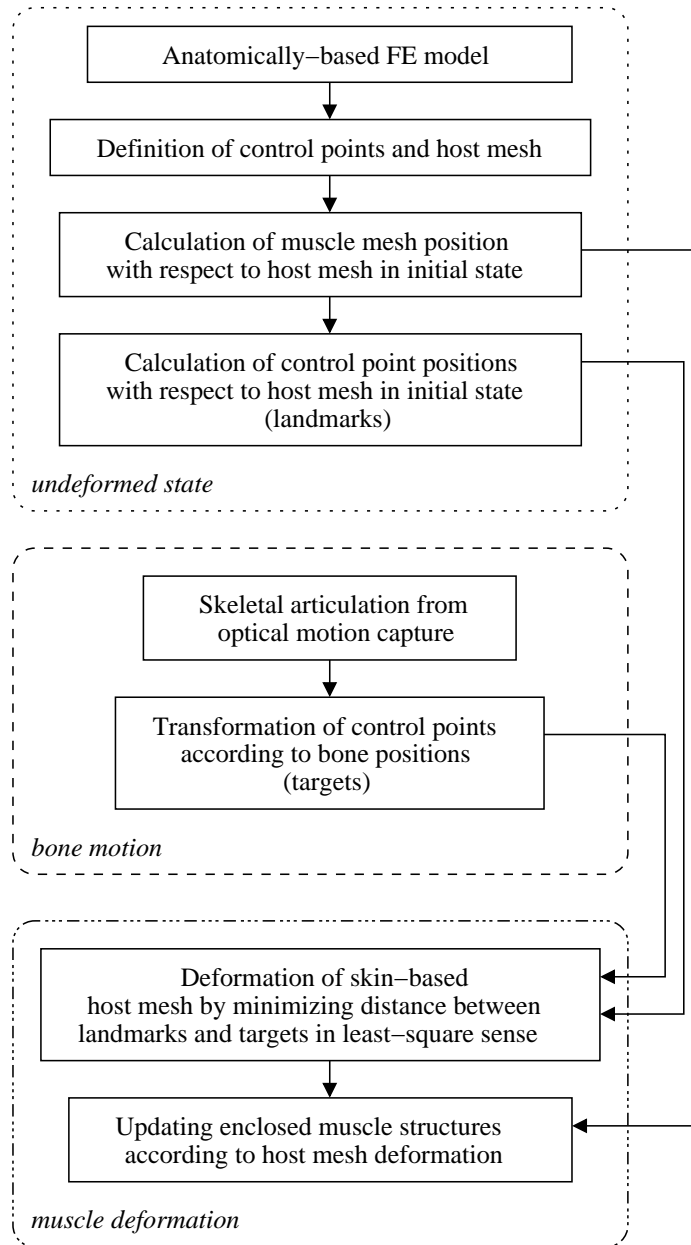


Figure 5.3: Flowchart of the modelling approach for deriving the muscle deformations in the anatomically-based model of the lower limbs from segmental kinematics.

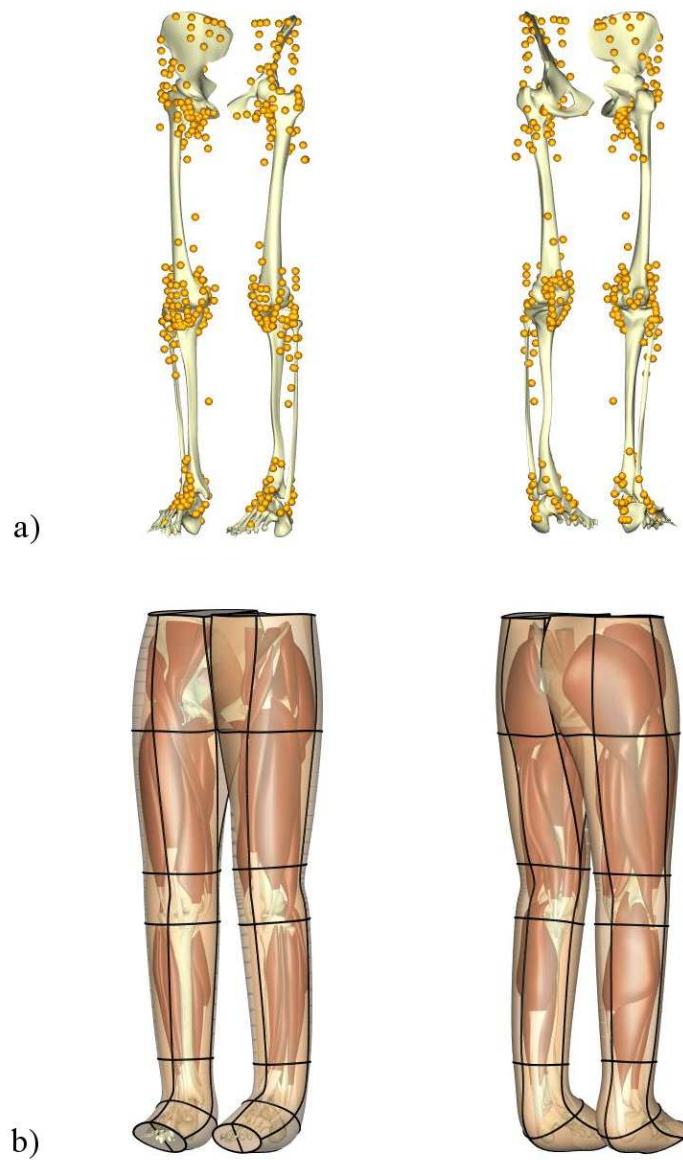


Figure 5.4: a) The control points and b) the skin-based host mesh with the enclosed muscle structures for the lower limb model (supplementary movie, Appendix F.2).

fined, and muscle deformations during walking were calculated for each iteration using the HMF technique. The resulting deformations were qualitatively compared, focusing on the wrapping of muscles around joints in case of high flexion angles. The best solution was found for a 12 element bicubic-linear host mesh with the Sobolev weights set to 0.01, Eq. 3.11. The corresponding skin-based host mesh for the right leg is shown in Figure 5.4b.

5.2.4 Validation

The predicted muscle deformations from the HMF solution were validated by comparing the shape changes with subject-specific MRI data. During a validation trial, MRI scans of the same female subject were taken in two different limb positions (position A and position B). Two foam wedges of different heights were positioned underneath the knee to support and elevate the leg in the two positions. Position B was constrained to the maximal knee flexion angle permitted within the scanner's dimension (diameter of the tube 60 cm). The knee flexion-extension angles were approximately 15° in position A and 45° in position B respectively, Fig. 5.5.

The bones were registered in both positions by transforming the subject-specific skeletal model according to the image data, Fig. 5.5. New subject-specific FE meshes were developed for the muscle structures in the two positions using the FF technique. The development of subject-specific muscle structures is a time-consuming procedure. For this reason, the analysis was constrained to one flexor and one extensor muscle for each joint. The selected muscles comprised iliacus, semimembranosus, rectus femoris, tibialis anterior and gastrocnemius.

The deformations of the muscles moving from position A to B were computed using the HMF technique, and the predicted shape changes were compared with the MRI data in position B. As error estimate, the image data in position B was projected onto the external surfaces of the deformed FE meshes, and the RMS error was computed between the data and the projection points. Except for iliacus, the RMS error was computed for the muscle and tendon parts of the FE mesh separately. Iliacus was considered to comprise only muscle tissue.

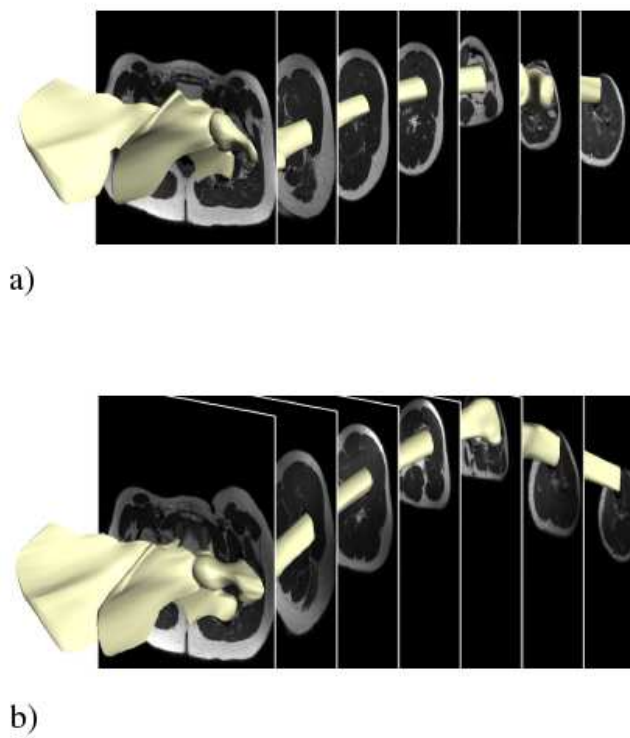


Figure 5.5: Bone structures were registered in position A and B based on the MRI data. The knee flexion-extension angles were approximately 15° in position A and 45° in position B respectively.



Figure 5.6: Resulting deformation of the skin-based host mesh of the right leg (supplementary movie, Appendix F.3).

5.3 Results

5.3.1 Walking Simulation

The results of the walking simulation for the subject-specific lower limb model are shown in Figure 5.6 and Figure 5.7 (supplementary movies, Appendix F.3 - F.5). The solution time for deforming the host mesh of one leg over 100 time steps, that corresponded to one gait cycle, was 63 sec on a desktop with an Intel Pentium 4 processor (3.4 GHz). Updating the geometry of one muscle throughout gait according to the host deformation took 53 sec. There were no obvious penetrations of muscles into bones throughout gait. The wrapping of muscles around joints was maintained, except for the knee extensors in the case of high knee flexion angles. Muscle-muscle penetration was avoided by embedding all muscle structures into the same skin-based host.

5.3.2 Validation

The initial muscle-tendon structures in position A were registered with average RMS errors of 0.7 mm for the tendon parts and 0.9 mm for the muscle parts respectively. There was generally good agreement between the predicted shape changes from the HMF solution moving from position A (15° knee flexion) to

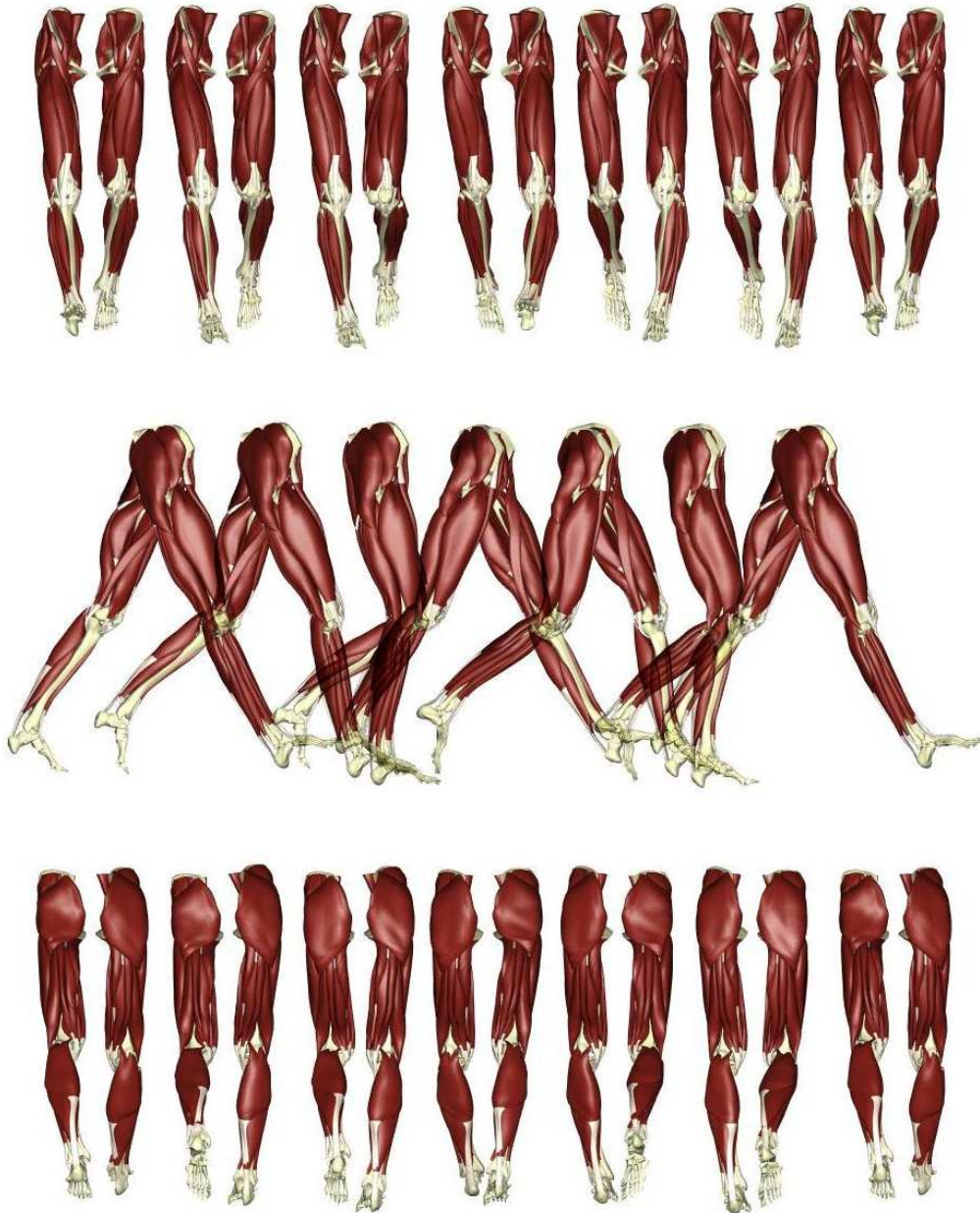


Figure 5.7: Gait simulation from anterior (top row), lateral (middle row) and from posterior view (bottom row) (supplementary movie, Appendix F.4).

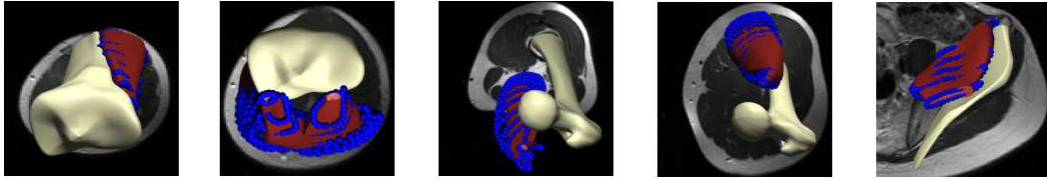


Figure 5.8: Comparison between the HMF solution and image data in position B for tibialis anterior, gastrocnemius, semimembranosus, rectus femoris and iliacus (from left to right).



Figure 5.9: Comparison between the HMF solution (red) and the subject-specific FE meshes based on the MRI data in position B (gold) with the model shown from lateral, anterior and posterior.

position B (45° knee flexion) and the MRI data in position B as illustrated in Figure 5.8 and Figure 5.9.

The RMS errors between the image data in position B and the projection of the data onto the deformed muscle meshes are given in Table 5.1. The most accurate deformation was predicted for the tibialis anterior with an RMS error of 0.9 mm for the tendon and 2.4 mm for the muscle belly respectively. The highest RMS error between the predicted deformation and the image data was found for semimembranosus with an RMS error of 2.2 mm for the tendon and 8.2 mm for the muscle belly respectively. The shape changes of the tendons were overall better predicted than the deformations of the muscle bellies, Table 5.1.

Table 5.1: RMS error of the predicted muscle-tendon deformation compared with the MRI data for the muscle belly and the tendon part.

	RMS error [mm]		data points	
	muscle	tendon	muscle	tendon
iliacus	3.9	-	474	-
rectus femoris	4.3	1.7	494	164
semimembranosus	8.2	2.2	493	93
gastrocnemius	4.3	1.5	649	80
tibialis anterior	2.4	0.9	449	46

5.4 Discussion

The geometric-based HMF technique enabled the efficient and realistic prediction of soft-tissue muscle deformations in the lower limbs during walking. The solution time for deforming 20 muscle structures in each leg throughout one gait cycle was less than 20 minutes. The validity of the proposed approach was demonstrated by moving five muscles over a range of 30° knee flexion angle with an average RMS error of 3.7 mm between the predicted shape changes and the MRI data.

The introduction of a skin-based host mesh had the advantage that the muscle positions with respect to each other were maintained and the implementation of a complex contact mechanics formulation could be avoided. However, the proposed approach does not allow for capturing the effects of active muscle contraction, muscle-muscle interaction or external forces on the muscle shape. This could be one of the reasons why the predicted deformation of the fleshy semimembranosus was less accurate than of the slender tibialis anterior, and why the tendon paths were generally better predicted than the deformations of the muscle bellies.

The anatomically-based model of the lower limb only captured the geometric boundary surfaces of muscle structures. However, previous studies demonstrated that fibre lengths and penetration angles change spatially within a muscle (Blemker & Delp, 2005; Roehrl & Pullan, 2007; Teran et al., 2005), as well as temporarily during motion (Lieber & Friden, 2000). The exclusion of macroscopic anatomical properties could explain some of the differences found between the model prediction and the image data, especially for iliopus which is known to have large intermuscular variations in fibre lengths (Klein Horsman et al., 2007).

Furthermore, the accessibility to a scanner that allowed imaging under physiological weight-bearing conditions, such as described in Gold et al. (2004), was not provided in the present work, and the model prediction had to be validated using a typical horizontal MRI unit.

The success of the HMF technique depends on the number and distribution of the control points, the geometry of the host and the magnitudes of the Sobolev smoothing constraints (Fernandez et al., 2004). Except for the muscle attachment points, these variables could not be linked to physiological properties and were defined according to subjective criteria. Even though we obtained a reasonable solution for modelling muscle deformation during walking, the application of the HMF technique to different motion patterns or other parts of the human body has to be further assessed and validated.

The definition of control points is not only crucial for deriving muscle-soft tissue deformation using the HMF technique but also for calculating muscle moment arms and muscle shortening velocities based on the muscle-tendon paths (Delp & Loan, 1995, 2000). Future work should aim to define standardised procedures for selecting control points based on objective criteria. An attempt for developing objective methods to select the shape, orientation, size and location of wrapping surfaces for the spinal muscle paths has been made by Vasavada et al. (2008). This work could provide a basis for better defining control points in the lower limbs.

The geometric-based HMF solution may be used in future work as displacement boundary condition for solving the governing equations of finite elasticity. The successful convergence of nonlinear boundary-value problems in continuum mechanics is more likely to be achieved if the initial guess is already close to the final displacement (Fernandez, 2004). Such a hybrid approach would allow for investigations of stresses and strains within muscles during walking, and would make a significant contribution in better understanding the biomechanics of muscle functioning during walking.

6

Study III: Accuracy in Modelled Muscle-Tendon Lengths During Gait

The following chapter outlines a study to assess the accuracy in modelled muscle-tendon lengths during walking. The error propagation from skin marker coordinates to muscle-tendon lengths was analytically described and applied to kinematic data of two subjects. A summary of the study has been successfully published in the *Journal of Biomechanics* (Oberhofer et al., 2009b). The chapter is divided into (i) Introduction, (ii) Subjects and Methods, (iii) Results and (iv) Discussion.

6.1 Introduction

Muscle-tendon length during walking is an important parameter in the assessment of children with CP, commonly derived using kinematic data from optical motion capture as input into musculoskeletal models (Arnold et al., 2005, 2006b; Delp et al., 1996; Scheepers et al., 1997; Wren et al., 2004). The validity of the geometric representation of musculoskeletal models has been demonstrated by comparing muscle lengths or muscle shapes for certain body positions against medical image data (Oberhofer et al., 2009a; Vasavada et al., 2008) or cadaveric experiments (Arnold et al., 2000).

However, the accuracy of musculoskeletal models in predicting parameters such as muscle-tendon lengths does not only depend on the accurate representation of the musculoskeletal geometry but also on the accuracy of the kinematic data which are used to drive the inverse kinematics simulation. One of the main error

sources of optical motion capture are STA which refer to movements of skin markers with respect to the underlying bones, Sec. 3.2.

STA have been shown to significantly affect the computation of joint kinematics, particularly in the frontal and transversal plane (Cappozzo et al., 1996; Cheze, 2000; Ramakrishnan & Kadaba, 1991; Reinschmidt et al., 1997). Thereby, various techniques of error propagation analysis have been deployed. Ramakrishnan & Kadaba (1991) as well as Cheze (2000) adopted a numerical approach and compared the differences in joint angle outputs from numerically perturbed kinematic data. The drawback of numerical techniques is that a great number of perturbation steps are needed to draw valid conclusions.

In contrast, Woltring et al. (1985) performed an analytical error analysis to determine the error propagation from noisy landmark measurements to joint angles. A zero-mean, isotropic, uncorrelated measurement error with a constant Standard Deviation (SD) was adopted for each skin marker coordinate to derive an analytically tractable formulae. Even though the error functions were considered much more complicated in reality, it was postulated that the general conclusions still hold.

Generally, it was found that flexion-extension angles can be reliably determined; however, for internal-external rotation and abduction-adduction angles, the errors introduced by STA were almost as high in magnitudes as the corresponding joint motion. Although the effect of STA on joint angles has extensively been described, the error propagation from STA to modelled muscle-tendon lengths has not been previously analysed.

6.1.1 Aim

The aims of the present study were to introduce an analytical method for calculating the error propagation from STA to modelled muscle-tendon lengths and to provide a first estimate of the accuracy of modelled muscle-tendon lengths derived from inverse kinematics for clinical gait analysis. Based on previous findings by Lu & O'Connor (1999), it was hypothesized that joint constraints would lead to error reductions in muscle-tendon lengths. To corroborate this hypothesis, two different musculoskeletal models were specified; one with the joints moving freely in all directions, and one with the joints constrained to rotation but no translation. In order to evaluate the validity of the analytical formulation, the

error propagation from STA to the knee joint angles was additionally computed and compared with previously published error magnitudes.

6.2 Subjects and Methods

6.2.1 Reference Kinematic Data

Kinematic data were acquired for two typically developing children (subject 001 and 002, Table 4.1) at the Gait Laboratory, Tamaki Campus, University of Auckland, using an 8-camera VICON Workstation Version 5.0 (Oxford Metrics Ltd., Oxford, England) at 100 Hz. Both subjects walked barefoot at a self-selected speed on a 10 m walkway.

A customised marker set was used for the data acquisition consisting of 41 reflective skin markers on the lower limbs, Fig. 3.7g-i. The segmental kinematics of the thigh and shank were derived from the corresponding marker clusters using the optimisation algorithm based on singular value decomposition proposed by Challis (1995). The algorithm is outlined in the Appendix C.

6.2.2 Musculoskeletal Model

Anatomical coordinate systems for bone structures were derived from the positions of anatomical landmarks as described in Section 3.2, Fig. 3.8. Initially, the segments were allowed to move freely in all directions. Treating segments independently can lead to apparent joint dislocation due to STA and consequently, to altered muscle lever arms and muscle paths. Lu & O'Connor (1999) showed that joint constraints considerably improved the estimation of segmental kinematics, and were as such expected to reduce the errors in muscle-tendon lengths. Hence, a second model was specified with the hip, knee and ankle joints constrained to rotation but no translation.

The muscle-tendon lengths of semimembranosus, gastrocnemius and soleus were derived from segmental kinematics, and used as reference data for the error propagation analysis. These three lower limb muscles were chosen as they are often shortened in children with CP, and have been modelled in previous studies (Arnold et al., 2006b; Delp et al., 1996; Scheepers et al., 1997; Wren et al.,

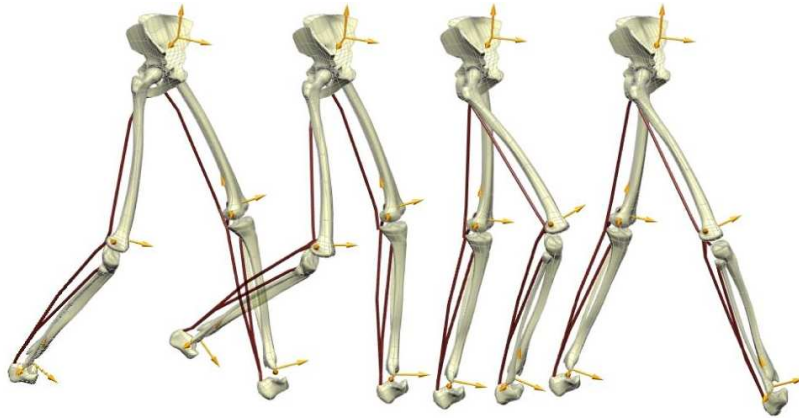


Figure 6.1: Anatomical coordinate systems (yellow) for each bone structure were derived from the kinematic data. Muscle-tendon lengths were approximated using straight-line segments (red) to allow for an analytical formulation.

2004). The muscle paths were approximated using straight-line segments to allow for an analytical formulation, Fig. 6.1. The local coordinates of the muscle attachment points were given with respect to the anatomical coordinate systems, Fig. 6.1. The global coordinates of the attachment points during walking were derived via coordinate transformations between the anatomical and the laboratory coordinate system. Muscle-tendon lengths were defined as absolute lengths between attachment points and were normalised with respect to the mean lengths during gait.

6.2.3 Soft Tissue Artifacts

Uncorrelated normal error functions were assigned to each skin marker coordinate, accounting for STA. Two distinct SD were adopted for each error function relating to different STA magnitudes: a) SD 4 mm for skin markers on thigh and SD 3 mm for all other markers; b) SD 9 mm for thigh and SD 6 mm for all other skin markers respectively. The SD of 4 mm led to a maximum deviation from the reference skin marker position of about ± 10 mm for thigh markers, which corresponded to STA magnitudes quantified by Cappozzo et al. (1996). The SD of 9 mm for thigh and 6 mm for all other markers were similar to the values previously reported in Stagni et al. (2005).

6.2.4 Error Propagation Analysis

In 3D gait analysis, numerical methods using a Monte-Carlo type approach have most often been used to analyse the error propagation from kinematic data to segmental and joint kinematics. Thereby, multiple random sets of input data have been generated, and the distribution of the resulting outputs have been analysed (Cheze, 2000; Ramakrishnan & Kadaba, 1991). However, an analytical error analysis can be performed if a differentiable function is defined which describes the output variable with respect to the input parameters. The advantage of an analytical approach is that the error propagation is not computed for a finite number of perturbed input data but for any value of error.

In the present study, the error propagation analysis was divided into several steps to allow for an analytically tractable formulation. A flowchart of the individual steps is given in Figure 6.2. For each step, a differentiable function was defined $f(\mathbf{x}_1, \mathbf{x}_2, \dots, \mathbf{x}_N)$. Assuming independent and normally distributed input variables $\mathbf{x}_1, \mathbf{x}_2, \dots, \mathbf{x}_N$ with given SD of $\Delta\mathbf{x}_1, \Delta\mathbf{x}_2, \dots, \Delta\mathbf{x}_N$ around the reference values, the error Δf in the dependent variable was derived from the Addition in Quadrature that is

$$\Delta f = \sqrt{\sum_{i=1}^N \left(\frac{\partial f}{\partial x_i} \Delta x_i \right)^2} \quad , \quad (6.1)$$

whereby the partial derivatives were evaluated at the reference values (Taylor, 1982).

According to Equation 6.1, the errors $\Delta\mathbf{f}_i$ in the unit vectors \mathbf{f}_i of an anatomical coordinate system derived from the position data of skin markers \mathbf{p}_i as

$$\begin{aligned} \mathbf{f}_1 &= \frac{1}{|\mathbf{p}_1 - \mathbf{p}_2|} (\mathbf{p}_1 - \mathbf{p}_2) \\ \mathbf{f}_2 &= \frac{1}{|\mathbf{p}_3 - \mathbf{p}_2|} (\mathbf{p}_3 - \mathbf{p}_2) \\ \mathbf{f}_3 &= \mathbf{f}_1 \times \mathbf{f}_2 \end{aligned} \quad (6.2)$$

were computed from

$$\Delta\mathbf{f}_1 = \sqrt{\left(\frac{\partial \mathbf{f}_1}{\partial \mathbf{p}_1} \Delta\mathbf{p}_1 \right)^2 + \left(\frac{\partial \mathbf{f}_1}{\partial \mathbf{p}_2} \Delta\mathbf{p}_2 \right)^2} \quad (6.3)$$

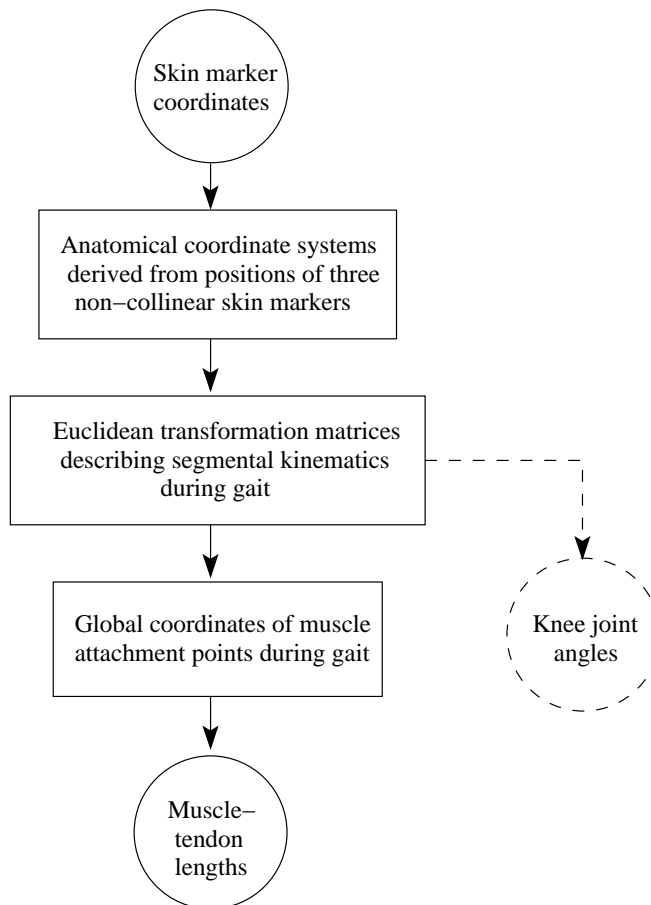


Figure 6.2: Flowchart of the individual steps for the analytical calculation of error propagation from skin marker coordinates to muscle-tendon lengths. The errors in the knee joint angles were additionally computed and compared with the literature to evaluate the analytical formulation.

$$\begin{aligned}\Delta \mathbf{f}_2 &= \sqrt{\left(\frac{\partial \mathbf{f}_2}{\partial \mathbf{p}_3} \Delta \mathbf{p}_3\right)^2 + \left(\frac{\partial \mathbf{f}_2}{\partial \mathbf{p}_2} \Delta \mathbf{p}_2\right)^2} \\ \Delta \mathbf{f}_3 &= \sqrt{\left(\frac{\partial \mathbf{f}_3}{\partial \mathbf{f}_1} \Delta \mathbf{f}_1\right)^2 + \left(\frac{\partial \mathbf{f}_3}{\partial \mathbf{f}_2} \Delta \mathbf{f}_2\right)^2}\end{aligned}$$

whereby $\Delta \mathbf{p}_i$ accounts for STA.

Given Equation 6.3, the errors $\Delta \mathbf{R}$ and $\Delta \mathbf{t}$ that propagated from an anatomical coordinate system $\mathbf{F} : [\mathbf{f}_1 \ \mathbf{f}_2 \ \mathbf{f}_3]$ to the rotation matrix \mathbf{R} , Eq. 3.16, and translation vector \mathbf{t} , Eq. 3.17, were derived as

$$\begin{aligned}\Delta \mathbf{R} &= \sqrt{\left(\frac{\partial \mathbf{R}}{\partial \mathbf{F}} \Delta \mathbf{F}\right)^2} \\ \Delta \mathbf{t} &= \sqrt{\left(\frac{\partial \mathbf{t}}{\partial \mathbf{R}} \Delta \mathbf{R}\right)^2 + \left(\frac{\partial \mathbf{t}}{\partial \mathbf{p}} \Delta \mathbf{p}\right)^2}\end{aligned}\tag{6.4}$$

whereby \mathbf{p} denotes the origin of the anatomical coordinate system $\mathbf{F} : [\mathbf{f}_1 \ \mathbf{f}_2 \ \mathbf{f}_3]$.

Given Equation 6.4, the error $\Delta \mathbf{m}_i^g$ that propagated to the global coordinates of the muscle attachment point \mathbf{m}_i^g was computed from

$$\Delta \mathbf{m}_i^g = \sqrt{\left(\frac{\partial \mathbf{m}_i^g}{\partial \mathbf{R}} \Delta \mathbf{R}\right)^2 + \left(\frac{\partial \mathbf{m}_i^g}{\partial \mathbf{t}} \Delta \mathbf{t}\right)^2} \quad ,\tag{6.5}$$

which resulted in the error Δl of muscle-tendon length

$$l = |\mathbf{m}_1^g - \mathbf{m}_2^g|\tag{6.6}$$

as

$$\Delta l = \sqrt{\left(\frac{\partial l}{\partial \mathbf{m}_1^g} \Delta \mathbf{m}_1^g\right)^2 + \left(\frac{\partial l}{\partial \mathbf{m}_2^g} \Delta \mathbf{m}_2^g\right)^2} \quad .\tag{6.7}$$

In order to evaluate the theoretical formulation, error propagation from STA to the knee joint angles was additionally computed and compared with previously published error magnitudes. The joint angles were defined according to Grood & Suntay (1983) as previously described in Section 3.2, Eq. 3.19. As an example, the error $\Delta \beta$ of angle β derived from

$$\cos \beta = \mathbf{f}_1 \cdot \mathbf{t}_3 \quad ,\tag{6.8}$$

was given as

$$\Delta\beta = \sqrt{\left(\frac{\partial\beta}{\partial\mathbf{f}_1}\Delta\mathbf{f}_1\right)^2 + \left(\frac{\partial\beta}{\partial\mathbf{t}_3}\Delta\mathbf{t}_3\right)^2} . \quad (6.9)$$

The error analysis was performed using the mathematical computing environment and programming language MATLAB (The MathWorks Inc., Massachusetts, USA).

6.3 Results

Both the knee joint angles and the modelled muscle-tendon lengths calculated from the reference kinematic data conform with the literature, Fig. 6.3. The analytical formulation led to estimated errors in the knee joint angles that were similar to those previously published, Table 6.1.

The higher STA magnitudes (SD 9 mm for thigh; SD 6 mm for shank) resulted in significantly higher errors in muscle-tendon lengths with gastrocnemius and soleus lengths generally more affected by STA than semimembranous lengths, Fig. 6.4. Constraining joint motion to rotation but no translation led to significantly smaller errors in muscle-tendon lengths for all muscles of both subjects with an error reduction of approximately one third of the initial magnitudes for unconstrained joint motion, Table 6.2. The error fluctuations throughout gait were generally low with the SD smaller than 10 % of the mean errors for all muscles. Only the propagated errors to gastrocnemius lengths were significantly different between the two subjects; however, the differences were small.

Table 6.1: Mean range of motion (ROM) [°] of the knee joint angles and average SD error [°] during gait propagated from STA a) SD 4 mm thigh, SD 3 mm other segments; b) SD 9 mm thigh, SD 6 mm other segments.

	ROM	STA (a)	STA (b)	literature
flexion-extension	68	1.1	2.0	8 [†] / 7.9 [*] / 2.5 [◇]
abduction-adduction	10	6.8	14.5	4 [†] / 6.6 [*] / 3.6 [◇]
int-ext rotation	17	2.9	6.5	12 [†] / 9.0 [*] / 2.9 [◇]

[†] Cappozzo et al. (1996), max absolute errors during gait (external fixators, N=7, mean age 23.3 y)

^{*} Reinschmidt et al. (1997), max absolute error during running (bone pins, N=3, mean age 25.7 y)

[◇] Benoit et al. (2006), average SD during gait (bone pins, N=8, mean age 26 y)

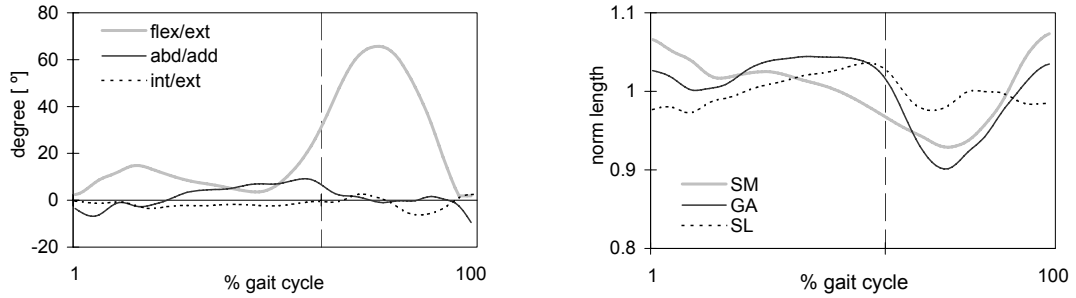


Figure 6.3: Knee joint angles (left) and normalised muscle-tendon lengths (right) for one reference trial. The angle and length changes during gait are consistent with previously published data (Arnold et al., 2006b; Delp et al., 1996; Wren et al., 2004). The vertical bar at about 60 % of the gait cycle marks the transition from stance to swing phase.

Table 6.2: Average SD % errors of the normalised muscle-tendon lengths during gait propagated from STA a) SD 4 mm thigh, SD 3 mm other segments; b) SD 9 mm thigh, SD 6 mm other segments.

		unconstrained model		constrained model	
		STA (a)	STA (b)	STA (a)	STA (b)
semimem	subject #1	9	18 [†]	6 [*]	12 ^{*,†}
	subject #2	9	19 [†]	6 [*]	12 ^{*,†}
gastrocnemius	subject #1	17	34 [†]	12 [*]	25 ^{*,†}
	subject #2	21 [◇]	43 ^{◇,†}	15 [*]	31 ^{◇,*,†}
soleus	subject #1	21	41 [†]	15 [*]	29 ^{*,†}
	subject #2	25	50 [†]	18 [*]	35 ^{*,†}

[†] Significant difference between (a) and (b) (paired Student's t-Test, $p < 0.0001$)

^{*} Significant difference between constrained and unconstrained model (paired Student's t-Test, $p < 0.0001$)

[◇] Significant difference between subjects (unpaired Student's t-Test, $p < 0.05$)

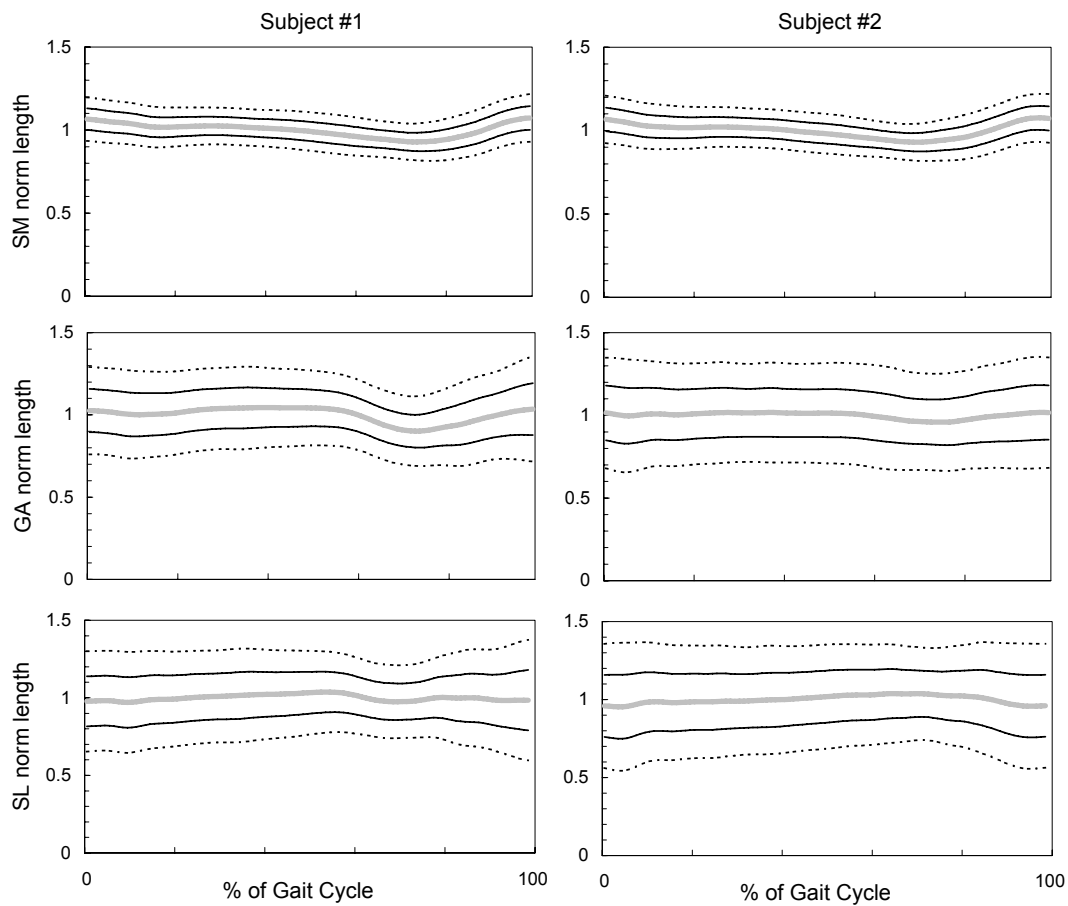


Figure 6.4: Propagated SD % errors to the normalised muscle-tendon lengths during gait for the constrained model. The errors in muscle-tendon lengths for STA a) SD 4 mm thigh, SD 3 mm other segments are plotted in black line and for b) SD 9 mm thigh, SD 6 mm other segments in dashed line respectively. The grey line depicts the normalised lengths.

6.4 Discussion

The present study introduced an analytical formulation that allowed the analysis of error propagation from STA to modelled muscle-tendon lengths. The errors in the lengths of semimembranosus, gastrocnemius, and soleus were quantified for two subjects with resulting average SD errors during gait ranging from 6 % to 50 % of normalised muscle-tendon lengths depending on the muscle, the STA magnitudes and the joint constraints. The error magnitudes in muscle-tendon lengths were considered reasonable theoretical estimates based on the realistic error values obtained for the knee joint angles.

Muscle-tendon lengths during walking have often been compared between children with CP and typically developing children, with the changes in gastrocnemius and soleus lengths throughout gait found to be between 5 % and 15 % (Wren et al., 2004; Arnold et al., 2005). Thereby, *short* has been defined as a peak normalised muscle length shorter than 2 SD of normal gait (Arnold et al., 2005; Schutte et al., 1997; Wren et al., 2004). The term *short* may need to be reconsidered given the estimated error values in normalised muscle-tendon length of the present study.

STA were assumed to be normally distributed around the reference skin marker coordinates as previously proposed to analytically estimate errors in joint kinematics (Woltring et al., 1985; Woltring, 1994). The same SD errors were assigned to the skin marker coordinates in the three spatial directions for both children subjects throughout gait. Previous studies have shown that STA vary between adult subjects, as well as during walking, with different magnitudes in the three directions (Cappozzo et al., 1996; Fuller et al., 1997; Stagni et al., 2005). The assessment of STA in children has so far been limited; thus there is the possibility of variability compared to adults due to differences in skeletal alignment and soft tissue distribution. Consequently, the small differences in error magnitudes found across the gait cycle, and between the two subjects, should be interpreted with caution.

In order to estimate the error propagation to muscle-tendon lengths, the muscles were simplified modelled as straight-line segments. Most studies in clinical gait research have used similar models to represent the muscle-tendon paths (Arnold et al., 2005, 2006b; Scheepers et al., 1997; Wren et al., 2004). A more realistic, curved path might have led to different values for absolute muscle-

tendon lengths. However, the propagated errors are unlikely to change as long as muscle-tendon lengths is derived from inverse kinematics. The substantially smaller error magnitudes obtained for the constrained musculoskeletal model suggest that additional optimisation methods such as the interval deformation technique, which has been reported to reduce errors in segmental kinematics by up to 33 % (Alexander & Andriacchi, 2001), may further decrease errors in muscle-tendon lengths.

Despite limitations, the results of the present study suggest that muscle-tendon lengths derived from kinematic data should be interpreted with caution, especially if used in the treatment decision process of children with CP. The proposed analytical method does allow the assignation of a wider range of SD to each error function, accounting for the variable error characteristics of STA in the three planes of motion across the gait cycle. Future error analysis studies should be directed towards more specifically defining STA magnitudes in each direction for children with and without CP. Furthermore, improved marker systems and new algorithms for constrained musculoskeletal models need to be developed in order to improve the accuracy of muscle-tendon lengths calculations for clinical interpretations.

7

Study IV: Interactive Visualisation of Muscle Activation During Gait

The following chapter outlines the last study, which was conducted in the scope of the present work, aiming for the interactive, web-based visualisation of the anatomically-based model of the lower limbs during walking, introduced in Chapter 5, to facilitate the teaching of gait. A prototype of the teaching tool is currently being evaluated in collaboration with the Auckland School of Physiotherapy, Auckland University of Technology, New Zealand. The results are aimed to be summarised and submitted to the journal *Human Movement Science*. The chapter is divided into (i) Introduction, (ii) Methods, (iii) Results and (iv) Discussion.

7.1 Introduction

Gait analysis is a highly visual science that requires a mastery of structure, function and spatial relationships (Sinav & Ambron, 2004). However, getting a good understanding of gait is difficult because of the complexity of human walking and because of the limited information gained from external observations. Facilitating the understanding of gait is a demanding teaching issue. Traditionally, drawings of the musculoskeletal system at different stages of the gait cycle have been used to visually assist students in the learning process; though, providing only information in two dimensions.

For the last few years, virtual reality applications, which deploy advanced 3D visualisation of medical data, have shown to be beneficial in medical education and training, in particular for teaching anatomy and physiology (Silen et al.,

2008; Sinav & Ambron, 2004). Virtual representations of internal structures and complex physiological phenomena offer new perspectives of medicine well beyond anything that can be read from books or even from dissecting cadavers, particularly in the case of dynamic processes. The Visible Human Project has thereby provided a catalyst for using anatomically-based models as basis for medical teaching (Spitzer & Whitlock, 1998a). Spitzer & Whitlock (1998a) envisioned the ideal subject for teaching human anatomy would be a computer database that appears, feels, smells, sounds, and ages like a living person.

Web-based applications offer many advantages for education purposes, including the ability to bypass physical and temporal barriers, the possibility to convey multimedia information rapidly to multiple users, the interactive user experience and the ease of information update (Chu & Chan, 1998; Sinav & Ambron, 2004). File format standards such as DICOM and X3D have supported the development of web-based tools for medical visualisation and teaching (John & Lim, 2007).

The effectiveness and the pedagogical use of web-based applications for medical education and training has been evaluated in previous studies (Silen et al., 2008; Storey et al., 2001). Questionnaires have shown that students favour web-based learning because it is convenient, accessible any time from anywhere, and supportive of learning if well designed (Storey et al., 2001). As predicted by Satava (1995), interactive, web-based teaching tools showcasing virtual representations of the human body have significantly contributed to medical education. However, the promising new media has not yet been deployed in gait analysis courses, even though it may provide a valuable addition to traditional teaching methods.

7.1.1 Aim

The aim of the present study was to develop a prototype of a web-based Graphical User Interface (GUI) for facilitating the teaching of gait to students in areas such as physiotherapy and human movement sciences. In particular, the specific muscle activation patterns at different gait events were aimed to be interactively visualised by embedding the anatomically-based model of the lower limbs during walking, introduced in Chapter 5, into a web page. The specification of the information content was done after consultation with the Auckland School of Physiotherapy, Auckland University of Technology, Auckland, New Zealand.

7.2 Method

7.2.1 Musculoskeletal Model

The gait simulation of the anatomically-based lower limb model, Fig. 5.7, built the core component of the web-based teaching tool for visualising muscle activation during walking. However, the entire simulation of one gait cycle consisted of several thousand files, which specified the configurations of the FE meshes of the bones and muscles during walking. Rendering such an extensive model within CMGUI is very time consuming, and was considered to be too slow to result in an attractive teaching tool.

Instead of embedding the entire simulation into the GUI, only the lower limb positions at eight specific events of the gait cycle were extracted. The positions comprised foot strike, loading response, mid stance, terminal stance, pre swing, toe off, mid swing, and terminal swing of the right leg. All these gait events feature unique joint motion and muscle activity patterns (Gage, 2004). The muscle structures in the right leg were coloured in each position according to their state of activation, Fig. 7.1 (supplementary movie, Appendix F.6).

7.2.2 Graphical User Interface

The purpose of any GUI is to provide a display for humans to interact with computers. As such, it should be relevant to the target user, easy to navigate, consistent in design, transparent in its functionalities, and compatible with various platforms. The present GUI was written in the interface markup language HTML, allowing for custom formatting and displaying information using the stylesheet language CSS.

The implementation of the anatomically-based model into the web-based GUI was made possible through Zinc¹. Zinc is a complex browser extension for the Mozilla platform which allows the advanced 3D visualisation modules of CMGUI to be embedded into a web page. Zinc has been released under the open source licence for the benefit of the IUPS Physiome Project. The current version

¹<http://www.cmiss.org/cmgui/zinc>

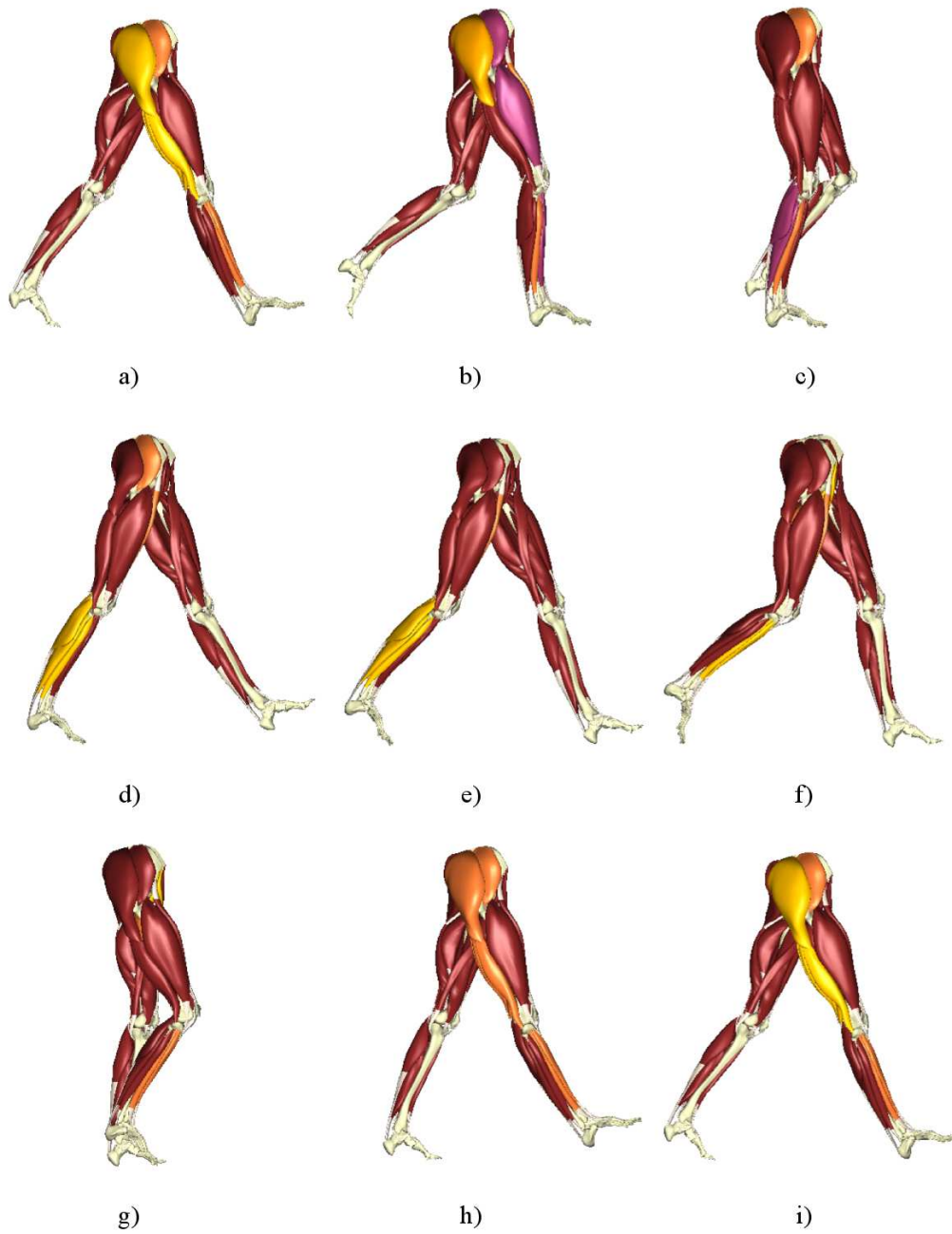


Figure 7.1: Visualisation of the muscle activity in the right leg at a) foot strike, b) loading response, c) mid stance, d) terminal stance, e) pre swing, f) toe off, g) mid swing, h) terminal swing and i) foot strike. The colour *gold* corresponds to concentric contraction, *orange* to isometric contraction, and *purple* to excentric contraction respectively (supplementary movie, Appendix F.6).

Zinc 0.6.3.4 is running on Linux and Windows, is supported for the Firefox 3.0 release and can be downloaded from the CMISS release centre² (4MB).

7.2.3 Functionalities

While the GUI design relates to the visual graphical elements on the page, interactivity design represents the functions that are called upon user input. Interactivity is a very important component of learning because it requires the active participation of users and consequently results in a deeper impression (Sinav & Ambron, 2004).

JavaScript was used for defining functions which could be called from the browser window to execute commands in the CMGUI window, and to access further background information related to individual muscle structures and gait events. The following key functions were implemented into the GUI:

- Loading the model at seven gait events with the muscles coloured according to their activity state and simultaneously providing information related to each phase.
- Highlighting individual muscles by turning off the surfaces of all other muscle structures and simultaneously providing information in terms of the specific muscle architecture, its functionality and its action during gait.
- Displaying different joint flexion-extension angles in the form of imagemaps for loading the model at particular positions during walking.
- Choosing the general point of view between frontal and lateral. Note that model rotation, translation and resizing is always possible using the mouse within the embedded CMGUI window.
- Resetting the status of the interface to the initial state with the model shown from frontal in neutral standing position.

Specific buttons, imagemaps and links were designed and embedded into the web page, which allowed users to interactively execute each function via the mouse. Screenshots of the particular elements are given in Figure 7.2.

²<http://www.cmiss.org/ReleaseCenter/zinc>

CHAPTER 7. STUDY IV: VISUALISATION OF MUSCLE ACTIVATION DURING GAIT

Table 7.1: Muscle activation patterns during gait with the type of muscle contraction indicated as I for isometric, C for concentric and E for excentric. The specific gait events are approximately given in % of the gait cycle in the following order: heel strike (0 %), loading response (10 %), mid stance (30 %), terminal stance (50 %), pre swing (55 %), toe off (60 %), mid swing (80 %) and terminal swing (100 %).

	0 %	10 %	30 %	50 %	55 %	60 %	80 %	100 %
<i>Hip flexor/extensor</i>								
iliacus	-	-	-	-	-	C	I	-
psoas	-	-	-	-	I	C	-	-
gluteus maximus	C	C	-	-	-	-	-	I
gluteus medius	I	E	I	I	I	-	-	I
adductor magnus	-	-	-	-	I	C	-	-
sartorius	-	-	-	-	-	C	C	-
<i>Quadriceps</i>								
rectus femoris	-	I	-	-	I	C	-	-
vastus lateralis	-	E	-	-	-	-	-	-
vastus medialis	-	E	-	-	-	-	-	-
vastus intermedius	-	E	-	-	-	-	-	-
<i>Hamstrings</i>								
biceps femoris	C	-	-	-	-	-	-	I
semimembranosus	C	-	-	-	-	-	-	I
semitendinosus	C	-	-	-	-	-	-	I
<i>Ankle plantar flexors</i>								
gastrocnemius	-	-	I	E	C	-	-	-
soleus	-	-	I	E	C	-	-	-
peroneus longus	-	I	I	I	C	-	-	-
tibialis posterior	I	I	I	I	C	-	-	-
<i>Ankle dorsi flexors</i>								
tibialis anterior	I	E	-	-	-	C	I	I
extensor digi long	I	E	-	-	-	C	I	I
extensor hall long	I	E	-	-	-	C	I	I

7.2.4 Validation

The evaluation by feedback from students and experienced staff is essential for developing useful and efficient tools for medical education. A questionnaire was developed to assess the usefulness and educational value of the present teaching tool in the student's learning process. The questions addressed three aspects of the GUI including its general design, the information content and the pedagogical usability. Each question could be answered on a five-graded scale with *one* corresponding to poor and *five* to excellent. Two open questions were included, asking whether the student would consider downloading Zinc for viewing the model, and whether there are any additional remarks or comments. The details of the questionnaire are given in the Appendix E.

7.3 Results

A prototype of an interactive, web-based teaching tool for gait courses was developed and will soon be introduced into a course at the School of Physiotherapy, Auckland University of Technology, New Zealand, in order to evaluate its pedagogical use to students. The GUI has been put onto the ABI main server and can be accessed online from <http://www.bioeng.auckland.ac.nz/gait>. The browser extension Zinc for the Mozilla platform needs to be downloaded to successfully load the anatomically-based lower limb model into the web page.

The prototype focuses on enhancing student's understanding of muscle activation during walking by interactively visualising the anatomically-based model of the lower limbs at eight particular gait events. The GUI was designed according to the ABI template with the elements clearly separated and accessible from one single page. Detailed explanations of the functionalities and further background information can be accessed in a special window via the help button.

A link to the online questionnaire is provided on the main page. The questionnaire can be filled out anonymously, asking only for age, gender, degree and previous experiences with computers. The feedback of users is forwarded to the authors for further analysis. Screenshots of the main page are given in Figure 7.3.

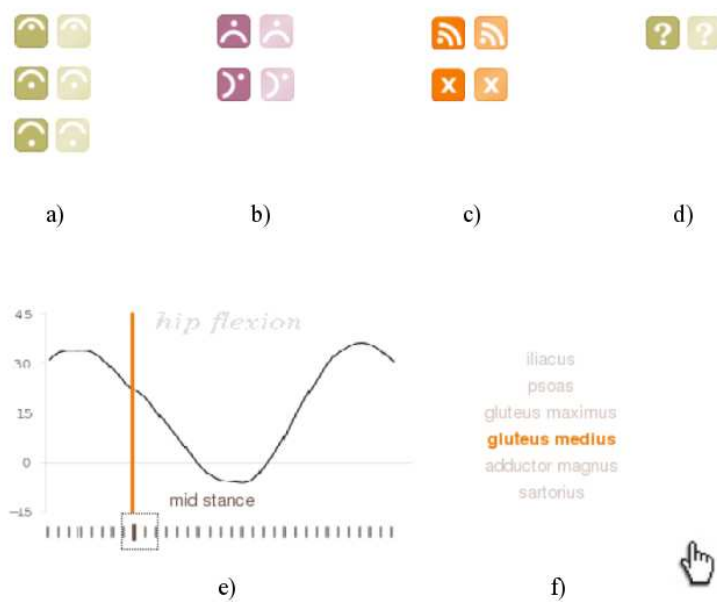


Figure 7.2: Functions are executed using the mouse on specific elements such as a) on-and-off buttons for changing the displayed joint angles, b) changing the point of view, c) resetting the status of the interface, and d) opening a help window; e) an imagemap for loading the model at different stages of the gait cycle and f) links for focusing on individual muscles.

7.4 Discussion

The anatomically-based model of the lower limbs, developed in Chapter 5, was embedded into a web page and visualised at eight specific gait events using the extension Zinc for the Mozilla platform. The interface markup language HTML was used to design a web-based GUI which allows students, teachers and the general public to load the teaching tool via the ABI web page and access information related to the muscle activation patterns during walking. Interactivity between the browser window and the CMGUI window was enabled by designing specific functions using JavaScript.

Interactive visualisation of anatomically-based models has been a promising resource in medical education (Sinav & Ambron, 2004; Spitzer & Whitlock, 1998a). However, Silen et al. (2008) showed that students did not use online teaching tools to the extent that was possible. The reasons given by students was mainly lack of time. Continuing evaluation by feedback from students and teachers is essential for successfully using the new media in medical education. At this stage, feedback from users is still collected, and no conclusions can be drawn in terms of the pedagogical usefulness of the present teaching tool.

Web-based applications can not only be accessed at any time from anywhere but they can also foster interaction between users. User-user interaction was found to be one of the most actively used features of a web site for medical education called MedWorld (Chu & Chan, 1998). Interaction between different users can be facilitated through online discussion forums and message boards. The implementation of a communication platform into the present web-based GUI would provide means to evaluate, adapt, and update the information content according to the users' demands.

The present web-based education tool is a prototype, focusing only on muscle activation during gait. Gait analysis, however, is a vast area comprising the study of anatomy, physiology, kinematics, kinetics, and different measurement techniques to name only a few. Hence, the ideal teaching tool would be a web-based platform, which facilitates further aspects of gait analysis through interactive 3D visualisation of musculoskeletal models. A rolemodel for such an online encyclopedia could be MathWorld³, which has become the most widely accessed online mathematics resource.

³<http://mathworld.wolfram.com>

CHAPTER 7. STUDY IV: VISUALISATION OF MUSCLE ACTIVATION DURING GAIT

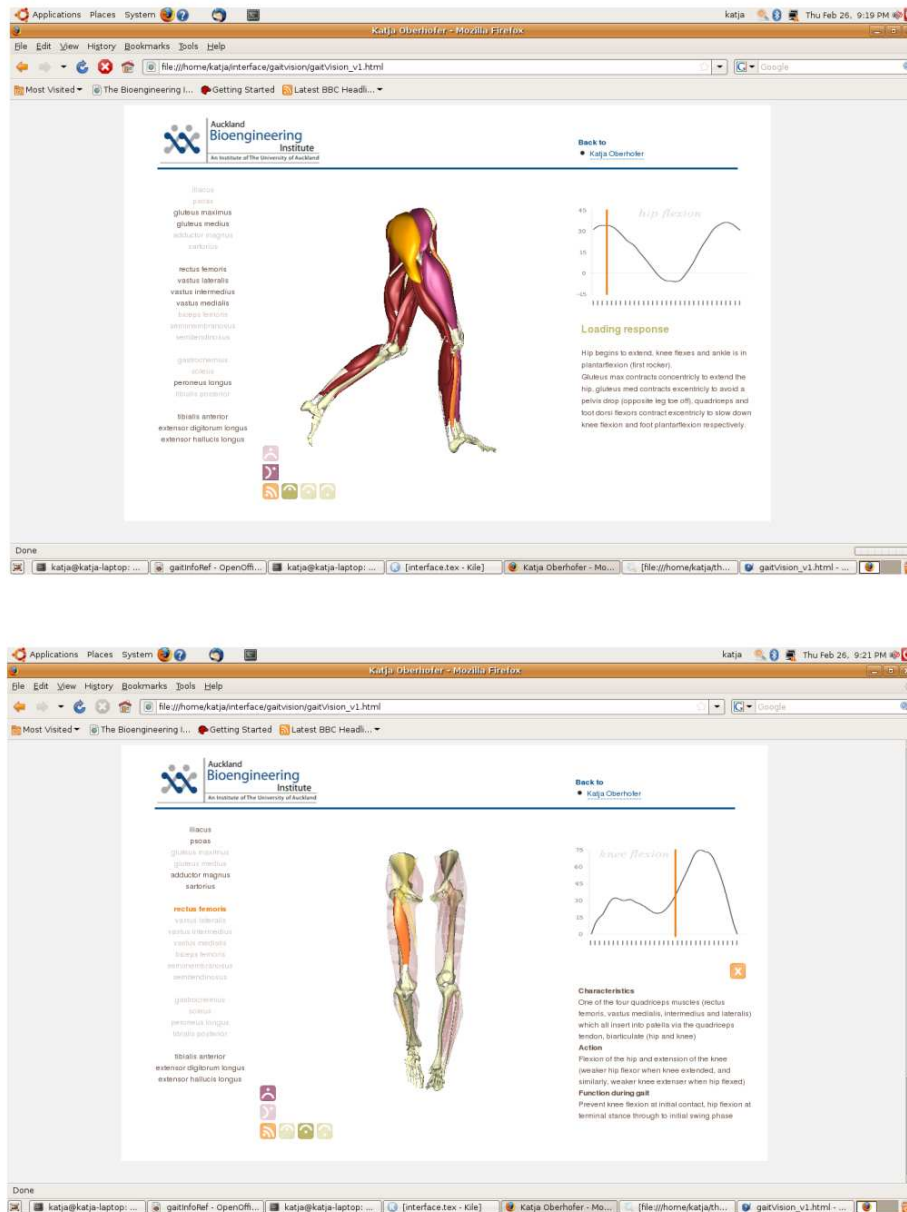


Figure 7.3: Screenshots of the web-based interface with the lower limb model shown at loading response from lateral (top), and with rectus femoris highlighted at toe off from frontal (bottom).

The current project is still at an early stage, and the usefulness of anatomically-based musculoskeletal modelling for gait courses requires further validation. Upon the results of ongoing evaluation, future work aims to extend the present prototype to include more aspects of gait and more features for facilitating learning. A well-structured, up-to-date, interactive interface, which displays essential content in an effective way through advanced 3D visualisation of the musculoskeletal system, may significantly contribute to the demanding task of teaching gait.

8

Conclusion

8.1 Summary

The objective of the present work was to explore the potential use of anatomically-based musculoskeletal models in clinical research related to CP. In particular, anatomically-based, subject-specific modelling of lower limb motion during walking was aimed to be introduced into clinical gait analysis. Three fields had to be merged in order to reach this goal that are subject-specific modelling of the musculoskeletal system, clinical gait analysis and finite deformation of muscle structures based on inverse kinematics. The theoretical background related to these three areas was outlined in Chapter 3.

The outcome of the present work was summarised in four studies in the Chapters 4 - 7. In the first study, Chap. 4, anatomically-based, subject-specific modelling techniques were adopted to investigate the volumes and lengths of lower limb muscles in children with CP (Oberhofer et al., 2009c). Subject-specific muscle models were developed based on MRI data of four children with spastic diplegia CP, two children with spastic hemiplegia CP and five age-matched children without musculoskeletal impairments. The average fitting error between the subject-specific image data and the final FE models was less than 1 mm for 120 muscle structures. Muscle lengths and muscle volumes were found to be significantly reduced in the shank and the thigh of children with CP when compared to typically developing children.

In the second study, Chap. 5, the geometric-based HMF technique was

adopted and validated for predicting soft-tissue muscle deformations in the lower limbs during walking based on kinematic data from optical motion capture (Oberhofer et al., 2009a). An anatomically-based, subject-specific lower limb model was simulated during gait by deforming 20 muscles in each leg according to the deformation of a simple skin-based host mesh. The simulation of one gait cycle was obtained in less than 20 min on a desktop with an Intel Pentium 4 processor (3.4 GHz). The validity of the HMF technique in predicting muscle deformation was demonstrated by comparing the HMF solution with MRI data in two different lower limb positions.

The third study, Chap. 6, introduced an analytical error analysis for estimating the error propagation from kinematic data to modelled muscle-tendon lengths during walking (Oberhofer et al., 2009b). Skin marker coordinates from optical motion capture were assumed to be affected by normally distributed errors which accounted for STA. Muscle-tendon lengths were simplified modelled as straight-line segments to allow for an analytically tractable formulation. The errors in modelled muscle-tendon lengths for the reference kinematic data of two subjects ranged from 6 % up to 50 % depending on the muscle, the STA magnitudes and the joint constraints adopted.

In the last study, Chap. 7, a prototype of a web-based, interactive teaching tool for gait courses was developed, particularly focusing on the visualisation of muscle activation patterns during walking. The anatomically-based model of the lower limbs during walking was embedded into a web-based GUI using the ZINC extension for the Mozilla platform. JavaScript functions were specified to load the model at certain gait events or to focus on individual muscle structures. The web page was put online onto the ABI server¹. A link to an online questionnaire is currently provided on site and will help for evaluating the usefulness of the interface to students.

8.2 Impact

Geometric features such as the physiological cross-sectional area, the pennation angle and the fibre length explain the great variation in muscle maximal forces and velocities observed within the human musculoskeletal sys-

¹<http://www.bioeng.auckland.ac.nz/gait>

tem (Lieber & Friden, 2000; Wickiewicz et al., 1983). However, measuring muscle morphology and muscle functioning in vivo is fundamentally limited. The predictions from straight-line models, used in clinical gait analysis, are not sufficient to identify the biomechanical sources of abnormal gait or to predict the consequences of treatment regimes. As a consequence, there is no agreement on the structural changes that occur in spastic muscles in children with CP (Lieber et al., 2004), and a scientific basis for determining how neuromusculoskeletal impairments contribute to abnormal gait is lacking (Gage, 2004).

Using MRI and anatomically-based modelling techniques, we demonstrated that the volumes and lengths in the thigh and the calf muscles in children with CP are significantly altered when compared to typically developing children. Our results extend previous findings which have largely been constrained to the superficial calf muscles due to limitations in ultrasound-based measurement techniques (Fry et al., 2007; Malaiya et al., 2007; Mohagheghi et al., 2008; Shortland et al., 2002). The presenting muscle atrophies suggest an overall mechanical deficit which may be related to the impaired gait patterns observed in children with CP. The library of high-order FE muscle models of children provides a significant contribution for future investigations of spastic muscles. In particular, its implementation within the mathematical modelling environment CMISS is considered a solid basis for further analysing the relationship between muscle architecture and functioning during walking.

Predicting muscle soft-tissue deformations during walking using anatomically-based musculoskeletal models is a challenging task, which has been tackled in many ways by researchers from different areas. To-date, musculoskeletal simulations have typically fallen into two categories: simulations of highly simplified models for many muscles (Chao et al., 2007; Damsgaard et al., 2006; Delp & Loan, 1995) or highly detailed models for only a few muscles and simple motor tasks (Blemker et al., 2005; Blemker & Delp, 2005; Lemos et al., 2005). To our knowledge, the anatomically-based model of the lower limbs during walking, detailed in Oberhofer et al. (2009a), is the first of its kind, allowing the realistic deformation of several muscles throughout gait with reasonable computational costs. Even though the geometric-based HMF technique does not comply with the governing equations of finite elasticity, the present framework is considered the first step towards introducing anatomically-based modelling techniques into clinical gait analysis.

Unfortunately, the accuracy in predicting physiological gait parameters does not only depend on accurate musculoskeletal models but also on error free input data. STA are considered a major error source in optical motion capture (Leardini et al., 2005), and have been shown to significantly affect the computation of segmental and joint kinematics (Cappozzo et al., 1996; Cheze, 2000; Ramakrishnan & Kadaba, 1991; Reinschmidt et al., 1997). The analytical error analysis, presented in Oberhofer et al. (2009b), demonstrated that STA also have an effect on modelled muscle-tendon lengths. Our results highlight the potential impact STA have on the biomechanical analysis of modelled muscle-tendon lengths during walking, and suggest the need for caution in the clinical interpretation of muscle-tendon lengths derived from inverse kinematics.

Anatomically-based models of the musculoskeletal system may currently not be more accurate in predicting muscle-tendon lengths during walking than simplified straight-line models, in particular if both models depend on input data from optical motion capture. However, anatomically-based models provide some significant visual insights into the spatial relationships of individual muscles during walking. Interactive visualisation of complex physiological processes has been a beneficial resource in medical education (Satava, 1995; Sinav & Ambron, 2004; Spitzer & Whitlock, 1998a). The present implementation of the anatomically-based model during walking into a web-based GUI may introduce this exciting new media to gait courses. The current teaching tool is still at an early stage, and further evaluation is required to assess its usefulness to students. However, the results of Blyth et al. (2007) have shown that anatomically-based musculoskeletal models, developed within the modelling platform CMISS, can be successfully implemented into virtual reality applications for medical education.

8.3 Limitations

The present work is a step towards applying anatomically-based, subject-specific modelling techniques to the clinical assessment of children with CP. However, accurately predict muscle functioning during walking for anatomically-based models remains a major challenge because of the non-linear material properties of muscle tissue, the high number of muscles involved in gait, the complex paths of muscles across several joints, the large deformations during gait, the interaction of individual muscles with surrounding tissue, and the limitations in current

measurement techniques for providing accurate input data. Furthermore, the application of anatomically-based models to clinical settings remains limited due to the tedious development of subject-specific models, the complexity of the resulting gait simulations, and the expertise which is required to run and analyse the models.

The development of subject-specific FE models from MRI was a very time consuming procedure because the structures of interest had to be manually digitised. Automatic image segmentation algorithms for muscle structures, such as the ones described for femur and pelvis in Shim et al. (2007), would be necessary for an extension of the current model library and more detailed investigations of spastic muscles in children with CP. Furthermore, the FE models only captured the geometric boundary surfaces. Hence, these models do not allow for studying microscopic alterations or microscopic deformations during walking. For instance, a fixed muscle shortening in children with CP can either result from a decrease in fibre lengths or from a decrease in fibre diameter (Lieber et al., 2004; Shortland et al., 2002); and the fibre lengths and pennation angles change spatially within a muscle (Blemker & Delp, 2005; Teran et al., 2005) as well as temporarily during motion (Blemker & Delp, 2006; Lieber & Friden, 2000).

The inverse kinematics simulation of the lower limb model required extensive software to be written for the calculation of segmental kinematics, the transformation of the bones within CMISS, the derivation of the control points throughout gait, the execution of the HMF subroutines and the visualisation of the resulting walking simulation. The anatomically-based model of the lower limbs during walking has a highly complex structure comprising several hundred files that specify the model in static position, numerous variables that need to be properly defined and different scripts that have to be executed in the right order. The complexity of the present lower limb model significantly limits its usefulness to other research groups or clinical settings. In addition, it was demonstrated that inverse kinematics simulation are significantly affected by errors in kinematic data from optical motion capture (Oberhofer et al., 2009b). The introduced errors into musculoskeletal models are considered a major limitation in their application to clinical gait research.

The muscle soft-tissue deformations during walking were purely derived from segmental kinematics without taking the forces into account that have caused the motion. However, successful walking is predetermined by the anisotropic, ac-

tive and passive mechanical properties of muscle tissue (Blemker & Delp, 2006; Roehrlé & Pullan, 2007). A hybrid approach, which couples the HMF solution with a constitutive model of muscle tissue such as described in Fernandez et al. (2005), would enable investigations of stresses and strains within muscles during walking. Challenges in the development of such a model would include the accurate description of the constitutive behaviour of muscle tissue and the handling of contact between muscle structures. The modelling environment CMISS would certainly provide an extremely powerful tool, allowing for the FE analysis of the muscle continuum under loading, and for the incorporation of constitutive laws that bridge spatial scales from cellular levels up to whole organs (Roehrlé & Pullan, 2007).

The validity of the HMF technique for predicting muscle deformation during walking was assessed using static MRI data in two different positions using a typical horizontal MRI unit. However, muscle deformation during walking is affected by active muscle contraction, muscle-muscle and muscle-bone interactions (Blemker & Delp, 2005). Additional external forces such as gravity further alter the muscle-tendon shape. A MRI unit, such as described in Gold et al. (2004), would be required to capture the muscle deformation under physiological weight-bearing conditions. Unfortunately, the accessibility to such a scanner was not provided in the scope of the present study. Hence, additional validation may be necessary if the anatomically-based model of the lower limbs during walking is to be used in the clinical assessment of children with CP.

8.4 Outlook

One day, subject-specific, anatomically-based models of children with CP might be developed routinely during a clinical assessment and used to identify the individual muscles which are causing the musculoskeletal impairments observed. Future models might even allow for predicting the consequences of different treatment regimes, and hence, assist in comprehensive surgical planning. Finally, the routine development of subject-specific musculoskeletal models in clinical gait analysis would lead to extensive model libraries which could be used for medical visualisation and education.

At this stage, however, the application of anatomically-based modelling techniques to clinical gait analysis is still considered visionary, requiring major re-

search outputs and advancements in modelling soft-tissue muscle deformation in the lower limbs during walking. Despite current limitations, the present work has demonstrated that anatomically-based musculoskeletal modelling provides significant new insight into spastic muscles of children with CP and offers a promising tool for more detailed investigations of muscle functioning during both normal and pathological gait.

Future work should aim to extend the library of anatomically-based lower limb models of children by improving the development of subject-specific models from MRI and further capturing microscopic features such as muscle fibre lengths and penation angles. Previous studies have introduced fitting algorithms, which facilitate the automatic development of high-order FE models from sparse medical datasets (Shim et al., 2007), and have demonstrated that the incorporation of fibre lengths and penation angles is feasible within the modelling software CMISS (Nash & Hunter, 2000; Roehrlé & Pullan, 2007). Extensive investigations of lower limb muscles in children with CP may not only provide new insights into the structural alterations that occur secondary to the neurological disorder, but may also help for the evaluation of treatment outcomes from serial castings or soft-tissue muscle surgeries. Depending on the structural alterations that present, strength training or electrical stimulation might be more valuable in preventing fixed contracture than stretching or casting (Shortland et al., 2002).

The gained insight from detailed anatomical studies of spastic muscles in children with CP may be linked to calculations of muscles forces from inverse dynamics. Muscle forces in gait analysis are commonly derived from the net joint moment and forces based on inverse dynamics using static optimisation and generic physiological muscle models (Gage, 2004; Zajac et al., 2002). However, the muscle architecture predetermines muscle functioning (Lieber & Friden, 2000). In particular, the physiological cross sectional area is related to the maximal force generating capabilities, and the fibre penation angle is related to the maximal shortening velocities of the muscle-tendon unit. Analysing the influence of subject-specific muscle architecture on muscle forces may lead to improved optimisation algorithms, and consequently, help for better identifying the causes of abnormal gait. Previous work has further demonstrated the value of using muscle forces from inverse dynamics as boundary conditions into subject-specific FE models of the skeletal system for analysing stress magnitudes and distributions in the knee joint during walking (Fernandez et al., 2007).

An extension of the web-based teaching tool for medical education may become a beneficial addition to the traditional teaching of gait. It has been demonstrated in the literature that the FE models within CMISS can be exported into computer animation software such as blender² (Blyth et al., 2007). Using blender, realistic virtual environments can be created and converted into the Virtual Reality Modeling Language (VRML) or X3D files, which are standard XML-based formats for representing 3D computer graphics interactively on the web (John & Lim, 2007). A platform-independent, freely-accessible, interactive visualisation of anatomically-based musculoskeletal models during walking could provide a valuable resource not only for gait courses, but also for patient education and the general public.

In conclusion, the field of anatomically-based modelling of the musculoskeletal system during walking is an exciting research area, with many more research questions to be answered in future work. Advancements in the field crucially depend on the collaboration between different research groups, especially if anatomically-based, subject-specific models are aimed to be applied to clinical gait analysis. For instance, improvements need to be made in medical imaging of muscles during walking, accurately deriving segmental kinematics from optical motion capture and describing the mechanical behaviour of muscle tissue. Upon successful collaboration, however, we are confident that musculoskeletal models will eventually become virtual representations of the human anatomy and physiology that not only appear, feel, smell, sound and age like humans, as envisioned by Spitzer & Whitlock (1998a), but also walk like us.

²<http://www.blender.org>



Ethical Approval Letter


 Health and Disability Ethics Committees	Northern Y Regional Ethics Committee Ministry of Health 3 rd Floor, BNZ Building 354 Victoria Street PO Box 1031 Hamilton Phone (07) 858 7021 Fax (07) 858 7070
8 September 2006	
Ms Katja Oberhofer The Bioengineering Institute Faculty of Engineering University of Auckland Private bag 92019, Auckland.	
Dear Katja	
MRI-Based Patient-Specific Musculoskeletal Modeling For Computation Of Lower Limb Muscle Lengths During Walking In Children With Cerebral Palsy. Investigators: Ms Katja Oberhofer, A/Prof Susan Stott, Ms Sharon Walt Locations: Auckland DHB, Gait Laboratory in University of Auckland. Ethics Ref: NTY/06/07/064	
The above study has been given ethical approval by the Northern Y Regional Ethics Committee.	
Approved Documents Information sheet for parents or guardians of children who have cerebral palsy, version 3 dated 16/08/2006. Information sheet for parents or guardians of control children, version 3 dated 16/08/2006. Advertisement – Children participants wanted for research in musculoskeletal modelling. Information Sheet for children with cerebral palsy version 2 dated 16/08/2006. Information Sheet for children with cerebral palsy version 2 dated 16/08/2006. Consent Form.- MRI-based musculoskeletal modelling of lower limbs.	

Figure A.1: Approval letter from the NZ Northern Y Regional Ethics Committee, page 1a.

APPENDIX A. ETHICAL APPROVAL LETTER

<p>Certification The Committee is satisfied that this study is not being conducted principally for the benefit of the manufacturer or distributor of the medicine or item in respect of which the trial is being carried out.</p> <p>Accreditation The Committee involved in the approval of this study is accredited by the Health Research Council and is constituted and operates in accordance with the Operational Standard for Ethics Committees, March 2002.</p> <p>Progress Reports The study is approved until 1 February 2009. The Committee will review the approved application annually and notify the Primary Investigator if it withdraws approval. It is the Primary Investigator's responsibility to forward a progress report covering all sites prior to ethical review of the project in 8 September 2007. The report form is available on http://www.newhealth.govt.nz/ethicscommittees. Please note that failure to provide a progress report may result in the withdrawal of ethical approval. A final report is also required at the conclusion of the study.</p>
<hr/> <p>Administered by the Ministry of Health Approved by the Health Research Council http://www.newhealth.govt.nz/ethicscommittees</p>

Figure A.2: Approval letter from the NZ Northern Y Regional Ethics Committee, page 1b.


 <p>Health and Disability Ethics Committees</p>	<p>Northern Y Regional Ethics Committee Ministry of Health 3rd Floor, BNZ Building 354 Victoria Street PO Box 1031 Hamilton Phone (07) 858 7021 Fax (07) 858 7070</p>
<p>Requirements for SAE Reporting The Primary Investigator will inform the Committee as soon as possible of the following:</p> <ul style="list-style-type: none">• Any related study in another country that has stopped due to serious or unexpected adverse events• withdrawal from the market for any reason• all serious adverse events occurring during the study in New Zealand which result in the investigator or sponsor breaking the blinding code at the time of the SAE or which result in hospitalisation or death.• all serious adverse events occurring during the study worldwide which are considered related to the study medicine. <p>All SAE reports must be signed by the Primary Investigator and include a comment on whether he/she considers there are any ethical issues relating to this study continuing due to this adverse event. If the adverse event is local and does not have the sponsor's report attached, an opinion on whether the event is thought to be related to the study should be given along with any other pertinent information. It is assumed by signing the report, the primary investigator has undertaken to ensure that all New Zealand investigators are made aware of the event.</p>	

Figure A.3: Approval letter from the NZ Northern Y Regional Ethics Committee, page 2a.

Amendments

All amendments to the study must be advised to the Committee prior to their implementation, except in the case where immediate implementation is required for reasons of safety. In such cases the Committee must be notified as soon as possible of the change.

Please quote the above ethics committee reference number in all correspondence.

The Primary Investigator is responsible for advising any other study sites of approvals and all other correspondence with the Ethics Committee.

It should be noted that Ethics Committee approval does not imply any resource commitment or administrative facilitation by any healthcare provider within whose facility the research is to be carried out. Where applicable, authority for this must be obtained separately from the appropriate manager within the organisation.

Yours sincerely



Amrita Kuruvilla
Northern Y Ethics Committee Administrator
Email: amrita_kuruvilla@moh.govt.nz

Figure A.4: Approval letter from the NZ Northern Y Regional Ethics Committee, page 2b.

B

Updating Nodal Derivatives after HMF

If a bicubic-linear FE mesh (slave mesh) is customised to subject-specific data using the HMF technique, not only the position \mathbf{u} of every node but also the nodal derivatives with respect to the slave mesh element coordinates $\eta \in [0, 1]$ need to be updated according to the deformed host mesh configuration.

As the slave mesh is completely embedded into the host, its nodal derivatives can be written as functions of host mesh element coordinates $\xi \in [0, 1]$ that is

$$\begin{aligned}\frac{\partial \mathbf{u}}{\partial \eta_1} &= \frac{\partial \mathbf{u}}{\partial \xi_1} \frac{\partial \xi_1}{\partial \eta_1} + \frac{\partial \mathbf{u}}{\partial \xi_2} \frac{\partial \xi_2}{\partial \eta_1} + \frac{\partial \mathbf{u}}{\partial \xi_3} \frac{\partial \xi_3}{\partial \eta_1} \\ \frac{\partial \mathbf{u}}{\partial \eta_2} &= \frac{\partial \mathbf{u}}{\partial \xi_1} \frac{\partial \xi_1}{\partial \eta_2} + \frac{\partial \mathbf{u}}{\partial \xi_2} \frac{\partial \xi_2}{\partial \eta_2} + \frac{\partial \mathbf{u}}{\partial \xi_3} \frac{\partial \xi_3}{\partial \eta_2}\end{aligned}\tag{B.1}$$

which can be expressed in matrix form, for example for Equation B.1, as

$$\begin{bmatrix} \frac{\partial u_1}{\partial \xi_1} & \frac{\partial u_1}{\partial \xi_2} & \frac{\partial u_1}{\partial \xi_3} \\ \frac{\partial u_2}{\partial \xi_1} & \frac{\partial u_2}{\partial \xi_2} & \frac{\partial u_2}{\partial \xi_3} \\ \frac{\partial u_3}{\partial \xi_1} & \frac{\partial u_3}{\partial \xi_2} & \frac{\partial u_3}{\partial \xi_3} \end{bmatrix} \begin{bmatrix} \frac{\partial \xi_1}{\partial \eta_1} \\ \frac{\partial \xi_2}{\partial \eta_1} \\ \frac{\partial \xi_3}{\partial \eta_1} \end{bmatrix} = \begin{bmatrix} \frac{\partial u_1}{\partial \eta_1} \\ \frac{\partial u_2}{\partial \eta_1} \\ \frac{\partial u_3}{\partial \eta_1} \end{bmatrix}.\tag{B.2}$$

The second term on the left hand side in Equation B.2 remains constant during the HMF procedure. Hence, the nodal derivatives in deformed state can be derived from Equation B.3.

$$\left(\frac{\partial \mathbf{u}}{\partial \eta}\right)_{\text{def}} = \left[\frac{\partial \mathbf{u}}{\partial \xi}\right]_{\text{def}} \times \left[\frac{\partial \mathbf{u}}{\partial \xi}\right]_{\text{in}}^{-1} \cdot \left(\frac{\partial \mathbf{u}}{\partial \eta}\right)_{\text{in}}\tag{B.3}$$

The cross derivatives are obtained in a similar fashion though mathematically more involved. Differentiating Equation B.1 for the first global coordinate u_1

APPENDIX B. UPDATING NODAL DERIVATIVES

with respect to η_2 gives

$$\begin{aligned} \frac{\partial^2 u_1}{\partial \eta_1 \partial \eta_2} &= \frac{\partial u_1}{\partial \xi_1} \frac{\partial^2 \xi_1}{\partial \eta_1 \partial \eta_2} + \frac{\partial \xi_1}{\partial \eta_1} \frac{\partial^2 u_1}{\partial \xi_1 \partial \eta_2} + \frac{\partial u_1}{\partial \xi_2} \frac{\partial^2 \xi_2}{\partial \eta_1 \partial \eta_2} \\ &+ \frac{\partial \xi_2}{\partial \eta_1} \frac{\partial^2 u_1}{\partial \xi_2 \partial \eta_2} + \frac{\partial u_1}{\partial \xi_3} \frac{\partial^2 \xi_3}{\partial \eta_1 \partial \eta_2} + \frac{\partial \xi_3}{\partial \eta_1} \frac{\partial^2 u_1}{\partial \xi_3 \partial \eta_2} \end{aligned} \quad (\text{B.4})$$

Rearranging Equation B.4 leads in

$$\begin{bmatrix} \frac{\partial u_1}{\partial \xi_1} \\ \frac{\partial u_1}{\partial \xi_2} \\ \frac{\partial u_1}{\partial \xi_3} \end{bmatrix}^T \begin{bmatrix} \frac{\partial^2 \xi_1}{\partial \eta_1 \partial \eta_2} \\ \frac{\partial^2 \xi_2}{\partial \eta_1 \partial \eta_2} \\ \frac{\partial^2 \xi_3}{\partial \eta_1 \partial \eta_2} \end{bmatrix} = \frac{\partial^2 u_1}{\partial \eta_1 \partial \eta_2} - \frac{\partial \xi_1}{\partial \eta_1} \frac{\partial^2 u_1}{\partial \xi_1 \partial \eta_2} - \frac{\partial \xi_2}{\partial \eta_1} \frac{\partial^2 u_1}{\partial \xi_2 \partial \eta_2} - \frac{\partial \xi_3}{\partial \eta_1} \frac{\partial^2 u_1}{\partial \xi_3 \partial \eta_2} \quad (\text{B.5})$$

which is solved for the second term on the left hand side. To do so, the mixed derivatives on the right hand side need further manipulation using the chain rule

$$\begin{aligned} \frac{\partial^2 u_1}{\partial \xi_1 \partial \eta_2} &= \frac{\partial^2 u_1}{\partial \xi_1^2} \frac{\partial \xi_1}{\partial \eta_2} + \frac{\partial^2 u_1}{\partial \xi_1 \xi_2} \frac{\partial \xi_2}{\partial \eta_2} + \frac{\partial^2 u_1}{\partial \xi_1 \xi_3} \frac{\partial \xi_3}{\partial \eta_2} \\ \frac{\partial^2 u_1}{\partial \xi_2 \partial \eta_2} &= \frac{\partial^2 u_1}{\partial \xi_1 \partial \xi_2} \frac{\partial \xi_1}{\partial \eta_2} + \frac{\partial^2 u_1}{\partial \xi_2^2} \frac{\partial \xi_2}{\partial \eta_2} + \frac{\partial^2 u_1}{\partial \xi_2 \partial \xi_3} \frac{\partial \xi_3}{\partial \eta_2} \\ \frac{\partial^2 u_1}{\partial \xi_3 \partial \eta_2} &= \frac{\partial^2 u_1}{\partial \xi_1 \partial \xi_3} \frac{\partial \xi_1}{\partial \eta_2} + \frac{\partial^2 u_1}{\partial \xi_2 \partial \xi_3} \frac{\partial \xi_2}{\partial \eta_2} + \frac{\partial^2 u_1}{\partial \xi_3^2} \frac{\partial \xi_3}{\partial \eta_2} \end{aligned} \quad (\text{B.6})$$

All terms on the right hand side in Equation B.6 are known, provided that the first derivatives were computed first. Hence, the new expressions for the mixed derivatives in Equation B.6 can be substituted back into Equation B.5.

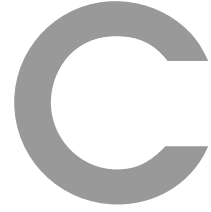
Similar expressions are obtained for the cross derivatives of the second and third global coordinates u_1, u_2 , resulting in a system of linear equations of the form

$$\begin{bmatrix} \partial(u_1, u_2, u_3) \\ \partial(\xi_1, \xi_2, \xi_3) \end{bmatrix}_{in} \begin{bmatrix} \frac{\partial^2 \xi_1}{\partial \eta_1 \partial \eta_2} \\ \frac{\partial^2 \xi_2}{\partial \eta_1 \partial \eta_2} \\ \frac{\partial^2 \xi_3}{\partial \eta_1 \partial \eta_2} \end{bmatrix} = \mathbf{q} \quad (\text{B.7})$$

with vector \mathbf{q} given as

$$\mathbf{q} = \begin{bmatrix} \frac{\partial^2 u_1}{\partial \eta_1 \partial \eta_2} - \frac{\partial \xi_1}{\partial \eta_1} \frac{\partial^2 u_1}{\partial \xi_1 \partial \eta_2} - \frac{\partial \xi_2}{\partial \eta_1} \frac{\partial^2 u_1}{\partial \xi_2 \partial \eta_2} - \frac{\partial \xi_3}{\partial \eta_1} \frac{\partial^2 u_1}{\partial \xi_3 \partial \eta_2} \\ \frac{\partial^2 u_2}{\partial \eta_1 \partial \eta_2} - \frac{\partial \xi_1}{\partial \eta_1} \frac{\partial^2 u_2}{\partial \xi_1 \partial \eta_2} - \frac{\partial \xi_2}{\partial \eta_1} \frac{\partial^2 u_2}{\partial \xi_2 \partial \eta_2} - \frac{\partial \xi_3}{\partial \eta_1} \frac{\partial^2 u_2}{\partial \xi_3 \partial \eta_2} \\ \frac{\partial^2 u_3}{\partial \eta_1 \partial \eta_2} - \frac{\partial \xi_1}{\partial \eta_1} \frac{\partial^2 u_3}{\partial \xi_1 \partial \eta_2} - \frac{\partial \xi_2}{\partial \eta_1} \frac{\partial^2 u_3}{\partial \xi_2 \partial \eta_2} - \frac{\partial \xi_3}{\partial \eta_1} \frac{\partial^2 u_3}{\partial \xi_3 \partial \eta_2} \end{bmatrix}. \quad (\text{B.8})$$

The first term in Equation B.7, which is the Jacobian matrix of the undeformed host, is invertible, and allows the expression to be solved for the cross derivatives.



Singular Value Decomposition

Challis (1995) demonstrated that a least-squares formulation for minimising STA from optical motion capture can be reformulated into a maximisation problem and solved using singular value decomposition. The corresponding numerical method to determine the best approximation of segmental kinematics based on a redundant number of skin markers is outlined below.

Initially, the affine transformation matrix \mathbf{T} , including rotation, shearing and scaling is computed by minimising the objective function \mathcal{S}

$$\mathcal{S}_{min} = \sum_{d=1}^D [(\mathbf{p}_{d,t+1} - \mathbf{T}\mathbf{p}_{d,t})^T (\mathbf{p}_{d,t+1} - \mathbf{T}\mathbf{p}_{d,t})] \quad , \quad (\text{C.1})$$

where \mathbf{p} is the 3D position of skin marker d of the cluster D in time frame t and $t + 1$ respectively. The best Euclidean transformation for the cluster of markers is then determined by minimising the difference between the unknown rotation matrix \mathbf{R} with entries r_{ij} and the upper left 3×3 entries t_{ij} of the affine transformation matrix \mathbf{T} as

$$\mathcal{S}_{min} = \sum_{i=1}^3 \sum_{j=1}^3 (t_{ij} - r_{ij})^2 \quad . \quad (\text{C.2})$$

Equation C.2 can be reformulated in

$$\mathcal{S}_{min} = \text{tr}(\mathbf{R}^T \mathbf{R}) - 2\text{tr}(\mathbf{R}^T \mathbf{T}) \quad , \quad (\text{C.3})$$

where $\text{tr}(\mathbf{X})$ is the trace of a given matrix \mathbf{X} .

APPENDIX C. SINGULAR VALUE DECOMPOSITION

The rotation matrix \mathbf{R} has to comply with the properties of an orthogonal matrix that is

$$\mathbf{R}\mathbf{R}^T = \mathbf{R}^T\mathbf{R} = \mathbf{R}^{-1}\mathbf{R} = \mathbf{I} \quad , \quad \det(\mathbf{R}) = 1 \quad (\text{C.4})$$

With \mathbf{R} subject to Equation C.4, the minimising problem in Equation C.3 can be written as a maximising problem as

$$\mathcal{S}_{max} = \text{tr}(\mathbf{R}^T\mathbf{T}) \quad . \quad (\text{C.5})$$

Equation C.5 can be solved by performing a singular value decomposition on \mathbf{T} . Singular value decomposition is based on the theorem that every real matrix \mathbf{A} can be factorised such that $\mathbf{A} = \mathbf{U}\mathbf{S}\mathbf{V}^T$, where \mathbf{U} and \mathbf{V} are orthogonal matrices and \mathbf{S} is a diagonal matrix with non-negative entries s_i , which are known as singular values (Nipp & Stoffer, 2002).

The singular value decomposition on \mathbf{T} gives

$$\mathbf{T} = \mathbf{U}\mathbf{S}\mathbf{V}^T \quad . \quad (\text{C.6})$$

Substituting Equation C.6 into Equation C.5 and reformulating the expression leads in

$$\mathcal{S}_{max} = \text{tr}(\mathbf{W}\mathbf{S}) \quad (\text{C.7})$$

with $\mathbf{W} = \mathbf{V}^T\mathbf{R}^T\mathbf{U}$. Since \mathbf{V} , \mathbf{R} and \mathbf{U} are orthogonal, \mathbf{W} must also be orthogonal, and is therefore subject to $|\mathbf{W}| \leq 1$ as implied in Equation C.4.

Thus, Equation C.7 is maximised if $\mathbf{W} = \mathbf{I}$, and therefore

$$\mathbf{R} = \mathbf{U}\mathbf{V}^T \quad . \quad (\text{C.8})$$

For certain cases, however, Equation C.8 does lead in a reflection matrix ($\det(\mathbf{R}) = -1$) rather than a rotation matrix. A modification, given in Equation C.9, was further proposed by Challis (1995) to account for these cases.

$$\mathbf{R} = \mathbf{U} \begin{bmatrix} 1 & 0 & 0 \\ 0 & 1 & 0 \\ 0 & 0 & \det(\mathbf{U}\mathbf{V}^T) \end{bmatrix} \mathbf{V}^T \quad (\text{C.9})$$

D

Lower Limb Mesh Parameters

Table D.1: Bone mesh parameters of the lower limb model described in Chapter 5, including the number of landmark and target points used for the HMF customisation of the generic model from the ABI library to the subject-specific data from MRI.

	Nodes	Elements	landmark/targets
hip	224	84	40
femur	829	832	60
patella †	47	48	8
tibia	178	170	42
fibula	122	112	32
foot †	1705	1567	12

† The subject-specific mesh was developed using the Direct Least-Squares Method, described in Section 3.3, instead of the HMF technique.

APPENDIX D. LOWER LIMB MESH PARAMETERS

Table D.2: Muscle mesh parameters of the lower limb model described in Chapter 5, including the number of control points which were used as kinematic constraints for the walking simulation.

	Mesh		Control Points			
	Nodes	Elements	Foot	Shank	Thigh	Hip
adductor magnus	56	24	-	-	8	4
biceps femoris	72	32	-	5	5	4
extensor digi long	32	14	5	7	-	-
extensor hall long	32	14	5	7	-	-
gastrocnemius	63	26	5	5	9	-
gluteus maximus	56	24	-	-	6	6
gluteus medius	48	20	-	-	6	6
iliacus	28	12	-	-	6	6
peroneus longus	40	18	5	7	-	-
psoas	24	10	-	-	6	6
rectus femoris	36	16	-	6	9	5
sartorius	40	18	-	5	3	6
semimembranosus	28	12	-	5	5	4
semitendinosus	32	14	-	5	5	4
soleus	56	24	5	7	-	-
tibialis anterior	28	12	5	7	-	-
tibialis posterior	32	14	5	7	-	-
vastus lateralis	64	28	-	6	9	-
vastus medialis	32	14	-	6	9	-
vastus intermedius	28	12	-	6	9	-
Total	943	358	35	91	95	51

E

Questionnaire Graphical User Interface

A questionnaire was developed to assess the usefulness and educational value of the web-based teaching tool, described in Chapter 7. A link to the online questionnaire is provided on the main page of the GUI.

The following questions are included in the questionnaire:

Table E.1: General layout with *one* the poorest and *five* the best grade.

General	1	2	3	4	5
Design	<input type="radio"/>	<input type="radio"/>	<input type="radio"/>	<input type="radio"/>	<input type="radio"/>
Organisation of content	<input type="radio"/>	<input type="radio"/>	<input type="radio"/>	<input type="radio"/>	<input type="radio"/>
Transparency of functionalities	<input type="radio"/>	<input type="radio"/>	<input type="radio"/>	<input type="radio"/>	<input type="radio"/>
Other:	<input type="radio"/>	<input type="radio"/>	<input type="radio"/>	<input type="radio"/>	<input type="radio"/>

Table E.2: Content of information with *one* the poorest and *five* the best grade.

Informational content	1	2	3	4	5
Relevant	<input type="radio"/>	<input type="radio"/>	<input type="radio"/>	<input type="radio"/>	<input type="radio"/>
Accurate	<input type="radio"/>	<input type="radio"/>	<input type="radio"/>	<input type="radio"/>	<input type="radio"/>
Coverage	<input type="radio"/>	<input type="radio"/>	<input type="radio"/>	<input type="radio"/>	<input type="radio"/>
Other:	<input type="radio"/>	<input type="radio"/>	<input type="radio"/>	<input type="radio"/>	<input type="radio"/>

APPENDIX E. QUESTIONNAIRE GUI

Table E.3: Pedagogical usability with *one* the poorest and *five* the best grade.

Pedagogical usability	1	2	3	4	5
Enhanced your learning	<input type="radio"/>	<input type="radio"/>	<input type="radio"/>	<input type="radio"/>	<input type="radio"/>
Added value to the course	<input type="radio"/>	<input type="radio"/>	<input type="radio"/>	<input type="radio"/>	<input type="radio"/>
Would recommend to others	<input type="radio"/>	<input type="radio"/>	<input type="radio"/>	<input type="radio"/>	<input type="radio"/>
Other:	<input type="radio"/>	<input type="radio"/>	<input type="radio"/>	<input type="radio"/>	<input type="radio"/>

The following open questions are further asked:

- Would you consider downloading and installing the ZINC plugin (4MB) which is required to view the 3D model? If no, please give a reason why not.
- Do you have additional remarks or comments related to the interface?

F

Supplementary Movies

The following movies can be viewed either on the supplementary CD, which is attached to the back of this thesis, or online at <http://www.bioeng.auckland.ac.nz/gait>. All the movies were developed based on a series of static images from the dynamic simulations of the musculoskeletal models within CMGUI.

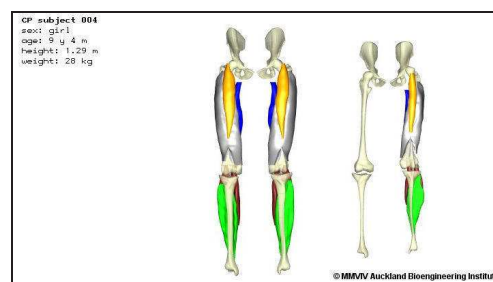


Figure F.1: *StaticChildrenModel.wmv* showing the subject-specific, anatomically-based models of one child without CP (subject 005, Table 4.1) and one child with CP (subject 006, Table 4.2) outlined in Chapter 4.



Figure F.2: *StaticLowerLimbs.wmv* showing the static model of the lower limbs, presented in Chapter 5, including the control points and the skin-based host mesh.

APPENDIX F. SUPPLEMENTARY MOVIES

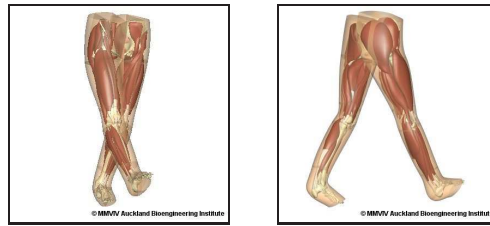


Figure F.3: *GaitHost.wmv* showing the gait simulation of the anatomically-based lower limb model, outlined in Chapter 5, including the resulting deformation of the skin-based host mesh.

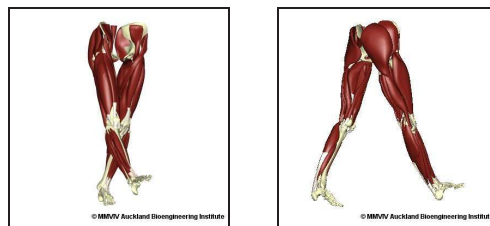


Figure F.4: *Gait.wmv* showing the gait simulation of the anatomically-based lower limb model, described in Chapter 5.

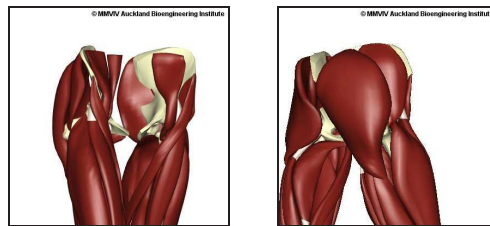


Figure F.5: *GaitPelvis.wmv* showing a close-up view of the pelvis of the anatomically-based lower limb model during gait, presented in Chapter 5

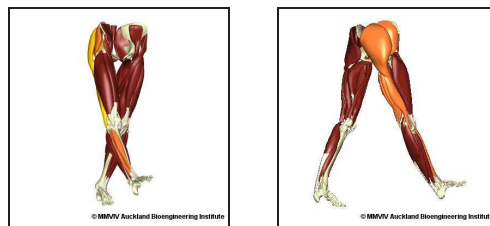


Figure F.6: *GaitMuscleActivation.wmv* showing the visualisation of the muscle activation during walking for the web-based teaching tool introduced in Chapter 7. The colour *gold* corresponds to concentric contraction, *orange* to isometric contraction, and *purple* to excentric contraction respectively.

Bibliography

- Alexander, E. J., & Andriacchi, T. P. (2001). Correcting for deformation in skin-based marker systems. *Journal of Biomechanics*, *34*, 355–361.
- Allard, P., Stokes, I. A. F., & Bianchi, J.-P. (Eds.) (1995). *Three-Dimensional Analysis of Human Movement*. Human Kinetics.
- Altmann, S. L. (1986). *Rotations, Quaternions, and Double Groups*. Clarendon Press, Oxford.
- Anderson, F. C., & Pandy, M. G. (2001). Dynamic optimization of human walking. *Journal of Biomechanical Engineering*, *123*, 381–390.
- Andriacchi, T. P., & Alexander, E. J. (2000). Studies of human locomotion: past, present and future. *Journal of Biomechanics*, *33*, 1217–1224.
- Andriacchi, T. P., Alexander, E. J., & Toney, M. K. (1998). A point cluster method for in vivo motion analysis: Applied to a study of knee kinematics. *Journal of Biomechanical Engineering*, *120*, 743–749. PCM versus SVD.
- Arnold, A. S., Anderson, F. C., Pandy, M. G., & Delp, S. L. (2005). Muscular contributions to hip and knee extension during the single limb stance phase of normal gait: a framework for investigating the causes of crouch gait. *Journal of Biomechanics*, *38*, 2181–2189.
- Arnold, A. S., Blemker, S. S., & Delp, S. L. (2001). Evaluation of a deformable musculoskeletal model for estimating muscle-tendon lengths during crouch gait. *Annals of Biomedical Engineering*, *29*, 263–274.
- Arnold, A. S., Liu, M. Q., Schwartz, M. H., Ounpuu, S., & Delp, S. L. (2006a). The role of estimating muscle-tendon lengths and velocities of the hamstrings in the evaluation and treatment of crouch gait. *Gait and Posture*, *23*, 273–281.
- Arnold, A. S., Liu, M. Q., Schwartz, M. H., Ounpuu, S., Dias, L. S., & Delp, S. L. (2006b). Do the hamstrings operate at increased muscle-tendon lengths and velocities after surgical lengthening? *Journal of Biomechanics*, *39*(8), 1498–506.
- Arnold, A. S., Salinas, S., Asakawa, D. J., & Delp, S. L. (2000). Accuracy of muscle moment arms estimated from MRI-based musculoskeletal models of the lower extremity. *Computer Aided Surgery*, *5*, 108–119.

BIBLIOGRAPHY

- Arun, K. S., Huang, T. S., & Blostein, A. D. (1987). Least-squares fitting of two 3-D point sets. *IEEE Trans Pattern Analysis and Machine Intelligence*, 9(5).
- Asakawa, D. S., Blemker, S. S., Gold, G. E., & Delp, S. L. (2002). In vivo motion of rectus femoris muscle after tendon transfer surgery. *Journal of Biomechanics*, 35, 1029–1037.
- Asakawa, D. S., Nayak, K. S., Blemker, S. S., Delp, S. L., Pauly, J. M., Nishimura, D. G., & Gold, G. E. (2003). Real-time imaging of skeletal muscle velocity. *Journal of Magnetic Resonance Imaging*, 18, 734–739.
- Aubel, A., & Thalmann, D. (2001). Interactive modeling of the human musculature. In *Conference Proceedings Computer Animation, Seoul, Korea*.
- Bandholm, T., Sonne-Holm, S., Thomsen, C., Bencke, J., Pedersen, S., & Jensen, B. (2007). Calf muscle volume estimates: Implications for botulinum toxin treatment? *Pediatric Neurology*, 37:4, 263–269.
- Bell, A. L., Brand, R. A., & Pedersen, D. R. (1989). Prediction of hip joint centre location from external landmarks. *Human Movement Science*, 8, 3–16.
- Benoit, D. L., Ramsey, D., Lamontagen, M., Xu, L., Wretenberg, P., & Renstroem, P. (2006). Effect of skin movement artifact on knee kinematics during gait and cutting motions measured in vivo. *Gait and Posture*, 24:2, 152–164.
- Berger, A. (2002). How does it work?: Magnetic resonance imaging. *BMJ*, 324, 35.
- Besier, T. F., Sturnieks, D. L., Alderson, J. A., & Lloyd, D. G. (2003). Repeatability of gait data using a functional hip joint centre and knee helical axis. *Journal of Biomechanics*, 36(8), 1159–1168.
- Blemker, S. A., Asakawa, D. S., Gold, G. E., & Delp, S. L. (2007). Image-based musculoskeletal modeling: Applications, advances and future opportunities. *Journal of Magnetic Resonance Imaging*, 25, 441–451.
- Blemker, S. S., & Delp, S. L. (2005). Three-dimensional representation of complex muscle architectures and geometries. *Annals of Biomedical Engineering*, 33(5), 661–673.
- Blemker, S. S., & Delp, S. L. (2006). Rectus femoris and vastus intermedius fiber excursions predicted by three-dimensional muscle models. *Journal of Biomechanics*, 39:8, 1383–1391.

- Blemker, S. S., Pinsky, P. M., & Delp, S. L. (2005). A 3D model of muscle reveals the causes of nonuniform strains in the biceps brachii. *Journal of Biomechanics*, *38*, 657–665.
- Blyth, P., Stott, N. S., & Anderson, I. A. (2007). A simulation-based training system for hip fracture fixation for use within the hospital environment. *Injury, International Journal of the Care of the Injured*, *38*, 1197–1203.
- Bohannon, R. W., & Smith, M. B. (1987). Interrater reliability of a modified ashworth scale of muscle spasticity. *Physical Therapy*, *67*(2), 206–207.
- Bonet, J., & Wood, R. D. (1997). *Nonlinear Continuum Mechanics for Finite Element Analysis*. Cambridge University Press.
- Bradley, C. P., Pullan, A. J., & Hunter, P. J. (1997). Geometric modeling of the human torso using cubic hermite elements. *Annals of Biomedical Engineering*, *25*, 96–111.
- Cappozzo, A., Catani, F., Della Croce, U., & Leardini, A. (1995). Position and orientation in space of bones during movement: anatomical frame definition and determination. *Clinical Biomechanics*, *10*(4), 171–178.
- Cappozzo, A., Catani, F., Leardini, A., Benedetti, M. G., & Della Croce, U. (1996). Position and orientation in space of bones during movement: experimental artefacts. *Clinical Biomechanics*, *11*:2, 90–100.
- Cappozzo, A., Croce, U. D., Leardini, A., & Chiari, L. (2005). Human movement analysis using stereophotogrammetry Part 1: Theoretical background. *Gait and Posture*, *21*, 186–196.
- Carman, A. B., & Milburn, P. D. (2006). Determining rigid body transformation parameters from ill-conditioned spatial marker co-ordinates. *Journal of Biomechanics*, *39*, 1778 – 1786.
- Cereatti, A., Della Croce, U., & Cappozzo, A. (2006). Reconstruction of skeletal movement using skin markers: comparative assessment of bone pose estimators. *Journal of NeuroEngineering and Rehabilitation*, *3*(7), 1–12.
- Challis, J. H. (1995). A Procedure for determining rigid body transformation parameters. *Journal of Biomechanics*, *28*(6), 733–737.
- Chao, E. Y., Armiger, R. S., Yoshida, H., Lim, J., & Harguchi, N. (2007). Virtual interactive musculoskeletal system (VIMS) in orthopaedic research, education

BIBLIOGRAPHY

- and clinical patient care. *Journal of Orthopaedic Surgery and Research*, *2*(2), 1–19.
- Cheze, L. (2000). Comparison of different calculations of three-dimensional joint kinematics from video-based system data. *Journal of Biomechanics*, *33*, 1695–1699.
- Chiari, L., Della Croce, U., Leardini, A., & Cappozzo, A. (2005). Human movement analysis using stereophotogrammetry Part 2: Instrumental errors. *Gait & Posture*, *21*, 197–211.
- Chu, L. F., & Chan, B. K. (1998). Evolution of web site design: implications for medical education on the internet. *Computers in Biology and Medicine*, *28*, 459–472.
- Damsgaard, M., Rasmussen, J., Christensen, S. T., Surma, E., & de Zee, M. (2006). Analysis of musculoskeletal systems in the AnyBody modeling system. *Simulation Modelling Practice and Theory*, *14*, 1100–1111.
- Della Croce, U., Leardini, A., Chiari, L., & Cappozzo, A. (2005). Human movement analysis using stereophotogrammetry. part 4: assessment of anatomical landmark misplacement and its effects on joint kinematics. *Gait and Posture*, *21*(2), 226–237.
- Delp, S. L., Arnold, A. S., Speers, R. A., & Moore, C. A. (1996). Hamstrings and psoas lengths during normal and crouch gait: Implications for muscle-tendon surgery. *Journal of Orthopaedic Research*, *14*, 144–151.
- Delp, S. L., & Loan, J. P. (1995). A graphics-based software system to develop and analyze models of musculoskeletal structures. *Computers in Biology and Medicine*, *25*(1), 21–34.
- Delp, S. L., & Loan, J. P. (2000). A computational framework for simulating and analyzing human and animal movement. *Computing in Science and Engineering*, *2*(5), 46–55.
- Dobson, F., Morris, M. E., & Baker, R. (2007). Gait classification in children with cerebral palsy: A systematic review. *Gait and Posture*, *25*(1), 140–52.
- Dong, F., Clapworthy, G. J., Krokos, M. A., & Yao, J. (2002). An anatomy-based approach to human muscle modeling and deformation. *IEEE Transactions on Visualization and Computer Graphics*, *8*, 154–170.

- Ehrig, R. M., Taylor, W. R., Duda, G. N., & Heller, M. O. (2006). A survey of formal methods for determining the centre of rotation of ball joints. *Journal of Biomechanics*, *39*(15), 2798–809.
- Elder, G. C. B., Kirk, J., Stewart, G., Cook, K., Weir, D., Marshall, A., & Leahey, L. (2003). Contributing factors to muscle weakness in children with cerebral palsy. *Developmental Medicine and Child Neurology*, *45*, 542–550.
- Fernandez, J. W. (2004). *An Anatomically Based Finite Element Model of Patella Articulation: Towards a Diagnostic Tool*. Ph.D. thesis, University of Auckland.
- Fernandez, J. W., Akbarshahi, M., Kim, H. J., & Pandy, M. G. (2007). Integrating modelling, motion capture and x-ray fluoroscopy to investigate patellofemoral function during dynamic activity. *Computer Methods in Biomechanics*, *11:1*, 41–53.
- Fernandez, J. W., Ho, A., Walt, S., Anderson, I. A., & Hunter, P. J. (2005). A cerebral palsy assessment tool using anatomically based geometries and free-form deformation. *Biomechanics and Modeling in Mechanobiology*, *4*, 39–56.
- Fernandez, J. W., Mithraratne, P., Thrupp, S. F., Tawhai, M. H., & Hunter, P. J. (2004). Anatomically based geometric modelling of the musculo-skeletal system and other organs. *Biomechanics and Modeling in Mechanobiology*, *2*, 139–155.
- Foran, J., Steinmann, S., Barash, I., Chamers, H., & Lieber, R. (2005). Structural and mechanical alterations in spastic skeletal muscle. *Developmental Medicine and Child Neurology*, *47*, 713–717.
- Friden, J., & Lieber, R. L. (2003). Spastic muscle cells are shorter and stiffer than normal cells. *Muscle and Nerve*, *26*, 157–164.
- Fry, N. R., Gough, M., McNee, A. E., & Shortland, A. P. (2007). Changes in the volume and length of the medial gastrocnemius after surgical recession in children with spastic diplegic cerebral palsy. *Journal of Pediatric Orthopaedics*, *27(7)*, 269–774.
- Fukunaga, T., Miyatani, M., Tachi, M., Kouzaki, M., Kawakami, Y., & Kanehisa, H. (2001). Muscle volume is a major determinant of joint torque in humans. *Acta Physiologica Scandinavica*, *172*, 249–255.
- Fukunaga, T., Roy, R. R., Shellock, F. G., Hodgson, J. A., Day, M. K., Lee,

BIBLIOGRAPHY

- P. L., Kwong-Fu, H., & Edgerton, V. R. (1992). Physiological cross-sectional area of human leg muscles based on magnetic resonance imaging. *Journal of Orthopaedic Research*, *10*(6), 926–934.
- Fuller, J., Liu, L.-J., Murphy, M., & Mann, R. (1997). A comparison of lower-extremity skeletal kinematics measured using skin- and pin-mounted markers. *Human Movement Science*, *16*, 219–242.
- Gage, J. R. (2004). *The Treatment of Gait Problems in Cerebral Palsy*. Mac Keith Press.
- Gold, G. E., Besier, T. F., Draper, C. E., Asakawa, D. S., Delp, S. L., & Bequpre, G. S. (2004). Weight-bearing MRI of patellofemoral joint cartilage contact area. *Journal of Magnetic Resonance Imaging*, *20*(3), 526–530.
- Graham, H. K., & Selber, P. (2003). Musculoskeletal Aspects of Cerebral Palsy - Review Article. *Journal of Bone and Joint Surgery*, *85*, 157–66.
- Grood, E. S., & Suntay, W. J. (1983). A joint coordinate system for the clinical description of three-dimensional motions: Application to the knee. *Journal of Biomechanical Engineering*, *105*, 136–144.
- Harrington, M. E., Zavatsky, A. B., Lawson, S. E. M., Yuan, Z., & Theologis, T. N. (2007). Prediction of the hip joint centre in adults, children, and patients with cerebral palsy based on magnetic resonance imaging. *Journal of Biomechanics*, *40*(3), 595–602.
- John, N. W., & Lim, L. S. (2007). Cybermedicine tools for communication and learning. *Journal of Visual Communication in Medicine*, *30*(1), 4–9.
- Jonkers, I., Stewart, C., Desloovere, K., Molenaers, G., & Spaepen, A. (2006). Musculo-tendon length and lengthening velocity of rectus femoris in stiff knee gait. *Gait and Posture*, *23*, 222–229.
- Kadaba, M. P., Rmakrishnan, H. K., & Wootten, M. E. (1989). Measurement of lower extremity kinematic during level walking. *Journal of Orthopaedic Research*, *8*, 383–392.
- Klein Horsman, M., Koopman, H., van der Helm, F., Poliacu Prose, L., & Veeger, H. (2007). Morphological muscle and joint parameters for musculoskeletal modelling of the lower extremity. *Clinical Biomechanics*, *22*, 239–247.
- Lampe, R., Grassl, S., Mitternacht, J., Gerdesmeyer, L., & Gradinger, R. (2006).

- MRT-measurements of muscle volumes of the lower extremities of youths with spastic hemiplegia caused by cerebral palsy. *Brain and Development*, *28*, 500–506.
- Leardini, A., Chiari, L., Della Croce, U., & Cappozzo, A. (2005). Human movement analysis using stereophotogrammetry Part 3: Soft tissue artifact assessment and compensation. *Gait and Posture*, *21*, 212–225.
- Lemos, R., Rokne, J., Baranoski, G. V. G., Kawakami, Y., & Kurihara, T. (2005). Modeling and simulating the deformation of human skeletal muscle based on anatomy and physiology. *Computer Animation and Virtual Worlds*, *16*, 319–330.
- Lieber, R., Steinman, S., Barash, I., & Chambers, H. (2004). Structural and functional changes in spastic skeletal muscle. *Muscle and Nerve*, *29*, 615–627.
- Lieber, R. L., & Friden, J. (2000). Functional and clinical significance of skeletal muscle architecture. *Muscle and Nerve*, *23*, 1647–1666.
- Lu, T.-W., & O'Connor, J. J. (1999). Bone position estimation from skin marker co-ordinates using global optimisation with joint constraints. *Journal of Biomechanics*, *32*, 129–134.
- Magenat-Thalmann, N., & Thalmann, D. (2005). Virtual humans: thirty years of research, what next? *The Visual Computer*, *21*, 997–1015.
- Malaiya, R., McNee, A. E., Fry, N. R., Eve, L. C., Gough, M., & Shortland, A. P. (2007). The morphology of the medial gastrocnemius in typically developing children and children with spastic hemiplegic cerebral palsy. *Electromyography and Kinesiology*, *17*, 657–663.
- Medved, V. (2001). *Measurement of Human Locomotion*. CRC Press.
- Meier, P., & Blickhan, R. (2000). *Skeletal Muscle Mechanics: From Mechanisms to Function*. John Wiley and Sons, Ltd.
- Mithraratne, K., & Hunter, P. J. (2006). Customisation of anatomically based musculoskeletal structures. In *Proceedings of the 15th International Conference on Mechanics in Medicine and Biology*.
- Mohagheghi, A. A., Khan, T., Meadows, T. H., Giannicas, K., Baltzopoulos, V., & Maganaris, C. N. (2007). Differences in gastrocnemius muscle architecture

BIBLIOGRAPHY

- between the paretic and non-paretic legs in children with hemiplegic cerebral palsy. *Clinical Biomechanics*, *22*, 718–724.
- Mohagheghi, A. A., Khan, T., Meadows, T. H., Giannikas, K., Baltzopoulos, V., & Maganaris, C. N. (2008). In vivo gastrocnemius muscle fascicle length in children with and without diplegic cerebral palsy. *Developmental Medicine and Child Neurology*, *50*, 44–50.
- Molenaers, G., Desloovere, K., Fabry, G., & De Cock, P. (2006). The effects of quantitative gait assessment and botulinum toxin a on musculoskeletal surgery in children with cerebral palsy. *Journal of Bone and Joint Surgery*, *88*, 161–170.
- Moro-oka, T., Hamai, S., Miura, H., Shimoto, T., Higaki, H., Fregly, B. J., Iwamoto, Y., & Banks, S. A. (2007). Can magnetic resonance imaging-derived bone models be used for accurate motion measurement with single-plane three-dimensional shape registration? *Orthopaedic Research*, *25*(7), 867–872.
- Nash, M. P., & Hunter, P. J. (2000). Computational mechanics of the heart. *Journal of Elasticity*, *61*, 113–141.
- Nigg, B. M., & Herzog, W. (Eds.) (1999). *Biomechanics of the Musculo-skeletal System*, 2nd edition. John Wiley and Sons, Ltd.
- Nipp, K., & Stoffer, D. (2002). *Lineare Algebra*, vol. 5. vdf Hochschulverlag AG ETH Zuerich.
- Oberhofer, K., Mithraratne, K., & Stott, I. A., N. S. and Anderson (2009a). Anatomically-based musculoskeletal modeling: prediction and validation of muscle deformation during walking. *The Visual Computer*, *25*(9), 843–851.
- Oberhofer, K., Mithraratne, K., Stott, N. S., & Anderson, I. A. (2009b). Error propagation from kinematic data to modeled muscle-tendon lengths during walking. *Journal of Biomechanics*, *42*, 77–81.
- Oberhofer, K., Stott, N. S., Mithraratne, K., & Anderson, I. A. (2009c). Subject-specific modelling of lower limb muscles in children with cerebral palsy. *Clinical Biomechanics*, *accepted*.
- Paul, J. P. (1998). History and fundamentals of gait analysis. *Bio-Medical Material and Engineering*, *8*, 123–135.

- Ramakrishnan, H. K., & Kadaba, M. P. (1991). On the estimation of joint kinematics during gait. *Journal of Biomechanics*, *24*(10), 969–977.
- Reinschmidt, C., van den Boger, A., Nigg, B., Lundberg, A., & Murphy, N. (1997). Effect of skin movement on the analysis of skeletal knee joint motion during running. *Journal of Biomechanics*, *30*:7, 729–732.
- Robertson, D. G. E., Caldwell, G. E., Hamill, J., Kamen, G., & Whittlesey, S. (2004). *Research Methods in Biomechanics*. Human Kinetics.
- Rodda, J., & Graham, H. K. (2001). Classification of gait patterns in spastic hemiplegia and spastic diplegia: a basis for a management algorithm. *European Journal of Neurology*, *8*(Suppl 5), 98–108.
- Roehrl, O., & Pullan, A. (2007). Three-dimensional finite element modelling of muscle forces during mastication. *Journal of Biomechanics*, *40*(3363-3372), 3363–3372.
- Rosenbaum, P. L., Plisano, R. J., Bartlett, D. J., Galuppi, B. E., & Russell, D. J. (2008). Development of the gross motor function classification system for cerebral palsy. *Developmental Medicine and Child Neurology*, *50*, 249–253.
- Satava, R. M. (1995). Medical applications of virtual reality. *Journal of Medical Systems*, *19*(3), 275–280.
- Schache, A. G., Baker, R., & Lamoreux, L. W. (2006). Defining the knee joint flexion-extension axis for purposes of quantitative gait analysis: An evaluation of methods. *Gait and Posture*, *24*(1), 100–109.
- Scheepers, F., Parent, R. E., Carlson, W. E., & May, S. F. (1997). Anatomy-based modeling of the human musculature. In *SIGGRAPH '97: Proceedings of the 24th annual conference on Computer graphics and interactive techniques*.
- Scholtes, V. A. B., Becher, J. G., Beelen, A., & Lankhorst, G. J. (2006). Clinical assessment of spasticity in children with cerebral palsy: a critical review of available instruments. *Developmental Medicine and Child Neurology*, *48*, 64–73.
- Schutte, L. M., Hayden, S. W., & Gage, J. R. (1997). Lengths of hamstrings and psoas muscles during crouch gait: Effects of femoral anteversion. *Journal of Orthopaedic Research*, *15*, 615–621.

BIBLIOGRAPHY

- Sederberg, T. W., & Parry, S. R. (1986). Free-form deformation of solid geometric models. *ACM Computer Graphics*, 20:4, 151–160.
- Shim, V. B., Pitto, R. P., Streicher, R. M., Hunter, P. J., & Anderson, I. A. (2007). The use of sparse CT datasets for auto-generating accurate FE models of the femur and pelvis. *Journal of Biomechanics*, 40, 26–35.
- Shortland, A. P., Harris, C. A., Gough, M., & O Robinson, R. (2002). Architecture of the medial gastrocnemius in children with spastic diplegia. *Developmental Medicine and Child Neurology*, 44, 158–163.
- Silen, C., Wirell, S., Kvist, J., Nylander, E., & Smedby, O. (2008). Advanced 3D visualization in student-centred medical education. *Medical Teacher*, 30(5), 115–124.
- Simon, S. R. (2004). Quantification of human motion: gait analysis - benefits and limitations to its application to clinical problems. *Journal of Biomechanics*, 37, 1869–1880.
- Sinav, A., & Ambron, R. (2004). Interactive web-based programs to teach functional anatomy: The pterygopalatine fossa. *The Anatomical Record (Part B: New Anatomy)*, 279B, 4–8.
- Soederkvist, I., & Wedin, P.-A. (1993). Determining the Movements of the Skeleton using Well-configured Markers. *Journal of Biomechanics*, 26(12), 1473–1477.
- Spitzer, V., & Whitlock, D. (1998a). The Visible Human Dataset: The anatomical platform for human simulation. *The Anatomical Record B (New Anatomist)*, 253(2), 49–57.
- Spitzer, V. M., & Whitlock, D. (1998b). *Atlas of the Visible Human Male*. Jones and Bartlett Publishers, Inc.
- Spoor, C. W., & Veldpaus, F. E. (1980). Rigid body motion calculated from spatial co-ordinates of markers. *Journal of Biomechanics*, 13, 391–393.
- Stagni, R., Fantozzi, A., Cappello, A., & Leardini, A. (2005). Quantification of soft tissue artefact in motion analysis by combining 3D fluoroscopy and stereophotogrammetry: a study on two subjects. *Clinical Biomechanics*, 20, 320–329.
- Stagni, R., Fantozzi, S., & Cappello, A. (2006). Propagation of anatomical

- landmark displacement to knee kinematics: Performance of single and double calibration. *Gait and Posture*, *24*, 137–141.
- Stagni, R., Leardini, A., Cappozzo, A., Benedetti, M. G., & Cappello, A. (2000). Effects of hip joint centre mislocation on gait analysis results. *Journal of Biomechanics*, *33*, 1479–1487.
- Storey, M.-A., Phillips, B., Maczewski, M., & Wang, M. (2001). Evaluating the usability of web-based learning tools. In *World Conferences on Educational Multimedia, Hypermedia and Telecommunications, Tampere, Finland*.
- Sutherland, D. H. (2001). The evolution of clinical gait analysis Part I: kinesiological emg. *Gait and Posture*, *14*, 61–70.
- Sutherland, D. H. (2002). The evolution of clinical gait analysis Part II kinematics. *Gait and Posture*, *16*, 159–179.
- Sutherland, D. H. (2005). The evolution of clinical gait analysis Part III - kinetics and energy assessment. *Gait and Posture*, *21*, 447–461.
- Taylor, J. R. (1982). *An introduction to error analysis*. University Science Books.
- Teran, J., Sifakis, E., Blemker, S. S., Ng-Thow-Hing, V., Lau, C., & Fedkiw, R. (2005). Creating and simulating skeletal muscle from the visible human data set. *IEEE Transactions on Visualization and Computer Graphics*, *11:3*, 317–328.
- Vasavada, A. N., Lasher, R. A., Meyer, T. E., & Lin, D. C. (2008). Defining and evaluating wrapping surfaces for MRI-derived spinal muscle paths. *Journal of Biomechanics*, *41(7)*, 1450–1457.
- Whittle, M. (2002). *Gait Analysis: An Introduction*. Elsevier Health Sciences.
- Wickiewicz, T., Roy, R. R., Powell, P. L., & Edgerton, V. R. (1983). Muscle architecture of the human lower limb. *Clinical Orthopaedics and Related Research*, *179*, 275–283.
- Winter, D. A. (1990). *Biomechanics and Motor Control of Human Movement, Second Edition*. John Wiley and Sons, Ltd.
- Woltring, H., Huiskes, R., & De Lange, A. (1985). Finite centroid and helical axis estimation from noisy landmark measurements in the study of human joint kinematics. *Journal of Biomechanics*, *18(5)*, 379–389.

BIBLIOGRAPHY

- Woltring, H. J. (1994). 3-D attitude representation of human joints: a standardization proposal. *Journal of Biomechanics*, *27*(12), 1399–1414.
- Wren, T. A. L., Do, K. P., & Kay, R. M. (2004). Gastrocnemius and soleus lengths in cerebral palsy equinus gait - differences between children with and without static contracture and effects of gastrocnemius recession. *Journal of Biomechanics*, *37*, 1321–1327.
- Wu, G. (2002). ISB recommendation on definitions of joint coordinate system of various joints for the reporting of human joint motion - part i: ankle, hip and spine. *Journal of Biomechanics*, *35*, 543–548.
- Young, S. (1987). *Magnetic Resonance imaging: Basic principles*. Raven Press, New York.
- Zajac, F. E. (1993). Muscle coordination of movement: a perspective. *Journal of Biomechanics*, *26*, 109–124.
- Zajac, F. E., Neptune, R. R., & Kautz, S. A. (2002). Biomechanics and muscle coordination of human walking Part I: Introduction to concepts, power transfer, dynamics and simulations. *Gait and Posture*, *16*, 215–232.
- Zienkiewicz, O., & Taylor, R. (2000). *Finite Element Method Volume 1 - The Basis*. Elsevier.